論文 / 著書情報
Article / Book Information

題目(和文)	陽子のK+ υ 崩壊事象の探索
Title(English)	Search for proton decay into K+ υ
著者(和文)	早戸良成
Author(English)	Yoshinari Hayato
出典(和文)	学位:博士(理学), 学位授与機関:東京工業大学, 報告番号:甲第3656号, 授与年月日:1998年3月26日, 学位の種別:課程博士, 審査員:
Citation(English)	Degree:Doctor (Science), Conferring organization: Tokyo Institute of Technology, Report number:甲第3656号, Conferred date:1998/3/26, Degree Type:Course doctor, Examiner:
学位種別(和文)	博士論文
Type(English)	Doctoral Thesis

Search for proton decay into $K^+\bar{\nu}$

Yoshinari Hayato

High Energy Experimental Physics Group

Department of Physics

Tokyo Institute of Technology

Ph.D Dissertation

February 1998

Acknowledgments

First of all, I would like to express my great gratitude to Professor Y.Watanabe for continuous guidance and encouragement. I wish to express my gratitude to Professor T.Tanimori for his suggestive advice. I also thank Dr.K.Kaneyuki for his useful suggestions and for his hard work.

This work presented in this thesis was done as a part of the Super-Kamiokande experiment. It is a great experience for me to participate in this experiment. I thank all the collaborators of the Super-Kamiokande experiment. In particular, I would like to thank Professor Y.Totsuka for providing me the opportunity to participate in this exciting experiment. I wish to thank Professor M.Koshiba for promoting this experiment.

I would like to express my appreciation to Professor T.Kajita for his helpful suggestions and for deep insight in physics. I am grateful to Dr.Y.Itow, Dr.M.Miura and Mr.M.Shiozawa for a lot of helpful discussions, fruitful suggestions in proton decay analysis. I also thank Professor K.Young, Professor R.J.Wilkes, Dr.T.Hasegawa, Dr.L.Wai, Messrs T.Hayakawa, K.Fujita, S.Kasuga, J.George, M.Etoh, K.Ishihara, Y.Kanaya, K.Okumura and J.Kameda for their cooperation in analysis of atmospheric neutrino and proton decay.

I with to thank Professor Y.Suzuki and Professor M.Nakahata for many useful discussions and suggestions. I thank Dr.K.Inoue for his kind help in handling data. I thank Dr.Y.Fukuda, Dr.J.Kanzaki, Dr.K.Martens, Dr.Y.Takeuchi, Dr.M.Takita, Messrs Y.Koshio, H.Okazawa, T.Yamaguchi, H.Ishino for their useful discussions.

I also thank Professors K.Miyano, M.Mori, Y.Nagashima, K.Nakamura, K.Nishikawa, M.Sakuda, A.Suzuki, Dr.T.Ishii, Dr.T.Kobayashi, Dr.K.Nishijima, Dr.Y.Oyama, Dr.O.Sasaki, Dr.Atsumu Suzuki for their kind suggestions.

I gratefully acknowledge the cooperation of the Kamioka Mining and Smelting Company.

Finally, I would like to thank all the members of high energy physics group at Tokyo Institute of Technology for their kind help.

Super-Kamiokande Collarboration

Y.Fukuda[a], T.Hayakawa[a], E.Ichihara[a], K.Inoue[a], K.Ishihara[a], H.Ishino[a], Y.Itow[a], T.Kajita[a], J.Kameda[a], S.Kasuga[a], K.Kobayashi[a], Y.Kobayashi[a], Y.Koshio[a], K.Martens[a], M.Miura[a], M.Nakahata[a], S.Nakayama[a], A.Okada[a], M.Oketa[a], K.Okumura[a], M.Ota[a], N.Sakurai[a], M.Shiozawa[a], Y.Suzuki[a], Y.Takeuchi[a], Y.Totsuka[a], S.Yamada[a], M.Earl[b], A.Habig[b], J.T.Hong[b], E.Kearns[b], S.B.Kim[b], M.Masuzawa[b,1], M.Messier[b], K.Scholberg[b], J.L.Stone[b], L.R.Sulak[b], C.W.Walter[b], M.Goldhaber[c], T.Barszczak[d], W.Gajewski[d], P.G.Halverson[d,2], J.Hsu[d], W.R.Kropp[d], L.R. Price[d], F.Reines[d], H.W.Sobel[d], M.R.Vagins[d], K.S.Ganezer[e], W.E.Keig[e], E.W.Ellsworth[f], S.Tasaka[g], J.Flanagan[h], A.Kibayashi[h], J.G.Learned[h], S.Matsuno[h], V.Stenger[h], D.Takemori[h], T.Ishii[i], J.Kanzaki[i], T.Kobayashi[i], K.Nakamura[i], K.Nishikawa[i], Y.Oyama[i], A.Sakai[i], M.Sakuda[i], O.Sasaki[i], S.Echigo[j], M.Kohama[j], A.T.Suzuki[j], T.J.Haines[k,d] E.Blaufuss[l], R.Sanford[l], R.Svoboda[l], M.L.Chen[m], Z.Conner[m,3] J.A.Goodman[m], G.W.Sullivan[m], M.Mori[n,4], F.Goebel[o,5], J.Hill[o], C.K.Jung[o], C.Mauger[o], C.McGrew[o], E.Sharkey[o], B.Viren[o], C.Yanagisawa[o], W.Doki[p], T.Ishizuka[p,6], Y.Kitaguchi[p], H.Koga[p], K.Miyano[p], H.Okazawa[p], C.Saji[p], M.Takahata[p], A.Kusano[q], Y.Nagashima[q], M.Takita[q], T.Yamaguchi[q], M.Yoshida[q], M.Etoh[r], K.Fujita[r], A.Hasegawa[r], T.Hasegawa[r], S.Hatakeyama[r], T.Iwamoto[r], T.Kinebuchi[r], M.Koga[r], T.Maruyama[r], H.Ogawa[r], M.Saito[r], A.Suzuki[r], F.Tsushima[r], M.Koshiba[s], M.Nemoto[t], K.Nishijima[t], T.Futagami[u], Y.Hayato[u], Y.Kanaya[u], K.Kaneyuki[u], Y.Watanabe[u], D.Kielczewska[v,d,7], R.Doyle[w], J.George[w], A.Stachyra[w], L.Wai[w], J.Wilkes[w], K.Young[w]

[a]*Institute for Cosmic Ray Research, University of Tokyo, Tanashi, Tokyo 188-8502, Japan*

[b]*Boston University, Boston, MA 02215, USA*

[c]*Physics Department, Brookhaven National Laboratory, Upton, NY 11973, USA*

[d]*Department of Physics and Astronomy, University of California, Irvine Irvine, CA 92697-4575, USA*

---

[1]Present address: High Energy Accelerator Research Organization (KEK)

[2]Present address: NASA, JPL, Pasadena, CA 91109, USA

[3]Present address: Enrico Fermi Institute, University of Chicago, Chicago, IL 60637 USA

[4]Present address: Institute for Cosmic Ray Research, University of Tokyo

[5]Present address: Deutsches Elektronen-Synchrotron DESY, Hamburg, Germany

[6]Present address: Department of System Engineering, Shizuoka University Hamakita, Shizuoka 432, Japan

[7]Supported by the Polish Committee for Scientific Research.

[e] *Department of Physics, California State University, Dominguez Hills, Carson, CA 90747, USA*
[f] *George Mason University, Fairfax, VA 22030, USA*
[g] *Department of Physics, Gifu University, Gifu, Gifu 501-1112, Japan*
[h] *The University of Hawaii, Honolulu, Hawaii 96822, USA*
[i] *Institute of Particle and Nuclear Studies, High Energy Accelerator Research Organization (KEK), Tsukuba, Ibaraki 305-0801, Japan*
[j] *Department of Physics, Kobe University, Kobe, Hyogo 657-0013, Japan*
[k] *Physics Division, P-23, Los Alamos National Laboratory, Los Alamos, NM 87544, USA.*
[l] *Louisiana State University, Baton Rouge, Louisiana 70803, USA*
[m] *University of Maryland, College Park, MD 20742, USA*
[n] *Department of Physics, Miyagi University of Education, Sendai, Miyagi 980, Japan*
[o] *State University of New York, Stony Brook, NY 11794-3800, USA*
[p] *Department of Physics, Niigata University, Niigata, Niigata 950-2102, Japan*
[q] *Department of Physics, Osaka University, Toyonaka, Osaka 560-0043, Japan*
[r] *Department of Physics, Tohoku University, Sendai, Miyagi 980-8578, Japan*
[s] *The University of Tokyo, Tokyo 113-0033, Japan*
[t] *Department of Physics, Tokai University, Hiratsuka, Kanagawa 259-1292, Japan*
[u] *Department of Physics, Tokyo Institute for Technology, Meguro, Tokyo 152-0033, Japan*
[v] *Institute of Experimental Physics, Warsaw University, 00-681 Warsaw, Poland*
[w] *Department of Physics, University of Washington, Seattle, WA 98195-1560, USA*

Abstract

A search for proton decay into $K^+\bar{\nu}$, which is predicted by SUSY-SU(5) GUT, is performed with the Super-Kamiokande detector. The total exposure of the detector is 25.5 kt·yr. We obtained a total of 3468 fully contained events. We have analyzed the proton decay mode of $p \to \bar{\nu}K^+$ by using the decay products of K^+. The major decay modes of K^+ are $K^+ \to \mu^+\nu_\mu$ and $K^+ \to \pi^+\pi^0$, and both modes have been analyzed. Also the prompt 6.3MeV γ-ray tagging method has been used for $K^+ \to \mu^+\nu_\mu$ mode analysis to eliminate almost all the background events caused by atmospheric neutrino. Although the number of candidate events are consistent with the expected number of atmospheric neutrino events and no statistical significant evidence of proton decay for this mode has been observed. Thus, the 90% confidence level lower limits of partial lifetime are obtained as :

$$\tau/B(p \to \bar{\nu}K^+) \geq 2.8 \times 10^{32} \text{ yr for } K^+ \to \nu_\mu\mu^+,$$
$$\tau/B(p \to \bar{\nu}K^+) \geq 1.3 \times 10^{32} \text{ yr for } K^+ \to \pi^0\pi^+,$$
$$\tau/B(p \to \bar{\nu}K^+) \geq 1.5 \times 10^{32} \text{ yr for } K^+ \to \nu_\mu\mu^+ \text{ with prompt } \gamma\text{ray-tag.}$$

Combining the first two, which are independent to each other, the limit obtained is

$$\tau/B(p \to \bar{\nu}K^+) \geq 3.3 \times 10^{32}\text{yr. (90\% C.L.).}$$

Contents

Chapter 1

Introduction

The ultimate motivation of the particle physics is to understand fundamental particles and interactions among them. In the last decades, dramatic progress has been made and the "standard model" in particle physics has been established. It consists of SU(2)×U(1) electro-weak gauge theory which has been proposed by Glashow, Weinberg and Salam in 1960's[1] and of SU(3) color gauge theory of strong interaction[2]. This is one of the most successful models and there are essentially no experimental results which are inconsistent with the predictions. The results of experiments from Fermilab's Tevatron proton-antiproton collider and CERN's LEP electron-positron collider, for example, agree very well with the predictions of the standard model and strongly support this model. In 1995, the top-quark has been found at Tevatron[3] and now only the Higgs boson remains to be discovered.

In spite of its great success, the standard model cannot be the ultimate theory. First of all the gravitation interaction is not included. Also the model contains so many free parameters which have to be determined by measurements, such as masses of quarks and leptons, mixing angles of quarks, number of generations for quarks and leptons. Further, the source of charge quantization or the relations between three coupling constants cannot be predicted in the framework of the standard model. Thus, after the successful unification of electromagnetic and weak interactions, attempts to develop a unified theory of the strong and electroweak interactions (GUT: Grand Unified Theory) have been started.

The minimal gauge group which contains SU(3)×SU(2)×SU(1) is SU(5). The simplest

GUT model is the minimal SU(5) GUT[4]. One of the most impressive predictions of GUT is the baryon number violation. This occurs because leptons and quarks are placed in the same multiplet in the GUT. Therefore, experiments to search for nucleon decays are very important to test GUTs, which allow us to probe physics at extremely high energy scale unattainable by accelerators. Several such experiments have been performed but there are no statistically significant evidences for nucleon decays reported up to now. The minimal SU(5) GUT predicts $p \to e^+\pi^0$ as the dominant decay mode of proton, of which partial lifetime is 3.3×10^{31} yr at maximum. But the experimental lower limits obtained up to now is much longer than this prediction. For example, the obtained lower limit of partial lifetime for $p \to e^+\pi^0$ is 5.5×10^{32} yr from IMB experiment[5]. Also the predicted parameters, such as $\sin^2\theta_W$, where θ_W is the Weinberg angle, is different from the result obtained from the precise measurements at LEP and SLC and the running coupling constants do not meet at a single point in contradiction to the prediction. Thus, the minimal SU(5) GUT has been ruled out.

To remedy theoretical unnaturalness and discrepancy, imposition of Supersymmetry (SUSY) has been proposed[6]. SUSY theory introduces a new symmetry between fermions and bosons and every particle has its own SUSY partner with the spin different by 1/2. The minimal SUSY-SU(5) GUT predicts $p \to \bar{\nu}K^+$ as a major mode of proton decay in contrast with minimal SU(5) GUT[7]. The obtained lower limit of partial lifetime for $p \to \bar{\nu}K^+$ is 1.0×10^{32} yr from KAMIOKANDE experiment[8].

The Super-Kamiokande experiment employs the world largest Water Cherenkov detector of which fiducial volume is 22,500 metric tons. By using this detector, we can survey nucleon decay modes of which partial lifetime is up to about 10 times longer than the current lifetime limits within 5 years.

In this thesis, we present the first result of proton decay analysis for $p \to \bar{\nu}K^+$ mode in Super-Kamiokande. We use the data from May 1996 to October 1997, of which total exposure time of the detector is 25.5 kt·yr. The obtained results are compared with the theoretical predictions by the minimal SUSY-SU(5) GUT.

In chapter 2, theoretical background is described. The apparatus of the Super-Kamiokande detector are explained in chapter 3. Monte Carlo simulations of proton decay and atmospheric neutrino events to study the background are summarized in chapter 4. Each reduction step of the data is described in chapter 5. The analysis tools are described in chapter 6. In chapter 7, calibration and the uncertainties in energy determination are presented. The characteristics of the event sample are shown in chapter 8. In chapter 9, the result on the proton decay analysis and discussions are presented. Finally the conclusion is given in chapter 10.

Chapter 2

Theoretical background

The basic idea of GUTs is to unify the three independent gauge groups, SU(2)×SU(1) electro-weak theory and SU(3) color gauge theory into a theory of one gauge group. In this type of model, all the three gauge coupling constants are unified above the GUT scale of $\sim 10^{14-16}$ GeV. Quarks and leptons are assigned to common multiplets and new gauge bosons mediate transition. As a result, it becomes possible to transform a quark into a lepton via gauge boson exchange. It means that the baryon and lepton number violating interactions, such as proton decay, are allowed. Also, the GUTs have capability to predict the Weinberg angle, to relate charges between lepton and quark and so on.

The simplest GUT model is the minimal SU(5) GUT model[4]. SU(5) is the minimum gauge group which contains SU(3)×SU(2)×SU(1). There are 24 gauge bosons in this model: 8 gluons of SU(3), $W^{\pm}$, Z^0 and photon for SU(2)×U(1) and 12 very massive X and Y bosons, of which masses are of the order of the unification scale. $X(\overline{X})$ has electric charge $\frac{4}{3}(-\frac{4}{3})$ while $Y(\overline{Y})$ has the charge $\frac{1}{3}(-\frac{1}{3})$. Also X and Y carry the color. Thus, the transformation from quark to lepton is possible by mediating X or Y. The three generations of leptons and quarks are treated equally. Each generation consists of 15 states: two quarks, each in 3 color states (denoted by R, G and B) and 2 helicity states (L and R); charged leptons with 2 helicity states; and neutrino with 1 helicity state. These states are assigned to $\bar{5}+10$ dimension representations as follows:

$$\bar{5} = \begin{pmatrix} \nu_e \\ e^- \\ \overline{d_R} \\ \overline{d_B} \\ \overline{d_G} \end{pmatrix}_L,$$

$$10 = \begin{pmatrix} 0 & e^+ & d_R & d_B & d_G \\ -e^+ & 0 & u_R & u_B & u_G \\ -d_R & -u_R & 0 & \overline{u_G} & \overline{u_B} \\ -d_B & -u_B & -\overline{u_G} & 0 & \overline{u_R} \\ -d_G & -u_G & -\overline{u_B} & -\overline{u_R} & 0 \end{pmatrix}_L.$$

The total electric charge ($\sum Q_i$) in these multiplets is 0. Thus, the charges between quarks and electrons are directly related.

As described before, the existence of X and Y introduces the baryon and lepton number violating processes. However the number B$-$L, where B is the baryon number and L is the lepton number, is always conserved in baryon and lepton number violating processes. Figure 2.1 shows typical diagrams of proton decay via X and Y exchanges (dimension-six operators). The dominant factor of this decay probability is propagator of X, $(q^2+M_X^2)^{-1}$, where q^2 is the momentum transfer squared and it is only about 1GeV^2. Thus the decay rate is proportional to M_X^{-4}. The theoretical prediction of partial lifetime for $p \to e^+\pi^0$ is

$$\tau(p \to e^+\pi^0) \simeq 3.7 \times 10^{29\pm0.7} \left(\frac{M_X}{2\times10^{14}\mathrm{GeV}}\right)^4 \mathrm{yr}, \tag{2.1}$$

with the QCD scale parameter $\Lambda_{\overline{\mathrm{MS}}} = 150^{+150}_{-75}$MeV. The mass of X is estimated as $M_X = 2.0^{+2.1}_{-1.0} \times 10^{14}$ GeV[4]. As a result, the predicted partial lifetime for this mode is 3.3×10^{31} yr at maximum. But the results from Kamiokande and IMB experiments have already shown that the partial lifetime is 10 times longer than this prediction[8][5]. Also, the precise measurement of $\sin^2\hat{\theta}_W(M_Z)$ in LEP and other experiments excludes the minimal SU(5) GUT. The predicted value of $\sin^2\hat{\theta}_W(M_Z)$ is $0.2102^{+0.0037}_{-0.0031}$[9] but the measured value is 0.2315 ± 0.0004[10]. The running coupling constants ($\alpha_i(Q^2)$) can be written as follows:

$$\frac{1}{\alpha_i(Q^2)} = \frac{1}{\alpha_i(\mu^2)} + \frac{1}{4\pi} b_i \ln \frac{Q^2}{\mu^2}, \tag{2.2}$$

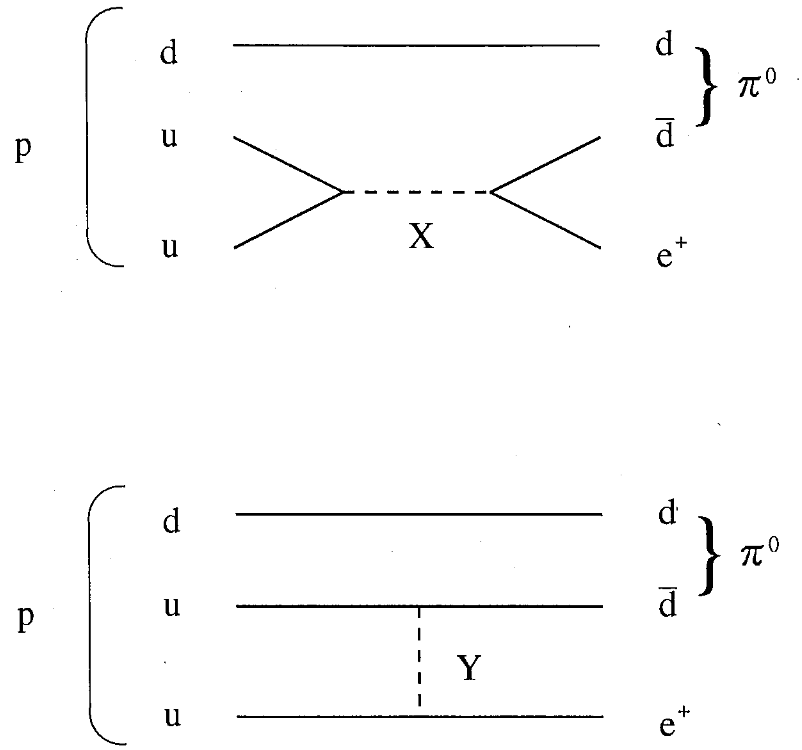

Figure 2.1: Diagram of proton decay via X and Y exchanges.

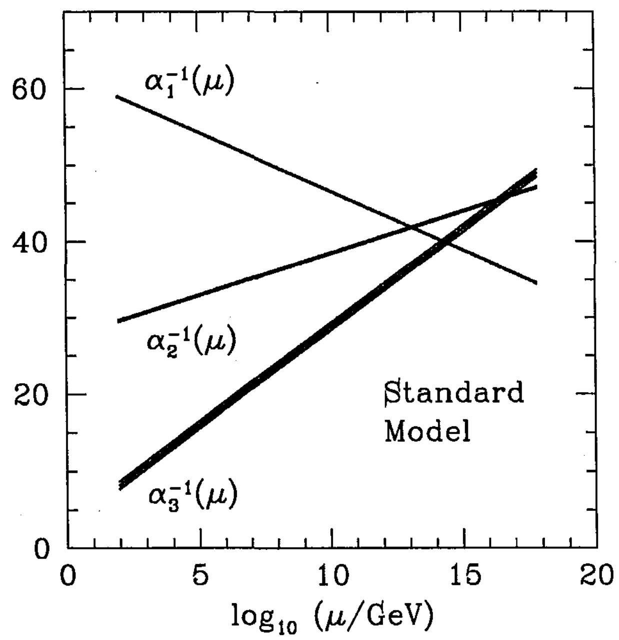

Figure 2.2: Evolution of three coupling constants in the minimal SU(5) GUT model[11].

where $b_i = (\frac{41}{10}, -\frac{19}{6}, -7)$, $\mu^2 = M_Z^2$, M_Z is the mass of Z^0 and Q^2 is the momentum transfer squared. If we use the input parameters obtained from the experiments, these three coupling constants do not meet at one point[Figure 2.2]. Therefore, the minimal SU(5) GUT has been ruled out and we have to extend or search for another model.

Among the extended models, introducing SUSY GUT (Supersymmetric GUT) has become very popular. SUSY theory introduces a new symmetry between fermions and bosons. In this model, every particle has its own SUSY partner with spin different by 1/2. At the same time, at least one more Higgs doublet is required for the mass generation as a natural extension from the standard model. In the minimal extension of the standard model, MSSM, which stands for the Minimal Supersymmetric Standard Model, "R-parity" symmetry is also required. This symmetry assigns a charge of -1 to the SUSY particles and 1 to the normal particles including Higgs bosons and the R-parity violating processes are prohibited. Thus, there must be even number of SUSY particles at every interaction vertex. This symmetry assures the suppression of the very fast nucleon decay and the absolute stability of the lightest SUSY particle. In the minimum SUSY-SU(5) GUT model, the predicted $\sin^2\theta_W$ is 0.2316 ± 0.0003[9] and this number is consistent with the experimental

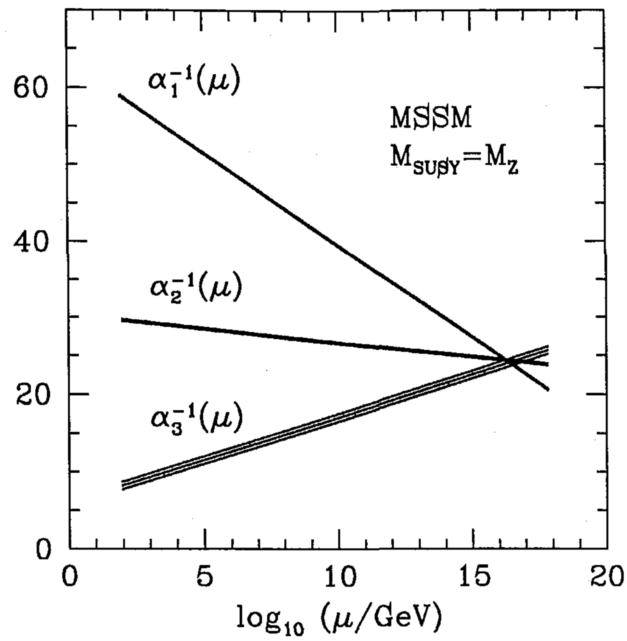

Figure 2.3: Evolution of three coupling constants in the minimal SUSY-SU(5) GUT model.[11].

data. For the running coupling constants, the b_i in the eqn.2.2 are modified as follows:

$$b_i = (\frac{33}{5}, 1, -3), \tag{2.3}$$

and the modification of b_i lead the three coupling constants to meet at $\sim 3\times10^{16}$ GeV[Figure 2.3]. In this model, X and Y gauge bosons are expected to be heavier compared to those of the minimal non-SUSY-SU(5) GUT and the predicted partial lifetime of proton decay via a single gauge boson exchange is about 10^{33} to 10^{35} yr. It is very hard to cover all the lifetime limit range even in Super-Kamiokande. But the SUSY SU(5) GUT predicts another decay mode which does not appear in the minimal SU(5) GUT. As shown in Figure 2.4, the Higgsino mediates the conversion of the quarks in the proton to quarks and sleptons (dimension-five operator).

Thus, in the final state, a strange particle is produced. The predicted partial lifetime is proportional to $M_{\tilde{H}}^2 \sin^2\beta/|f^2|$, where $f \sim m_{\chi^+}/m_{\tilde{q}}^2$, $M_{\tilde{H}}$ is the mass of Higgsino, β is the vacuum angle of doublet Higgs scalars, m_{χ^+} is the mass of chargino and $m_{\tilde{q}}$ is the mass of squark. The detailed studies of nucleon decay in the framework of the SUSY-SU(5) GUT

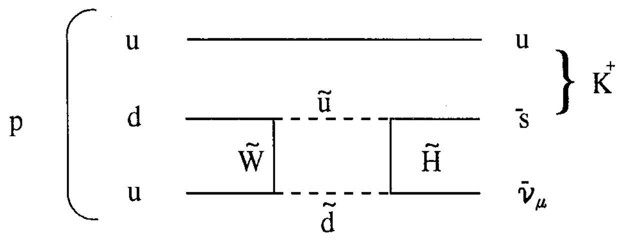

Figure 2.4: Diagram of proton decay predicted by SUSY-SU(5) GUT.

have been done by several authors[7]. There are quite a large ambiguities remaining and the predicted partial lifetime for $p \rightarrow \bar{\nu} K^+$ varies from the order of 10^{29} to 10^{33} yr. For this decay mode, the current experimental lower limit is 1.0×10^{32} obtained in Kamiokande experiment.

Chapter 3

The Super-Kamiokande detector

3.1 Earlier experiments

The first experiment of direct search for nucleon decay was started in 1954 by F.Reines et al, where the stability of protons and bound neutrons was tested. They used liquid scintillator and searched for high energy fragments from nucleon decay. At that time, they obtained 10^{22} yr for the lifetime limit. Similar experiments were performed by several groups and the best limit was 2×10^{30} obtained by Reins et al. in 1974. In the late 1970's, several nucleon decay experiments were proposed motivated by the prediction of nucleon lifetime estimated from the minimal SU(5) GUT. According to this model, the lifetime of nucleon was estimated to be 10^{27} to 10^{31} yr. These experiments necessarily employ the large mass. The detectors are required to have high performance in particle tracking to identify nucleon decay. There are two types of detectors: one is fine grained tracking detectors and the other is water Cherenkov detectors.

Fine grained tracking detectors consist of plates of irons or some other heavy materials and tracking chambers. This type of detector has good position and momentum resolution. Particle types can be identified through the range and ionization yield of tracks. But it is difficult to identify the direction of each particle. Also the total mass is limited to a few kilo-tons.

Water Cherenkov detectors provide good momentum and angular resolution for particles through the pulse height and patterns of the ring images. The particle identification can be made by the pattern of the Cherenkov ring. Also water itself is essentially free and available everywhere and the fiducial volume of a water Cherenkov detector can be scaled up to tens of kilo-tons.

In table3.1, the nucleon decay experiments recently performed or being in operation are summarized.

The Frejus experiment used a new generation tracking calorimeter type detector[12][68]. The detector consisted of iron plates, flash tubes and Geiger tubes and the fiducial volume was 550 metric tons. They did a beam test with a detector configuration close to the real one and the data were used to estimate the background from atmospheric neutrino events. This experiment was started in 1984 and continued until 1988.

The Soudan-II experiment also uses a tracking calorimeter[13]. This detector uses 15mmϕ drift tubes with iron sheets. For the veto counter, there is a proportional tube shield surrounding the main detector. The volume of this detector is not so large but the tracking capability for low energy charged particles is highly improved. They started data taking in 1992 in full operation.

The IMB experiment had been the largest water Cherenkov detector before the Super-Kamiokande detector[14]. The fiducial volume was 3300 metric tons and thus this experiment had given the best lifetime limits for $p \rightarrow e^+\pi^0$ and some other modes. But since their light collection efficiency was smaller than that of Kamiokande, some modes such as $p \rightarrow \nu+$meson modes were background limited. The IMB3 detector was closed in 1992.

The KAMIOKANDE experiment started in 1983 is the predecessor experiment of Super-Kamiokande experiment[15]. The fiducial volume of the detector was 1040 metric tons but they used 984 of 20 inch PMTs (Photo Multiplier Tubes). Its photo-coverage was 20% and the collection efficiency of Cherenkov photons were much higher than the IMB detector. Thus, it had better momentum and vertex resolutions and had higher capability in identifying particles. An anti-detector surrounded the inner detector to veto incoming cosmic-ray muons and to reduce great number of background events.

Experiment (location)	Detector	Depth (m.w.e.)	Fiducial Mass(ton)	operation (year)
KGF-I	10×10 cm^2 prop. tube	7000	60	1980-
(Kolar)	Fe plate			
KGF-II		6050	150	1985-
KGF-III		6050	(80?)	1988-
NUSEX	9×9 mm^2 streamer	5000	110-130	1982-
(Mont Blanc)	tube + FE plate			
Soudan-I	28mmϕ prop. tube	1800	16~24	1981-1990
(Soudan)	+ heavy concrete			
Soudan-II	15mmϕ drift tube	2090		1992-
	+corrugated Fe sheets			
	prop. tube active shield			
Frejus	5×5mm^2 flash tube	4850	550	1984-1988
(Frejus)	$+15\times15$mm^2 gaiger tube			
	+Fe plate			
IMB	Water Cherenkov	1580	3300	1982-1992
(Ohio)	5inchϕ PMT(Phase I)			
	8inchϕ PMT+wave shifter			
	(Phase III)			
KAMOIKANDE	Water Cherenkov	2700	1040	1983-1997
(Kamioka)	20inchϕ PMT			
Super-Kamoikande	Water Cherenkov	2700	22500	1996-
(Kamioka)	20inchϕ PMT			

Table 3.1: Recent experiments

3.2 Overview of the Super-Kamiokande detector

The Super-Kamiokande detector is a ring imaging water Cherenkov detector with 50,000 tons of pure water located 1000m under the ground (2700 meter water equivalent)[Figure 3.1].

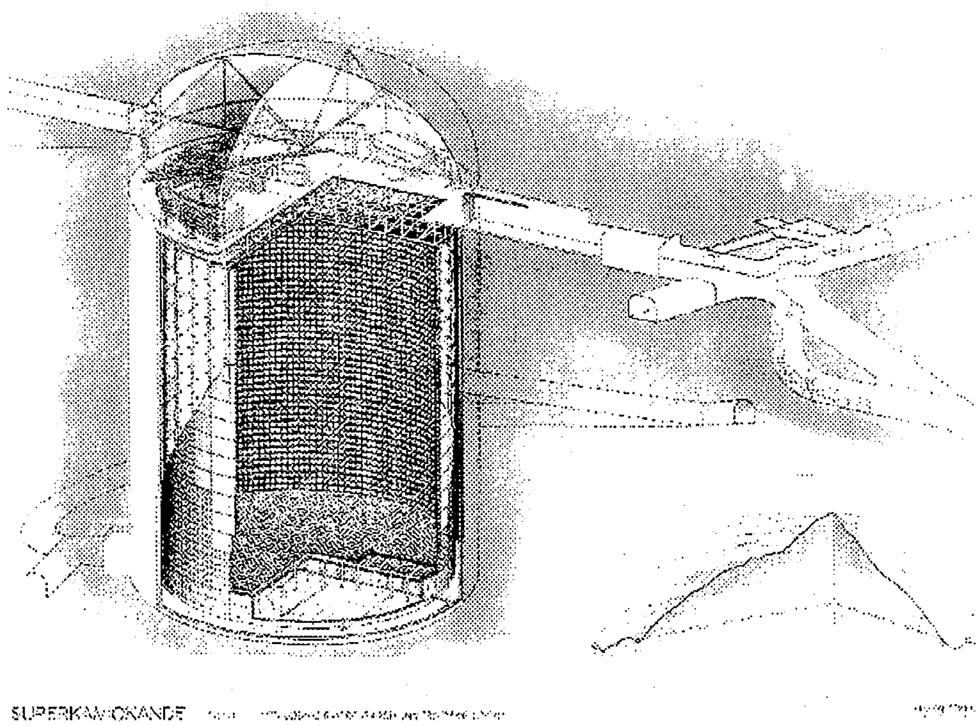

Figure 3.1: Super-Kamiokande detector

The thickness of the rock over the detector reduces the cosmic ray muons down to the level of 10^{-5} and the event rate caused by them is only 3Hz.

The detector uses a cylindrical stainless steel tank to hold water; its size is 39m in diameter and 40m in height. The water tank is optically separated into two sections by the PMT(Photo Multiplier Tube) support structure of which surfaces are covered by Tybek (white reflector sheet) and black-sheet; one is the inner detector and the other is the anti detector[Figure 3.2].

The inner detector is the main part of this detector to search for events of interest. The anti detector is used to identify incoming and outgoing particles. On the wall of the inner detector, 11,146 of 20inch PMTs are mounted and the photo cathode coverage amounts to

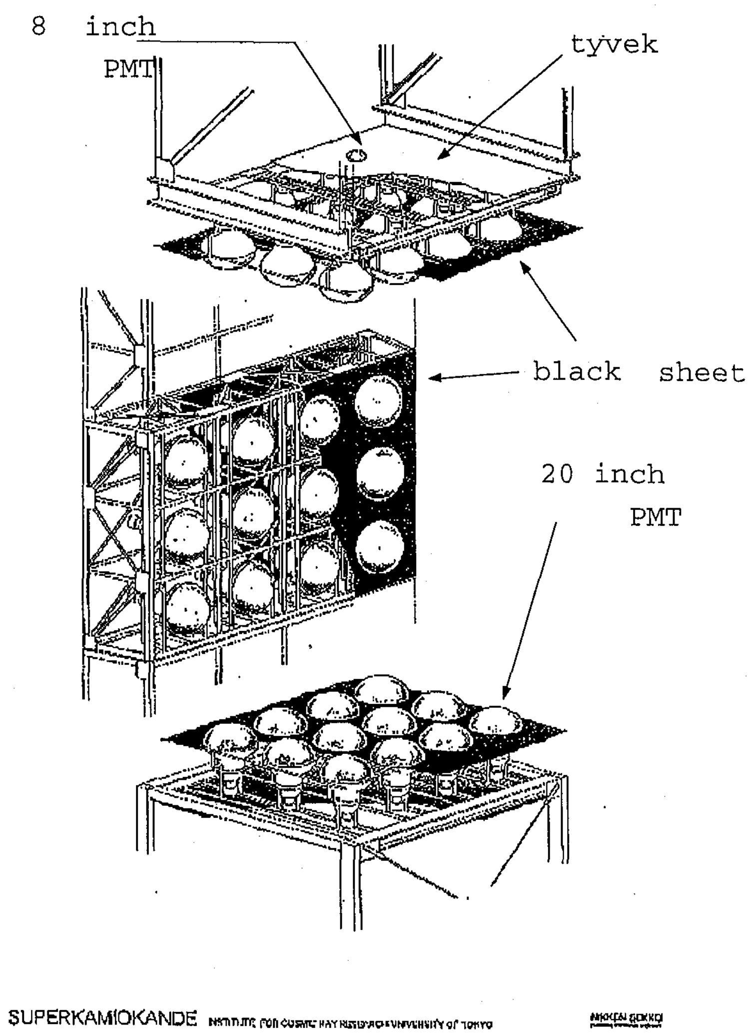

Figure 3.2: PMT support structure used in Super-Kamiokande detector

40% of the inner surface. For the anti detector, we use 1,885 of 8inch PMTs equipped with 60x60cm plates of wavelength-shifter to increase the collection efficiency of the Cherenkov photons.

3.3 Ring imaging Cherenkov technique

If a charged particle runs through material of the refractive index n with velocity more than c/n, Cherenkov light will be emitted. Cherenkov photons are emitted along the direction of the particle in a cone with half angle(θ), which is given by the following equation:

$$\theta = \cos^{-1}(\frac{1}{n\beta}) \tag{3.1}$$

where β=p/E, E and p are the energy and momentum of the particle, respectively.

The spectrum of Cherenkov light per unit length(x) and per wavelength(λ) is given by:

$$\frac{d^2N}{dxd\lambda} = 2\pi\alpha(1 - \frac{1}{n\beta})^2/\lambda^2. \tag{3.2}$$

where α is the fine structure constant. According to this, a particle with $\beta \sim 1$ in water, will emit about 340 photons/cm in the wavelength between 300 and 600nm.

These photons are detected by the PMTs mounted on the surface of this detector. An expanded view of a typical one ring event is shown in Figure 3.3. Each small circle corresponds to a hit PMT and its size is proportional to the pulse-height of each hit. As described before, one Cherenkov-ring corresponds to one charged particle or γ-ray. So we can count the number of such kind of particles in an event by counting the number of rings. The vertex of each event is reconstructed by using the timing and charge information. (For the fitting method, see chapter 6 in detail.) We can also identify the type of each particle by using the shape of the ring. For electrons and γ-rays, electromagnetic cascade showers are generated and the detected shape of the Cherenkov ring image is diffused, while muons and charged mesons generate clear-cut ring images. Typical events of each type are shown in Figures 3.4-(a) and (b). (For particle identification method, see chapter 6 in detail.)

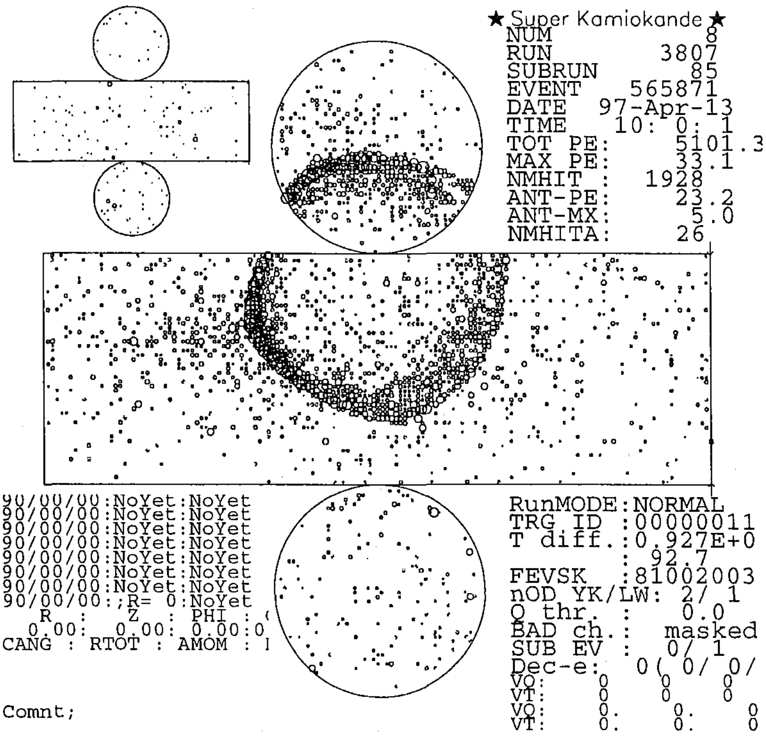

Figure 3.3: An expanded view of a typical one ring event.

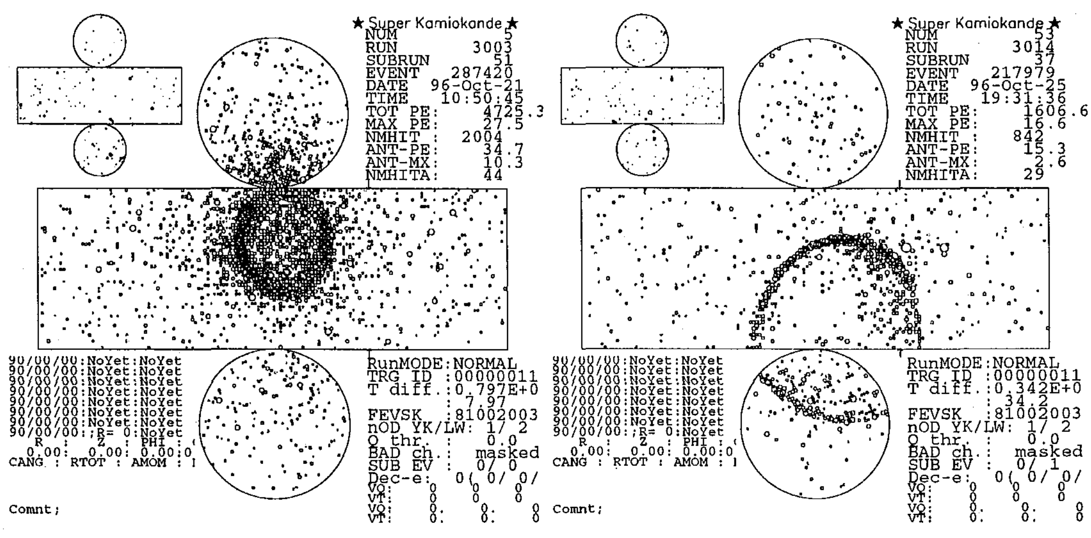

(a) e-like (b) mu-like

Figure 3.4: Typical (a) e-like and (b) mu-like single ring events.

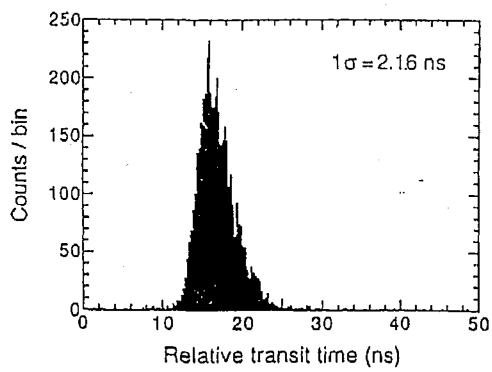

Figure 3.5: Timing resolution of 20inch PMT for single photoelectron.

3.4 Photomultiplier tubes

The 20 inch photomultiplier tubes (PMT) used in Super-Kamiokande have been developed by Hamamatsu Photonics Co. in cooperation with members of Super-Kamiokande Collaboration[16]. PMTs have been much improved compared to the ones used in Kamiokande. The major improvements are:

1) the timing resolution for single photoelectron is reduced to 3ns [Figure 3.5],

2) a clear single photoelectron peak can be observed because of the better electron collection efficiency at each dynodes[Figure 3.6],

3) the tolerance against the earth-magnetic field is increased in help avoiding a use of magnetic shield,

4) waterproof capability has been improved.

The items1) to 3) have been achieved by optimizing the structure of the Venetian blind type dynodes and the breeder chain. The cable and the water shield have been also changed to improve the tolerance to the pressure of the water. These PMTs are operated at a nominal gain of 1×10^7 and the average noise rate of each PMT is 3.6kHz at the 0.25 photoelectron equivalent threshold.

The 8 inch PMTs are also made by Hamamatsu Photonics Co. which were used in the IMB detector. These PMTs are installed with wavelength-shifter plates and due to this, the effective time jitter is about 11ns. They are operated at the gain of 1×10^8 and the average

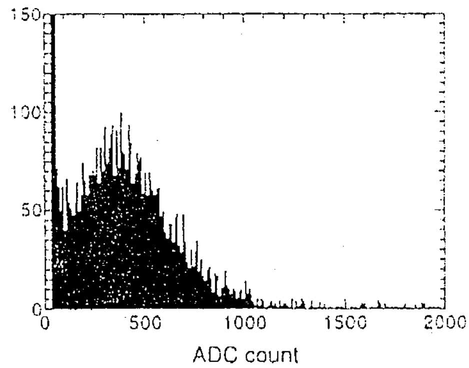

Figure 3.6: Typical single photoelectron peak observed by 20inch PMT.

dark noise rate is around 3kHz measured at the 0.5 photoelectron equivalent threshold.

3.5 DAQ system

The DAQ (Data AcQuisition) system for the Super-Kamiokande detector can be divided into 3 parts: the inner detector, the anti detector and the trigger system.

Inner detector DAQ system

A schematic view of the inner detector DAQ system is shown in Figure 3.7. The inner detector is divided into 8 parts and each detector part works independently. Each part consists of 1 front-end workstation, 1 VME crate and 6 TKO (Tristan KEK Online) boxes. The front-end module is called ATM which stands for the Analog Timing Module[17]. This module has 12 inputs and each individual channel has two local buffers. Each channel has own discriminator and is self-gated. The input signal above the discriminator threshold is stored into its own buffer and after that the internal buffer will be switched to the other. Therefore, basically we can take the subsequent signal without dead time. If there is no trigger coming within $1.3\mu s$, stored signal will be discarded. For each input signal above discriminator threshold, ATM creates a hit signal, which is a rectangular signal of 900ns width. They are summed up within an ATM board. This output signal is called 'hitsum' and used to generate the global trigger. At every 16 triggers, stored events in the ATM are

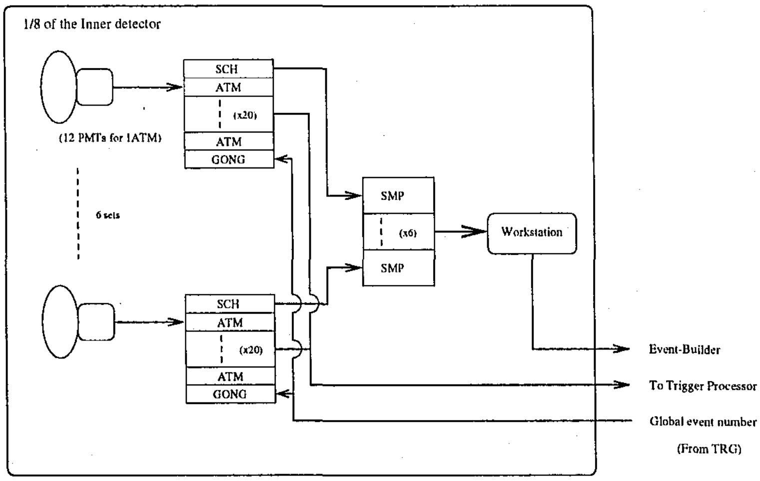

Figure 3.7: Schematic view of the inner detector DAQ system

read out automatically by SMPs (Super Memory Partner) through SCH (Super Control Header). Each SMP has two independent 1MByte memory buffers and by switching these two, SMP can store data from ATMs into one buffer while the workstation is reading data from the other buffer on the same SMP. The front-end workstation reads out the data from SMP before the buffer is filled up.

Anti detector DAQ system

The anti detector uses a completely different electronics system[Figure 3.8]. The signals from each PMT goes into a custom QTC (Charge to Time Converter) card. This card generates a rectangular pulse of which width is proportional to the input charge. The output signal is digitized by LeCroy 1877 multi-hit TDC (Time to Digital Converter). This TDC has 96 input channels per board. This module can record both leading and trailing edges of up to 8 pulses within 32 μs. The position of the trigger in this 32 μs window was initially set to -16 to 16 μs relative to the global trigger timing. But later, this width was changed to -10 to +6 μs to reduce the FIFO overflow caused by the multiple hits due to the PMT signal reflection. The signal reflection depends on the charge of the initial pulse and if the charge is not so much, this effect is almost negligible. But for example, in the cosmic ray muon events, some anti detector PMTs will lose its true timing information.

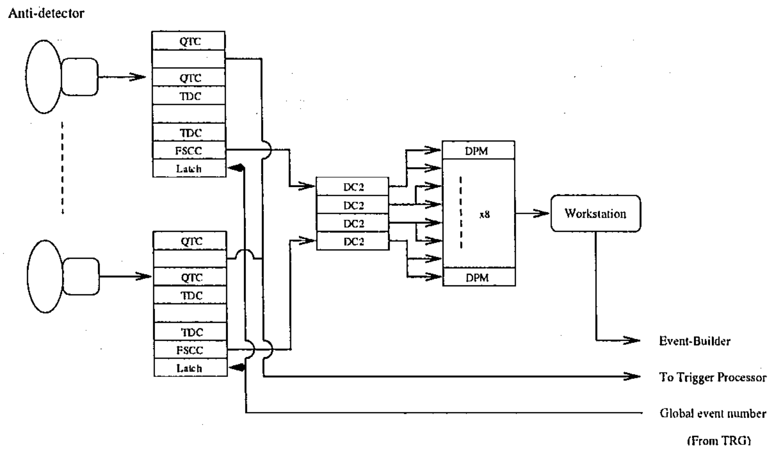

Figure 3.8: Schematic view of the anti detector DAQ system

Like the ATM module, QTC card generates hitsum signal to be used for the anti detector trigger. The digitized data from TDC are read out by the FSCC (FASTBUS Smart Crate Controller) and then sent to the DC2-DM115. The DC2-DM115 latches the TDC data and write to the available DPM (Dual Port Memory) Module. These two DPMs are operated like SMPs. While the DC2-DM115 is writing to one DPM, the data on the other one can be read out from the online front-end workstation.

Trigger system

In the Super-Kamiokande detector, the number of hit PMTs in the certain timing window is proportional to the energy of an electron when its energy is less than a few tens of MeV. Thus, the total number of hit PMTs within 200ns is used for the inner detector trigger discrimination.

At the beginning of the experiment, there were two inner detector triggers called HE (High Energy) trigger and LE (Low Energy) trigger. Both triggers are basically the same and the only difference was the discriminator threshold. The discriminator thresholds were 29 hits equivalent for the LE trigger and 31 hits equivalent for the HE trigger. Both triggers were always sent to the inner and anti detectors[Figure 3.9]. The nominal trigger rate for the LE (HE) trigger was around 12 Hz (5Hz). Both trigger rates were very stable. The anti detector trigger is also used to detect the incoming particles going through the anti detector volume. For this purpose, the number of hit PMTs, similarly to the inner detector, is used for the trigger. By using the real data and Monte Carlo simulations, width of the coincidence window is set to 200ns and the discriminator threshold is adjusted to 19 hit PMTs. The anti detector trigger is always sent to the whole detector system. The trigger rate of the anti detector trigger is around 3Hz and this number is consistent with the event rate of the cosmic ray muons.

After July 1997, the SLE (Super Low Energy) trigger is in operation and at the same time, the triggering scheme has been changed. This change is to take lower energy events for the solar neutrino analysis. The discriminator threshold for the SLE trigger is set at 25 hits equivalent and its trigger rate is around 90Hz. For the analysis of the low energy events, it is not necessary to use the information from anti detector and we decided not to send those triggers to the anti detector. The anti detector cannot catch up at this trigger rate, and the events triggered only by the LE or SLE trigger do not have the information of the anti detector[Figure 3.10].

The trigger handling module used in Super-Kamiokande detector is called TRG. This module can handle 8 independent triggers and generates 16bit global event number and feed this number to the electronics. This module has an internal 50MHz clock and this timing information is also added to each event. These trigger information for each event is read out by an independent workstation.

Online system

Each front-end workstation reads out the data from electronics independently, convert the raw data into a simple online format and sorts events in the order of event numbers. All the information from the detector is collected and merged into an event by the event-builder[Figure 3.11]. Each front-end workstation notifies the event-builder the last event number of data ready to be sent. The event-builder checks these event numbers and request the front-end workstations to send the available events. At the same time, the event-builder is always monitoring the front-end workstations and if something wrong is detected, event-builder will cut off that part issuing a warning message and continue the run without that part.

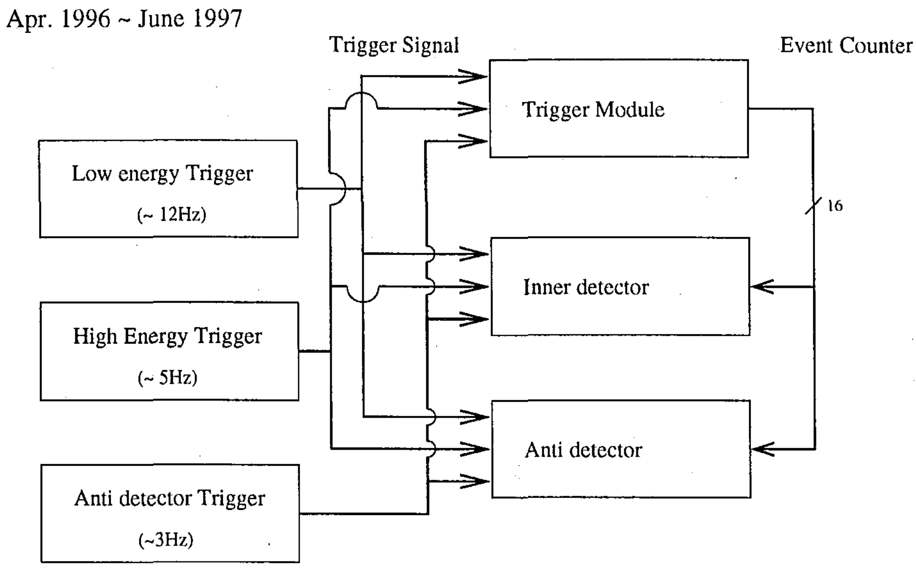

Figure 3.9: Trigger logic in Super-Kamiokande (Apr. 1996 ∼ June 1997)

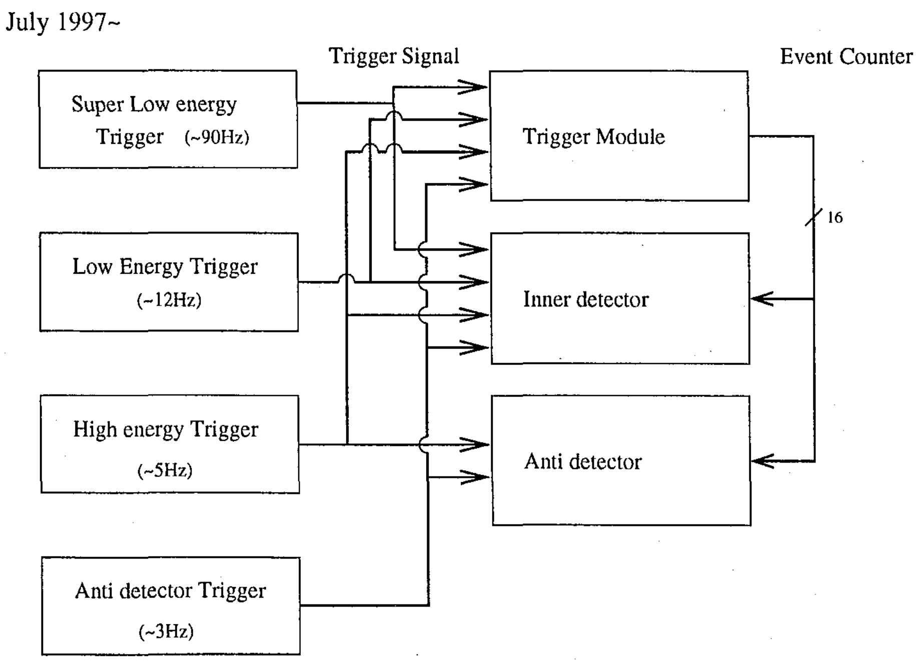

Figure 3.10: Trigger logic in Super-Kamiokande (July 1997 ∼)

There is also a slow-control monitoring system, monitoring such qualities as the status of all the high-voltage supply of the PMTs, measured temperatures and power supply voltage of the electronics. These kinds of information are also added to the event data and sent out to the offline. The data format made up by the event-builder cannot be handled by the offline procedures. The offline format (ZBS, Zebra Bank System) is not proper to this online DAQ system because of its overhead in the size and speed. So it is necessary to convert the data format from the online's to the offline's. This process is called "reformat". For this purpose, another workstation is employed and after this, processed data files are sent to the offline facilities. The workstation on which reformat process is running has 24MBytes of storage area to keep the data for a while.

3.6 Water purification system

It is very important to keep the water clean. The dirty water not only absorbs the Cherenkov photons but also gives out the remaining dusts and gas containing radio isotopes, such as Rn, the decays of which will be one of the major background for the low energy solar neutrino observation. Thus, water in Super-Kamiokande detector is always circulated to keep clean. The schematic view of the water purification system in Super-Kamiokande is shown in Figure 3.12. This system consists of the following elements.

1) Filter to remove dusts ($\sim 1\mu m$).
2) Heat exchanger to keep the water temperature around $14°C$.
3) Ion exchanger to remove metal ions.
4) UV sterilizer to kill bacteria.
5) Vacuum degasifier to remove remaining gas such as oxygen and radon.
6) Cartridge polisher to remove ions.
7) Ultra filter removing small particles($\sim$ 100nm).

As a result, the attenuation length of the photon of which wavelength is 450nm in water is almost 100m.

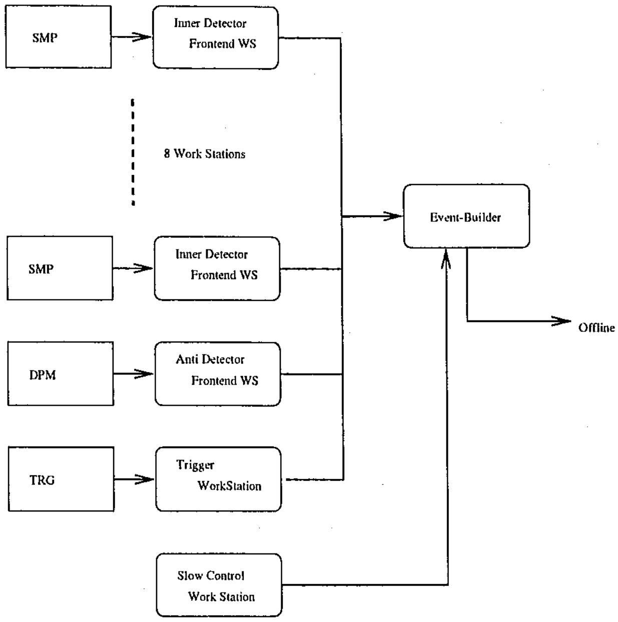

Figure 3.11: Schematic view of online system.

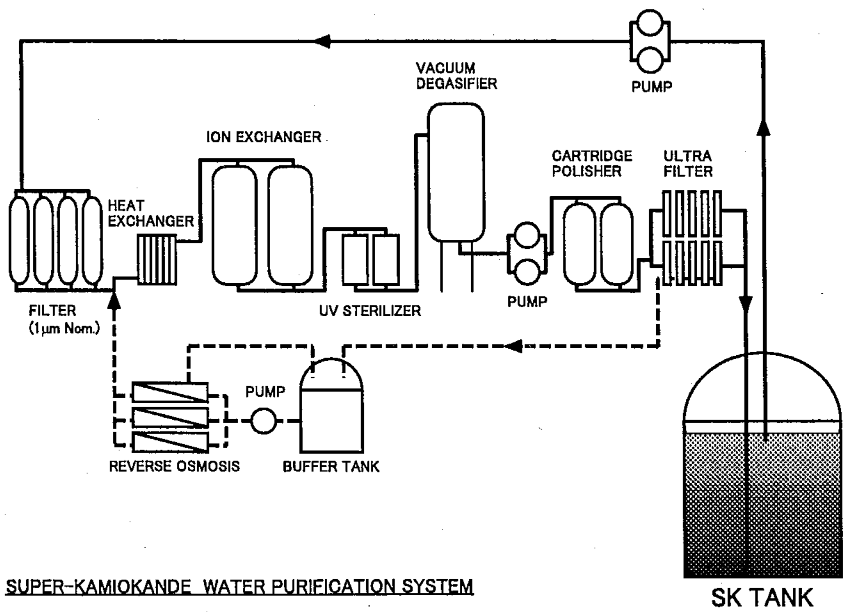

Figure 3.12: Water purification system in Super-Kamiokande.

Chapter 4

Event simulation

In the analysis of proton decay and the estimation of the background, Monte Carlo simulation plays an important role. The characteristics of simulations for proton decay and atmospheric neutrino event are presented here.

4.1 proton decay event simulation

In the Super-Kamiokande detector, proton decay is expected to occur with equal probability among free protons in ^{1}H and bound ones in ^{16}O. The decay of a free proton can be quite simply treated as a usual multi-body decay. The decay of a bound proton needs more careful treatment, because nucleons in ^{16}O carry Fermi momenta and the decay products may interact in the nucleus. The momentum distribution of nucleons in ^{16}O is evaluated from experimental results[18] [Figure 4.1]. The meson-nuclear interactions in ^{16}O are described in section 4.

4.2 Atmospheric neutrino event simulation

Major background for proton decay is the atmospheric neutrino interactions. The event topologies of some atmospheric neutrino interactions are similar to those of proton decays and their vertices also distribute uniformly in the detector.

4.2.1 Atmospheric neutrino fluxes

Primary cosmic-rays, most of which are protons, collide with molecules of the atmosphere and produce hadronic showers. Mesons in this shower decay into neutrinos and muons and these muons also decay into electrons and neutrinos. Atmospheric neutrino fluxes depend on the magnetic latitude since the cut-off energy of primary cosmic-ray protons is affected by geomagnetic field of the earth. Thus, we use Honda's calculation because his calculation has been done at the magnetic latitude of the Kamioka and covers the neutrino energy from 10MeV to 1TeV[19] [Figure 4.2]. Gaisser has also calculated the neutrino fluxes at the Kamioka site and we compare them to estimate the systematic errors[20] [Figure 4.3]. The discrepancy between these two calculations is less than ±10%.

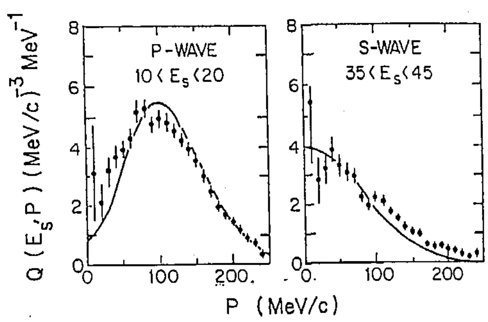

Figure 4.1: Fermi Momentum distribution of nucleons in ^{12}C[18].

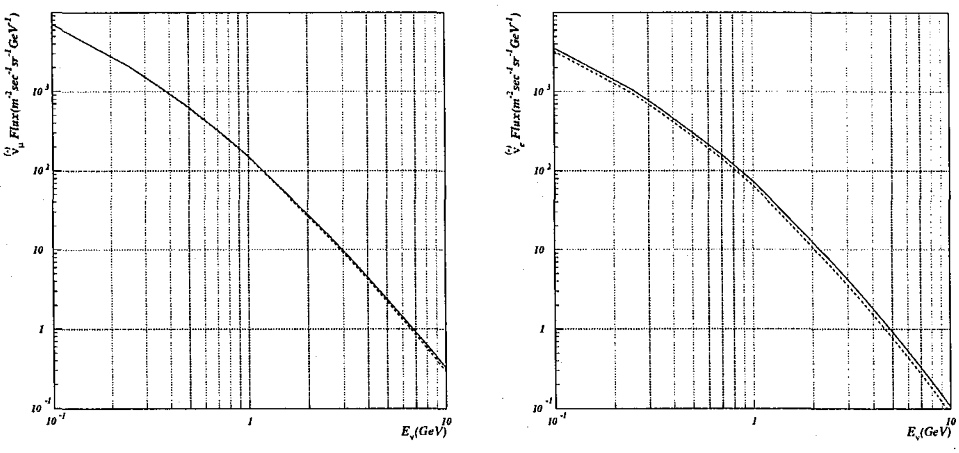

(a) (b)

Figure 4.2: Calculated atmospheric neutrino fluxes by Honda. (a) shows the ν_μ and $\bar{\nu_\mu}$ and (b) shows the ν_e and $\bar{\nu_e}$. The solid lines show the fluxes of neutrino and the dotted lines show the fluxes of anti neutrino.

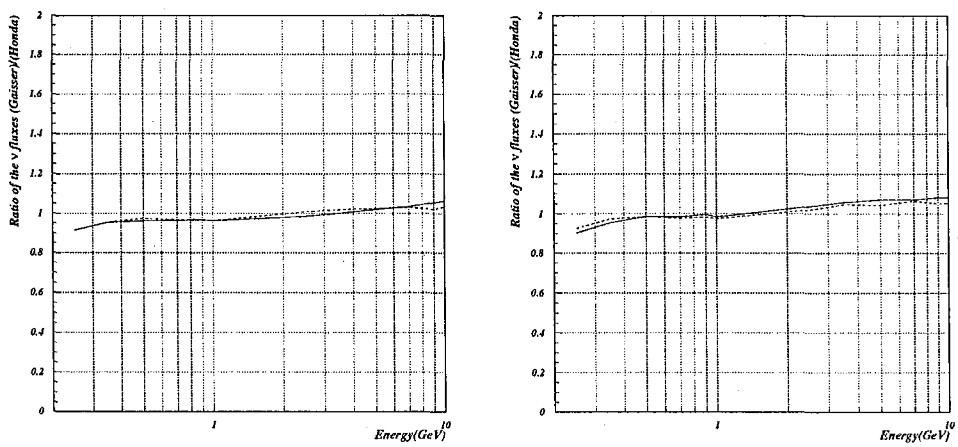

(a) (b)

Figure 4.3: Comparison between the calculated atmospheric neutrino fluxes by Gaisser and Honda. (a) shows the ν_μ and $\bar{\nu_\mu}$ and (b) shows the ν_e and $\bar{\nu_e}$. The solid lines show the fluxes of neutrino and the dotted lines show the fluxes of anti neutrino.

4.2.2 Neutrino interactions

In our Monte Carlo simulation, the following neutrino interactions are considered:

Charged Current quasi-elastic scattering	(	$\nu\ N$	$\rightarrow$	$l\ N'$	),
Neutral Current elastic scattering	(	$\nu\ N$	$\rightarrow$	$\nu\ N$	),
Charged Current single π production	(	$\nu\ N$	$\rightarrow$	$l\ N'\ \pi$	),
Neutral Current single π production	(	$\nu\ N$	$\rightarrow$	$\nu\ N'\ \pi$	),
Charged Current multi π production	(	$\nu\ N$	$\rightarrow$	$l\ N'\ n\pi$	),
(Neutral Current multi π production)	(	$\nu\ N$	$\rightarrow$	$\nu\ N'\ n\pi$	),
Charged Current coherent π production	(	$\nu\ ^{16}O$	$\rightarrow$	$l^{\pm}\ \pi^{\mp}\ X$	),
Neutral Current coherent π production	(	$\nu\ ^{16}O$	$\rightarrow$	$\nu\ \pi^0\ X$	),

where N and N' are the nucleons (proton or neutron), l is the charged lepton, $n(=1,2,3...)$ is the multiplicity of pions and X is the remaining nucleus. The other interaction modes such as a strange particle production is not included in this simulation, because its production probability is small enough to neglect compared to the above interactions. For the neutrino kaon production, its effect is estimated from the existing neutrino experimental results.

Elastic and quasi-elastic scattering

The cross sections for the quasi elastic charged current interaction can be written in terms of hadronic current,

$$< N'|J_{had,\lambda}|N > \;=\; cos\theta_c\bar{u}(N')[\gamma_\lambda F_V^1(q^2) + \frac{i\sigma_{\lambda\nu}q^\nu\xi F_V^2(q^2)}{2M} + \gamma_\lambda\gamma_5 F_A(q^2)]u(N) \quad (4.1)$$

where F_V^1, F_V^2 are the vector form factors, F_A is the axial-vector form factor, $\xi \equiv \mu_p - \mu_n = 3.71$, θ_c is the Cabibbo angle[21]. The parameters of the form factors are determined from the experiments[22]. If the target is a free proton, the q^2 dependence of the cross sections is directly calculated from this equation and the results are shown in Figure 4.4 and Figure 4.6.

In estimating the cross sections of neutral current elastic scattering, we use the following relations[27]:

$$\sigma(\nu p \rightarrow \nu p) \;=\; 0.153 \times \sigma(\nu n \rightarrow e^- p),$$

$$\sigma(\bar{\nu}p \to \bar{\nu}p) = 0.218 \times \sigma(\bar{\nu}p \to e^+n),$$
$$\sigma(\nu n \to \nu n) = 1.5 \times \sigma(\nu p \to \nu p),$$
$$\sigma(\bar{\nu}n \to \bar{\nu}n) = 1.0 \times \sigma(\bar{\nu}p \to \bar{\nu}p).$$

For the $\nu^{16}O$ scattering, Fermi motion of the nucleon and Pauli principle have to be taken into account. The momentum distribution of nucleons in ^{16}O is estimated from the experimental data of electron ^{12}C scattering[18] [Figure 4.1]. For the Pauli blocking effect, we assume the Fermi gas model and require the momentum of the recoil nucleon to be greater than the Fermi surface momentum. The calculated cross sections for $\nu^{16}O$ scattering are shown in Figure 4.5.

Single pion production

We adopt Rein-Sehgal's method to simulate this interaction[28]. In their method, this type of interaction is separated into two parts as follows.

$$\nu + N \to l + N^*,$$
$$N^* \to \pi + N',$$

where N and N' are the nucleons, N^* is the baryon resonances. To obtain the cross sections, we calculate the amplitude of each resonance production and after that multiply the probability of decay into one pion and nucleon to each resonance. At this time, interferences among the resonances are also taken into account. In calculating the cross sections for this interaction, 18 resonances below 2GeV are considered but to keep the consistency with multi pion production in our simulation, the hadronic invariant mass(W), which is the mass of intermediate resonance, is restricted to be less than 1.4GeV. The cross sections of single pion productions are shown in Figures 4.7-(a),(b) and (c).

In the calculation of the angular distribution of pion in the final state, we use Rein-Sehgal's model for the $P_{33}(1232)$ resonance, which is dominant in the region of W below 1.4GeV. For the other resonances, the distribution of direction of generated pion is set to be isotropic in the Adler Frame (resonance rest frame) [Figure 4.8]. We can calculate the single pion production cross sections for each single resonance and the intermediate resonance can be determined using them. The angular distribution of π^+ has been measured for $\nu p \to \mu^- p \pi^+$ mode[31]. Figure 4.9 shows the result of our Monte Carlo simulation and the measured value.

Multi pion production

The total cross section of this interaction is calculated by integrating eqn.4.2 in the range of $W > 1.3$GeV/c, where W is the invariant mass of the hadronic system:

$$\begin{aligned}
\frac{d^2\sigma}{dxdy} &= \frac{G_F^2 M_N E_\nu}{\pi}((1-y+\frac{1}{2}y^2+C_1)F_2(x,q^2) \pm y(1-\frac{1}{2}y+C_2)[xF_3(x,q^2)]), \quad (4.2) \\
C_1 &= \frac{yM_l^2}{4M_N E_\nu x} - \frac{xyM_N}{2E} - \frac{M_l^2}{4E_\nu^2} - \frac{M_l^2}{2M_N E_\nu x}, \\
C_2 &= -\frac{M_l^2}{4M_N E_\nu x},
\end{aligned}$$

where $x = -q^2/(2M(E_\nu - E_l))$, $y = (E_\nu - E_l)/E_\nu$, M_N is the mass of nucleon, M_l is the mass of lepton, E_ν and E_l are the energy of incoming neutrino and outgoing lepton in the laboratory frame, respectively. The nucleon structure functions, F_2 and xF_3 are taken from the result of CCFR experiment[32]. Total charged current cross sections including quasi-elastic scattering, single and multi pion productions are shown in Figures 4.10 and 4.11.

The mean multiplicity of charged pions($\langle n_\pi \rangle \geq 1$) is estimated from the result of Fermilab 15-foot hydrogen bubble chamber experiment[44],

$$\langle n_\pi \rangle = 0.09 + 1.83 \ln W^2. \tag{4.3}$$

The value of W is determined assuming the KNO scaling[45] [Figure 4.12]. The forward-backward asymmetry of pion multiplicity(n_π^F/n_π^B) in the hadronic center of mass system is also included as follows:

$$\frac{n_\pi^F}{n_\pi^B} = \frac{0.35 + 0.41\ln(W^2)}{0.5 + 0.09\ln(W^2)}. \tag{4.4}$$

This value is obtained from the result of BEBC experiment[46].

To obtain the cross sections for multi pion production induced by the neutral current, we use the following relations:

$$\frac{\sigma(\nu N \to \nu X)}{\sigma(\nu N \to \mu^- X)} = 0.26 \ (E_\nu \leq 3GeV), \tag{4.5}$$

$$\frac{\sigma(\nu N \to \nu X)}{\sigma(\nu N \to \mu^- X)} = 0.26 + 0.04 \times ((E_\nu - 3.)/3.)\ (3GeV < E_\nu < 6GeV), \tag{4.6}$$

$$\frac{\sigma(\nu N \to \nu X)}{\sigma(\nu N \to \mu^- X)} = 0.30\ (E_\nu \geq 6GeV), \tag{4.7}$$

$$\frac{\sigma(\bar{\nu} N \to \bar{\nu} X)}{\sigma(\bar{\nu} N \to \mu^+ X)} = 0.39\ (E_\nu \leq 3GeV), \tag{4.8}$$

$$\frac{\sigma(\bar{\nu} N \to \bar{\nu} X)}{\sigma(\bar{\nu} N \to \mu^+ X)} = 0.39 - 0.02 \times ((E_\nu - 3.)/3.)\ (3GeV < E_\nu < 6GeV), \tag{4.9}$$

$$\frac{\sigma(\bar{\nu} N \to \bar{\nu} X)}{\sigma(\bar{\nu} N \to \mu^+ X)} = 0.37\ (E_\nu \geq 6GeV). \tag{4.10}$$

These values are estimated from the experimental results[47][48].

Coherent pion production

The differential cross section of coherent pion production can be expressed as follows[49]:

$$\frac{d^3\sigma}{dQ^2 dy dt} = \frac{G^2 M_N}{2\pi^2} f_\pi^2 A^2 E_\nu (1-y) \frac{1}{16\pi} [\sigma_{tot}^{\pi N}]^2 (1+r^2) (\frac{m_A^2}{m_A^2 + Q^2})^2 e^{-b|t|} F_{abs}, \tag{4.11}$$

$$r = \mathrm{Re} f_{\pi N}(0) / \mathrm{Im} f_{\pi N}(0),$$

where G is the weak coupling constant, M_N is the mass of nucleon, $f_\pi = 0.93 m_\pi$, $y = (E_\nu - E_l$ E_ν and E_l are the energy of neutrino and outgoing lepton, respectively and A(=16) is the atomic number of oxygen. F_{abs}, which accounts for the absorption of pion in the nucleus, is expressed as follows:

$$F_{abs} = e^{-\langle x \rangle / \lambda}, \tag{4.12}$$

$$\lambda^{-1} = \sigma_{inel}^{\pi N} \rho$$

where $\langle x \rangle$ is the average path length of the pion in oxygen and $\rho = A(\frac{4\pi}{3} R^3)^{-1}$ is the nuclear density. Calculated cross sections for coherent pion productions are shown in Figure 4.13.

4.3 Meson nuclear effect

The interactions of the mesons, especially of pions, which are generated in a ^{16}O nucleus, is important in estimating the efficiency and expected background from atmospheric neutrino interactions. Because the cross section of neutrino pion production is quite large around a few GeV which is the same energy region of the pions emitted from proton decay. Also the interaction cross section of pion in nuclei is large. In our Monte Carlo simulation program, the following pion interactions in ^{16}O are considered: inelastic scattering, charge exchange and absorption. In simulating the pion interactions, we followed the philosophy of the cascade model. The actual procedure is as follows. The generated position of the pion in nuclei is set according to the Woods-Saxon type nucleon density distribution. The interaction mode is determined by using the calculated mean free path of each interaction. To calculate these mean free paths, we adopt the model by Oset et al[50]. In the calculation, Fermi motion of the nucleon in ^{16}O and the Pauli-blocking effect are included and the calculated mean free paths depend not only on the momentum of pion but also on the position of pion in the nucleus. If the inelastic scattering or the charge exchange occurs, the direction and momentum of pion are determined by using the result of phase shift analysis obtained from the $\pi - N$ scattering experiments[51]. When calculating the pion scattering amplitude, the Pauli blocking effect is also taken into account by requiring the nucleon momentum after interaction to be larger than the Fermi surface momentum ($p_F(r)$) at the interacting point defined as follows:

$$p_F(\mathbf{r}) = [\frac{3}{2}\pi^2\rho(\mathbf{r})]^{-\frac{1}{3}}, \tag{4.13}$$

where $\rho(\mathbf{r}) = \frac{\mathrm{Z}}{\mathrm{A}}\bar{\rho}\{1 + \exp(\frac{|\mathbf{r}| - \mathrm{c}}{\mathrm{a}})\}^{-1}$,

A: Atomic Number , Z: Number of protons

$\bar{\rho}$: Average density of nucleus

a,c : density parameter of nucleus.

This pion interaction simulation is tested by using the following three interactions:

- π^{12}C scattering,
- π^{16}O scattering,
- pion photo-production ($\gamma +^{12} C \rightarrow \pi^- + X$).

To simulate the pion photo-production, we use the measured cross section for primary interaction ($\gamma + n \rightarrow \pi^- + p$)[52]. The results of each simulation and comparison with the existing experimental results are shown in Figures 4.14-4.16.

The interactions of K^+ in ^{16}O are also important in analyzing $p \rightarrow \bar{\nu}K^+$ mode (momentum of K^+ is around 340MeV/c). But in this case, we are only interested in the charge exchange interaction of K^+, because the momentum of the K^+ is below the threshold energy for the Cherenkov light emission and the elastic and inelastic scattering will not affect the analysis. Among possible charge exchange interactions of K^+ at low energy, $K^+n \rightarrow K^0p$ has the largest cross section. Its cross section was measured for 340MeV/c K^+ to be only 3 ± 0.5mb[56]. From this result, the probability of charge exchange interaction is estimated to be 2.4% through Monte Carlo simulation[57].

4.4 Detector simulation

For the particle tracking part of simulation, we use GEANT package developed at CERN which is commonly used in high energy physics experiments. For the hadronic interactions in water, we choose CALOR package, which is based on the nuclear cascade model[58]. This package gives good agreement with the data even for the pion interactions below 1GeV/c. But reproducibility of the low energy pion interactions (for momentum less than 500MeV/c) is not enough for our experiment and there is no available simulator packages which have good agreement with other π-nucleus scattering data. Thus, we have prepared our own code which uses the cross sections of $\pi - H_2O$ estimated from the results of existing π scattering experimental results to determine the interactions of π[59][60][61].

Cherenkov photon radiation is also done in the GEANT package. But the tracking part of Cherenkov photons is developed for this experiment. For the short wave light scattering, Rayleigh scattering is known to dominate if the size of particle with which Cherenkov photons interact is small compared to the wavelength. So we take into account this scattering. For the longer wavelength, measured wavelength dependences of the light scattering and absorption are used. There are two method to measure the attenuation length of photon in water: one is the direct measurement by laser and the other is an indirectly measurement by using the through going muons. Figure 4.17 shows the attenuation length used in our simulation program and the results of direct water transparency measurement.

The effective quantum efficiency of photomultiplier and the response of them and electronics have been measured. Based on these results, Cherenkov photon detection part was developed.

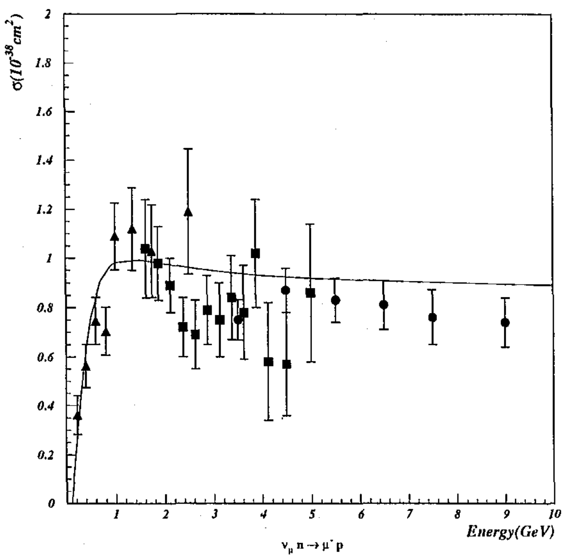

(a)

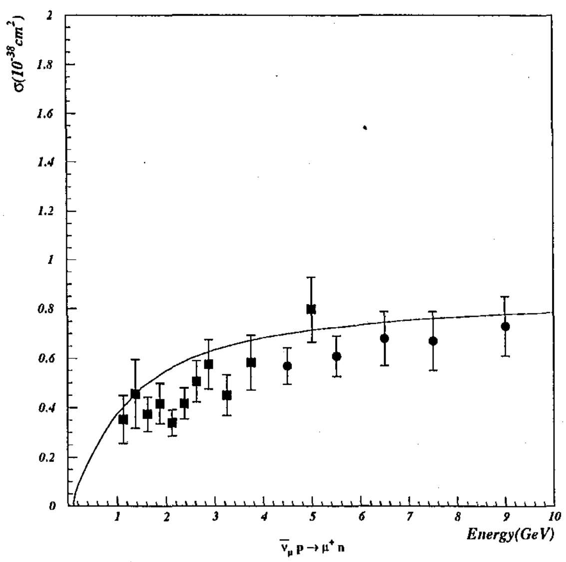

(b)

Figure 4.4: Cross sections of ν_μ(a) and $\bar{\nu}_\mu$(b) charged current quasi-elastic scattering. The solid lines show the calculated cross sections. Data points are taken from the following experiments: Figure(a): (▲)ANL[23], (■)GGM[24], (●)Serpukhov[25]. Figure(b): (■)GGM[26], (●)Serpukov[25].

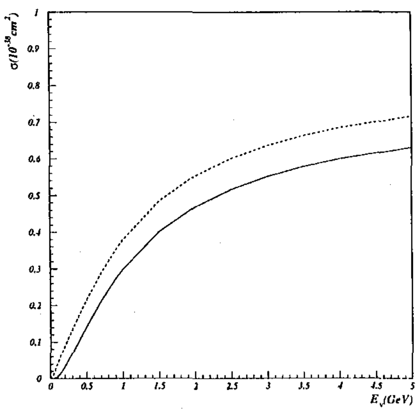

Figure 4.5: Cross section of $\bar{\nu}_e p \to e^+ n$ for bound proton in the ^{16}O and for free proton. Solid line corresponds to the bound proton (in the ^{16}O) and dashed line corresponds to the free proton.

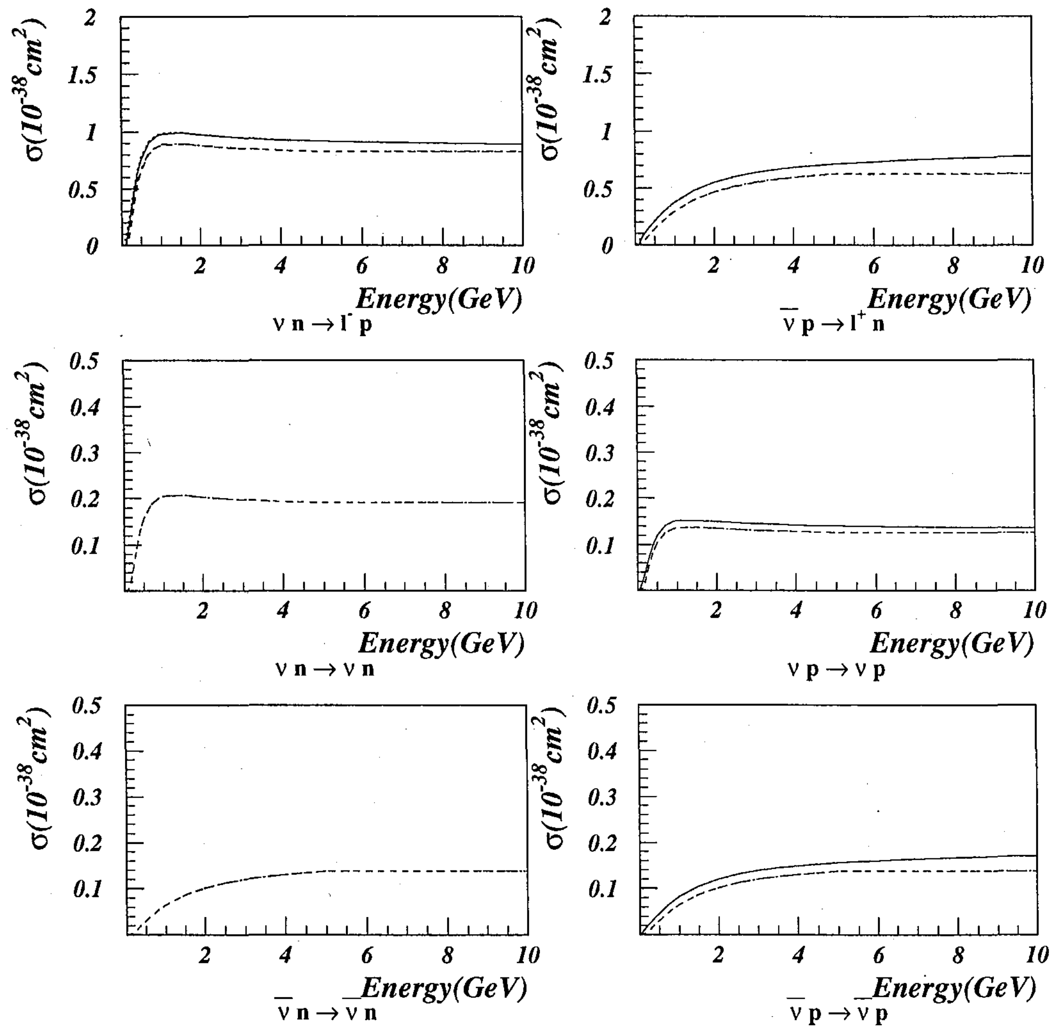

Figure 4.6: Cross sections of ν and $\bar{\nu}$ (quasi) elastic scattering. Solid lines show the cross sections for neutrino-free proton scattering. Dashed lines shows the cross sections for neutrino-bound nucleon scattering.

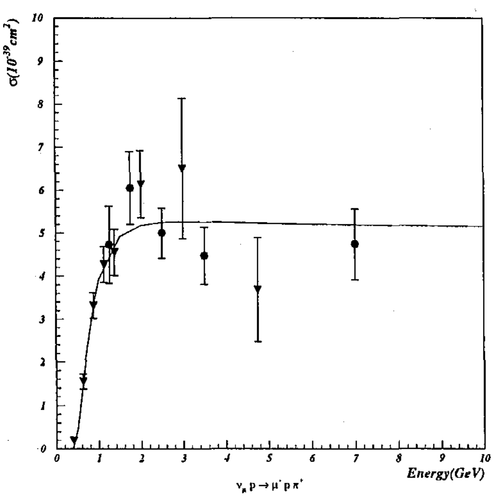

(a)

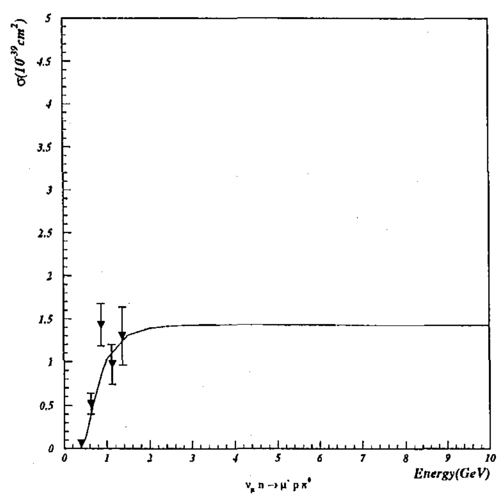

(b)

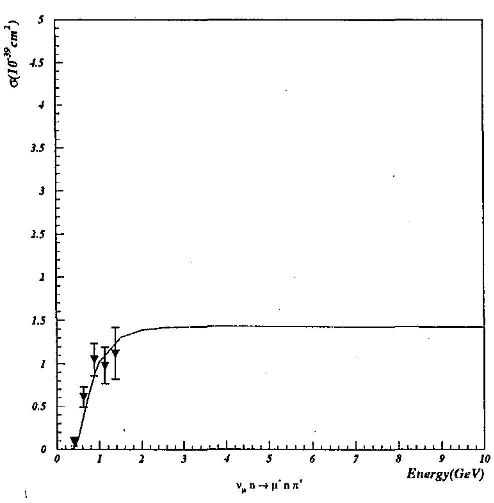

(c)

Figure 4.7: Cross sections of (a)$\nu_\mu p \rightarrow \mu^- p \pi^-$, (b)$\nu_\mu n \rightarrow \mu^- p \pi^0$, (c)$\nu_\mu n \rightarrow \mu^- n \pi^+$. Solid lines show the calculated cross sections. Data points are taken from the following experiments: (▼)ANL[29], (●)GGM[30].

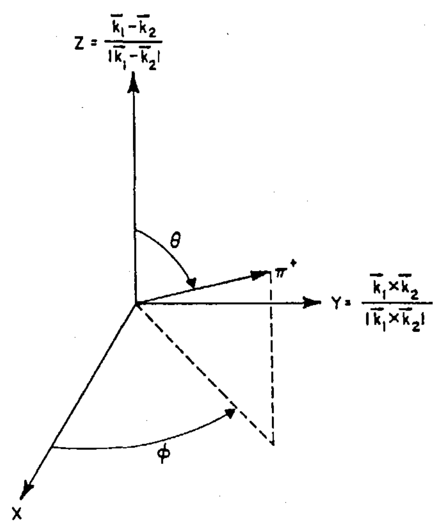

Figure 4.8: Definition of the Adler frame. $\vec{k_1}$ and $\vec{k_2}$ are the 4-momentum of incoming and outgoing lepton, respectively.

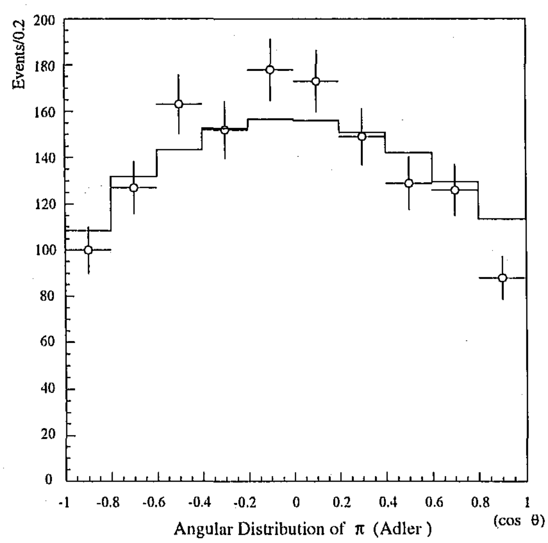

Figure 4.9: Distribution of π^+ for $\nu p \to \mu^- p \pi^+$ mode. The data points are taken from Ref.[31].

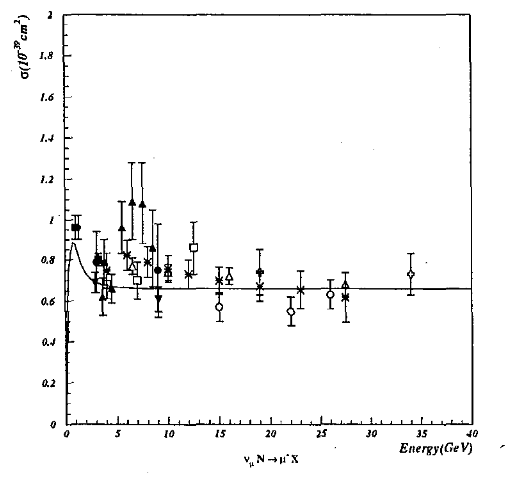

Figure 4.10: Neutrino charged current total cross section. Solid line shows the calculated cross section. Data points are taken from the following experiments: (▲)GGM73[33], (▼)GGM79[34], (○)GGM81[35], (□)SKAT79[36], (+)BEBC79[37], (△)IHEP79[38], (◆)ANL79[39], (●)BNL80[40], (■)BNL81[41], and (×)IHEP96[42].

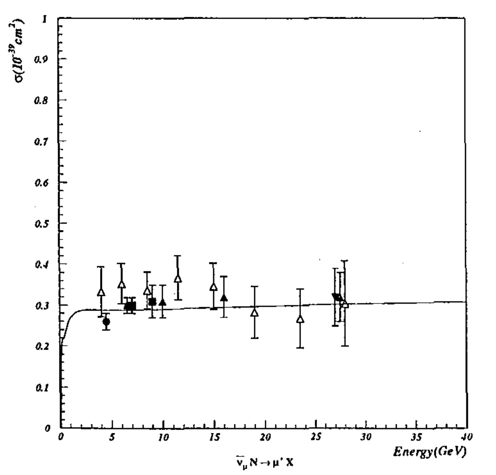

Figure 4.11: Anti neutrino charged current total cross section. Solid line shows the calculated cross section. Data points are taken from the following experiments: (●)GGM79[43], (■)GGM81[35], (△)IHEP79[38], (▲)IHEP96[42].

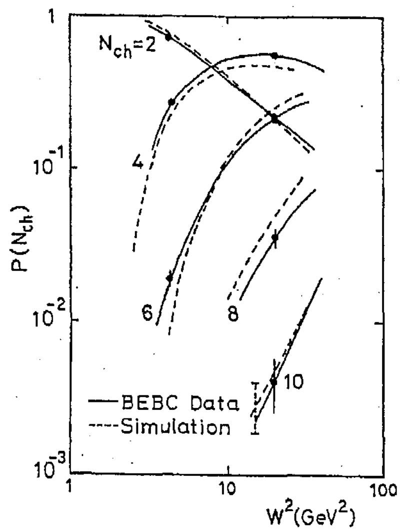

Figure 4.12: Charged particle multiplicity distributions using the KNO scaling. [45]

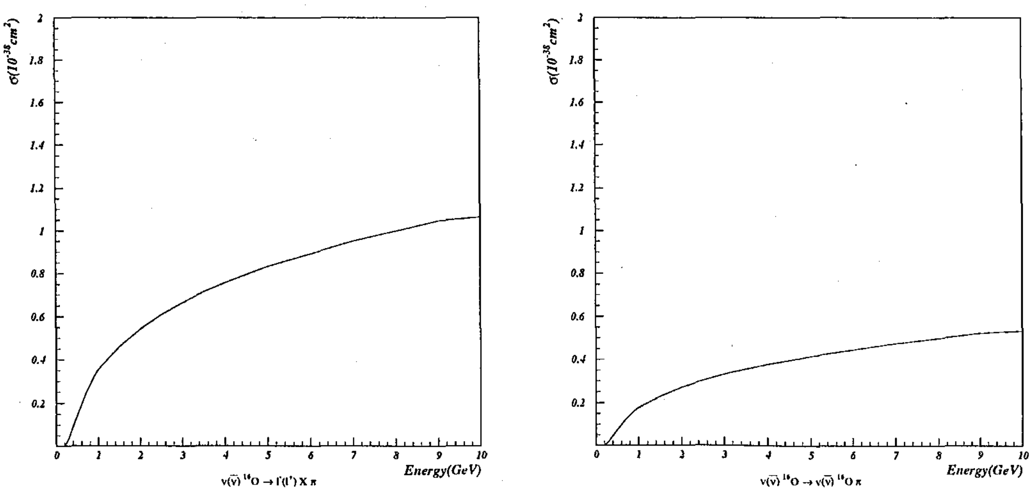

(a) (b)

Figure 4.13: Cross sections of charged current(a) and neutral current(b) coherent pion production.

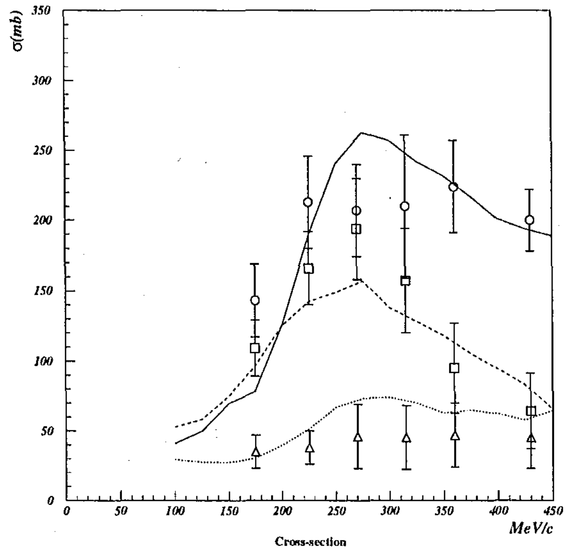

Figure 4.14: Interaction cross sections of $\pi^+ +^{12} C$ scattering. Data points are taken from ref.[53].

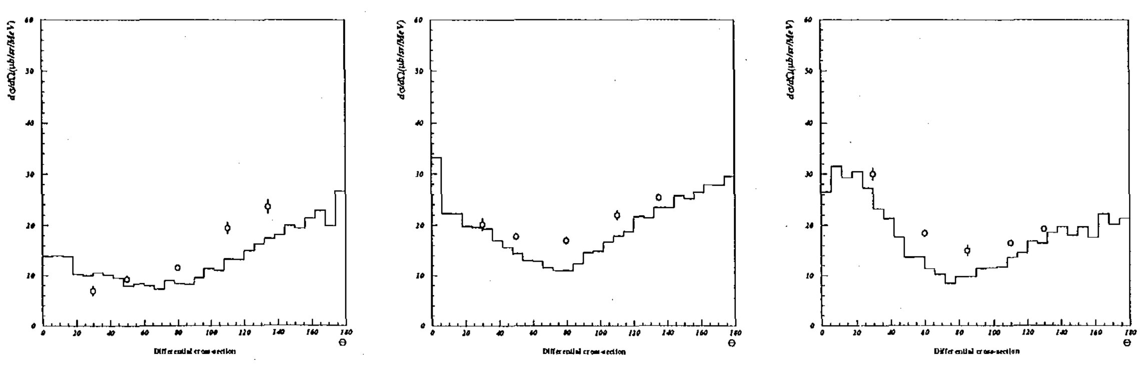

(a)$P_\pi = 213$MeV/c (b)$P_\pi = 268$MeV/c (c)$P_\pi = 353$MeV/c

Figure 4.15: Differential cross sections of $\pi^+ +^{16} O$ scattering. The data points are taken from ref.[54].

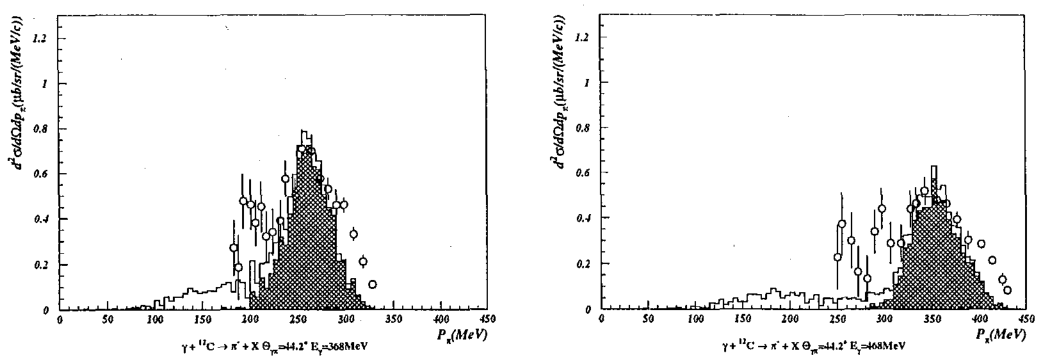

(a)$E_\gamma = 368MeV/c$ (b)$E_\gamma = 468MeV/c$

Figure 4.16: Differential cross section of π^- photo-production. Data points are taken from ref.[55]. The hatched region shows the πs which escaped from the ^{12}C without any interactions.

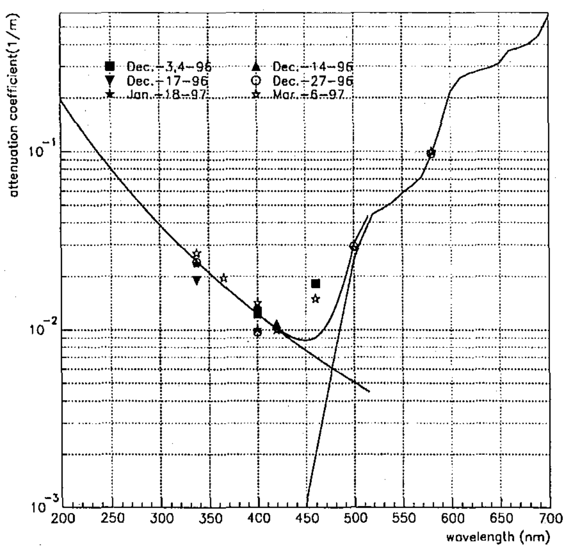

Figure 4.17: Attenuation length of the photon in water. Solid line shows the attenuation length used in the Monte Carlo simulation. Data points show the results of the direct measurements.

Chapter 5

Data reduction

In Super-Kamiokande, the nominal trigger rate is about 12Hz (90Hz after installation of the Super Low Energy Trigger) and it has been very stable. About 3Hz is from cosmic-ray muons and the remaining is from low energy events. Thus we have to reject large fraction of unnecessary events before doing detailed analysis for proton decay.

In this chapter, the data reduction scheme is described. Figure 5.1 shows the reduction steps for the proton-decay and atmospheric neutrino analysis.

5.1 1st and 2nd reduction

At the 1st reduction stage, we apply very loose cuts to reject low energy events and cosmic-ray muons. A typical cosmic-ray muon event is shown in Figure 5.2.

Low energy events are rejected by requiring total charge of the inner detector within 300ns window is more than 200 p.e. (photo electrons), which corresponds to 23MeV/c for electron, while cosmic-ray muon events are rejected by requiring the number of hit PMTs of the anti detector within 800ns window to be less than 50. After this reduction, the number of remaining events is about 4000 events/day.

Next, we apply tighter cuts to reject low energy events with accidental noise hits by requiring (maximum number of p.e. in one PMT)/(Total p.e. of the event) is less than 0.5 and cosmic-ray muon events by requiring the number of hit PMTs of the anti detector within 800ns window is less than 25. The number of hit PMTs of the anti detector within

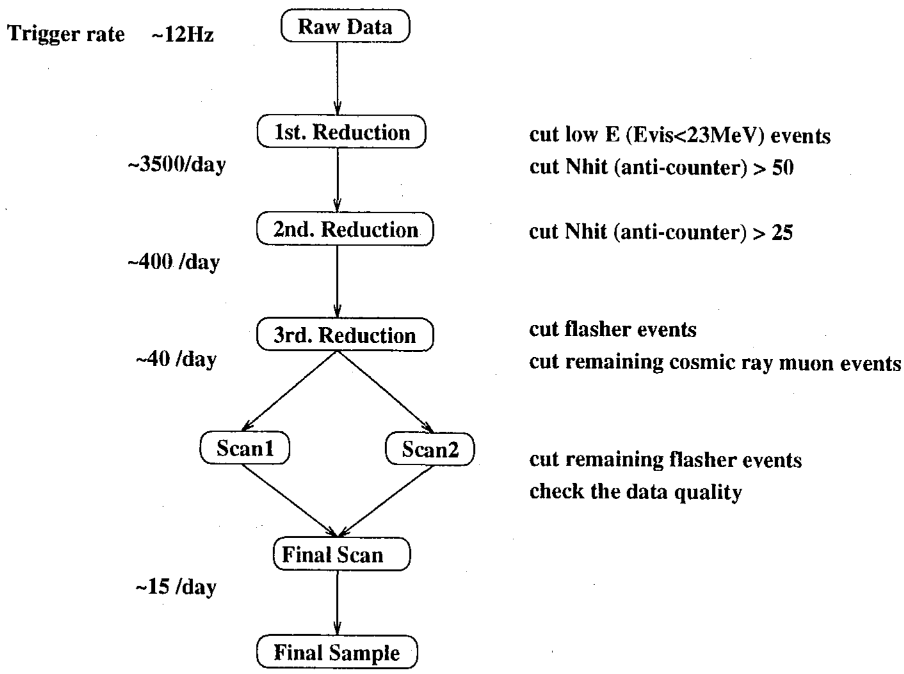

Figure 5.1: Reduction steps for the proton decay and atmospheric neutrino analysis.

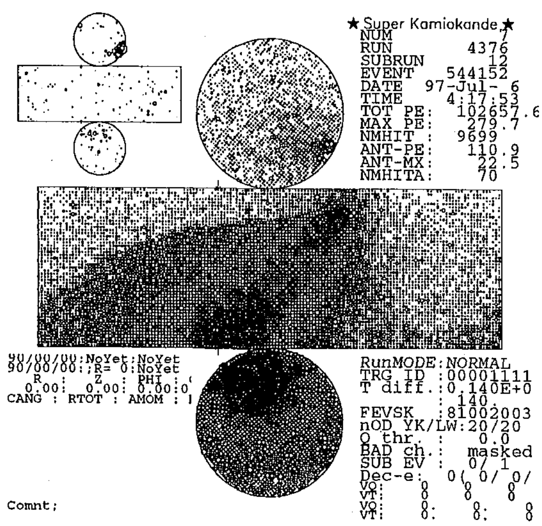

Figure 5.2: Typical cosmic-ray muon event.

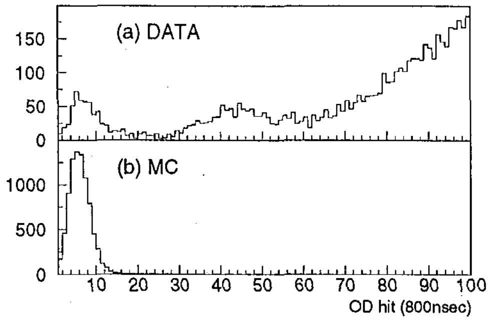

Figure 5.3: Number of hit PMTs of the anti detector within 800ns. Fig.(b) shows the atmospheric neutrino Monte Carlo events.

800ns is shown in Figure 5.3. Based on Figure 5.3-(b), the latter criterion of the second reduction has been determined. After this reduction, the number of remaining events is about 500 events/day.

5.2 3rd reduction

To further reduce events after the 2nd reduction, we apply tighter cuts to reject remaining noise events, cosmic-ray muon events, etc. The 3rd reduction is separated into six parts.

Rejection of through going muon events

The remaining through going muon events have fewer number of hit PMTs in the anti detector and cannot be easily rejected. Thus we use the fitted result of the muon track and count the number of hit PMTs in the anti-detector around the entrance and exit points[62]. Events which satisfy all the conditions below are rejected:

- one or more PMTs have p.e. more than 230,
- the number of hit PMTs in the inner detector is more than 1000,
- the number of OD-cluster hits for the entrance or exit of the particle is more than 9, where OD-cluster hits are hit PMTs of the anti detector in 800ns window within the

radius of 8m from the entrance or the exit point of the particle.

Rejection of stopping muon events

There are also cosmic-ray muons which come and stop in the detector. This type of events is rejected also by fitting the muon track and count the number of hit PMTs of the anti detector around the entrance. The stopping muon fitter assumes the location of the PMT having the earliest signal to be the entrance point. The direction of the muon is determined by maximizing the total charge in the Cherenkov cone. The *goodness* of this fit has the same definition as that of the TDC fit. (See chapter 6 for detail.) Events which satisfy one of the following two conditions are rejected:

- the number of OD-cluster hits at the entrance is more than 9,
- the *goodness* of the stopping-muon fit is greater than 0.5 and the number of OD-cluster hits at the entrance is more than 4.

For proton decay events and fully contained atmospheric neutrino events, the number of OD-cluster hits is at most 2.

Rejection of low energy events

To reject low energy events with noise hits, we apply a low-energy specific fitting program. This fitting program uses a grid-search method and search for the vertex where the $goodness_{low}$ is maximum. Here the definition of the $goodness_{low}$ is the same as that of point-fit (Eqn.6.3). We also use the number called N_{50}, which is the maximum number of hit PMTs within 50ns window and when we count the number of hit PMTs, we correct for the TOF (Time of Flight). For the low energy region, this number is proportional to the energy of electron and N_{50} of 5 corresponds to about 1MeV.

Low energy events with many hit PMTs caused by noise are rejected by requiring the number of hit PMTs of the inner detector to be more than 500 and N_{50} be more than 50. Events generated by noise which cannot be reconstructed are rejected by requiring the number of hit PMTs of the inner detector to be more than 500 and the $goodness_{low}$ be more than 0.5.

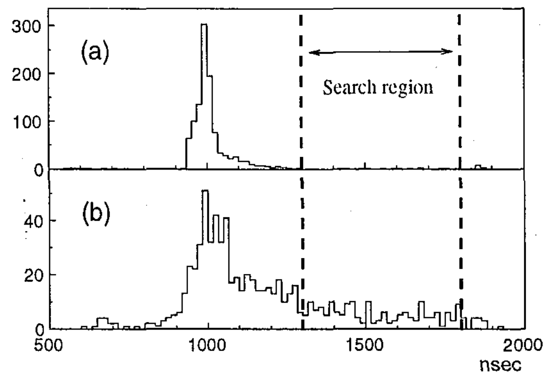

Figure 5.4: Typical timing distribution for (a):normal event and (b):flashing PMT.

Rejection of flashing PMT events

There are some flashing PMTs in the detector. These PMTs emit photons by sparking and generate false events. The events caused by such a flashing PMT usually shows a broad timing distribution. [Figure 5.4].

To remove these events, we use the number of hit PMTs within 100ns window, slide this window from 1200ns to 1800ns and search for the minimized point ($N_{100}(min)$). The events which satisfy one of the following conditions are rejected:

- $N_{100}(min)$ is more than 14,
- the number of hit PMTs of the inner detector is less than 800 and $N_{100}(min)$ is more than 9.

Rejection of accidentally overlapping events

There are some events where a low energy event overlaps with a muon event of later timing. Such events are rejected by requiring the number of hit PMTs in the anti detector in the timing window between 1300ns and 1800ns be less than 19 hits and the total number of p.e. of the inner detector in the same timing window be less than 5000 p.e..

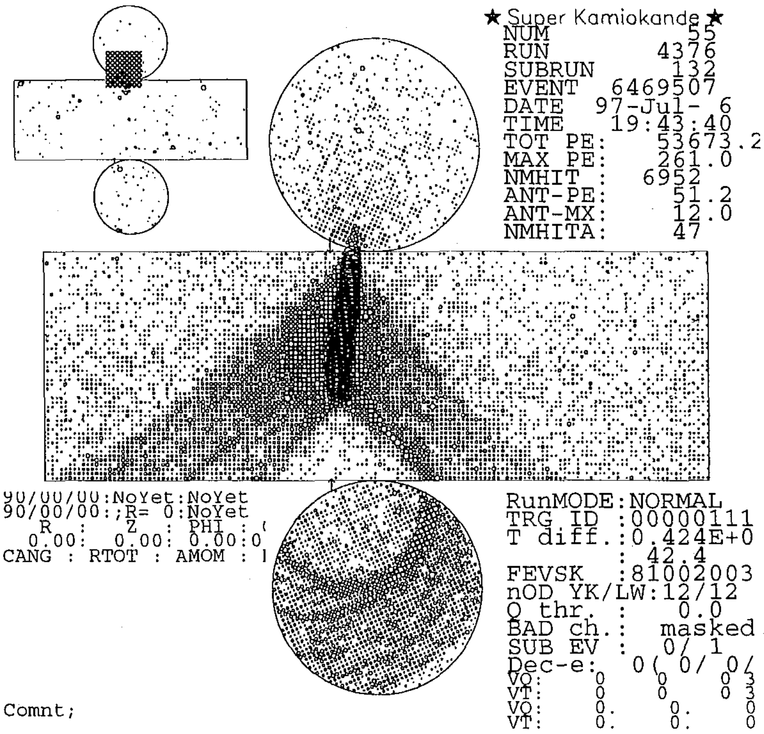

Figure 5.5: Typical cable-hole cosmic-ray muon. The shaded square in the anti detector corresponds to the hit of scintillator veto counter.

Rejection of Cable-hole muon events

In the top part of the anti detector, there are four cable holes where all the signal and high voltage supply cables go through and thus PMTs cannot be installed for the anti detector. To reduce this inefficiency, we have installed 2.0m×2.5m scintillation veto counters on each cable hole. If an event has hit in one of the veto counters and the entering point fitted by the stopping muon fitter is located within 4m from the cable hole, we reject this event. An event display of a typical cable-hole muon is shown in Figure 5.5.

5.3 Visual scanning

After the third reduction, the remaining event rate is about 30 events/day. But this dataset still contains cosmic-ray muon and noise events including events caused by a flashing PMT. In order to remove those events, all the remaining events are visually scanned by two physicists independently. At the same time, each scanner checks the quality of data and if there are some troubles found in the detector, such as too many noise or flasher events, rejects that part of the run. After the two independent scannings, we check the consistency of them and finalize the dataset.

Chapter 6

Event analysis tools

To the remaining events after the third reduction and the visual scanning, we apply several analysis programs. Firstly, the events are fitted to obtain the vertex position and the direction of the particles. The number of rings are counted. Then, we identify particle types of rings and reconstruct the momenta. Finally, for one-ring events, we apply another vertex fitter to improve the vertex resolution. These tools for the analysis are described in this chapter.

6.1 Reconstruction of initial vertex

The fit to obtain the initial vertex is divided into three parts:

- the "point-fit" part, which performs a rough vertex fitting by using only the timing information of hit PMTs,
- the "ring edge search" part, which searches for the edge of the Cherenkov ring,
- the fine vertex fitting part, which uses the ring edge information and takes into account the track length of the particle and scattered photons.

These three parts are described in this section.

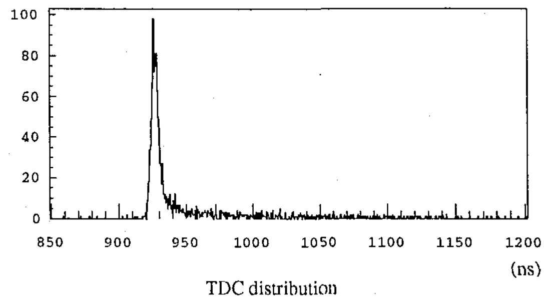

Figure 6.1: TOF subtracted timing(T_0') distribution.

Point-fitter

If we assume that all the Cherenkov photons are emitted from one point in the detector (x, y, z) at one time and that they are not scattered by the medium, then T_i, the timing information observed by the i-th PMT located at (x_i, y_i, z_i), can be written as follows:

$$T_i = \frac{n}{c} \times \sqrt{(x - x_i)^2 + (y - y_i)^2 + (z - z_i)^2} + (constant), \tag{6.1}$$

where c is the light velocity and n is the refractive index of water. The vertex fitter with timing information uses this relation to fit the vertex. If there is enough number of hit PMTs, we can find the correct vertex by changing x, y and z to minimize the width of the distribution of $T_0'(i)$ defined by the following equation:

$$T_0'(i) = T_i - \frac{n}{c} \times \sqrt{(x - x_i)^2 + (y - y_i)^2 + (z - z_i)^2}. \tag{6.2}$$

In the actual case, the Cherenkov photons are scattered by the medium (water) and each PMT has some timing fluctuation; the distribution of $T_0'(i)$ is smeared but still narrow enough to fit the vertex [Figure 6.1].

In fitting the vertex, we define *goodness* to evaluate the correctness of the fitted vertex. *goodness* for this point fit (G_p) is defined as

$$G_p = \frac{1}{N_{hit}} \sum_i \exp(-\frac{(t_i - \langle t \rangle)^2}{2\sigma_p^2}), \tag{6.3}$$

where N_{hit} is the number of hit PMTs, $\langle t \rangle$ is the mean value of t_i and σ_p(=3.75ns) is the typical timing resolution for this fitting. This σ_p includes the effect of scattering thus the value is larger than the actual timing resolution of PMT itself. The "point fit" program searches for a point where the G_p takes the maximum value and regards it as the vertex position.

Ring edge search

The opening angle of a Cherenkov ring is restricted by the refractive index of medium and the maximum half opening angle is 42 degrees for water for a $\beta = 1$ track. Thus, the edge of the Cherenkov ring is useful in fitting the vertex. In searching for the ring edge, we made a charge histogram as a function of the opening angle (PE(θ)) measured from the fitted vertex obtained by the point fitter. The resolution of the vertex fitting is taken into account in making the histogram. By using this histogram, the opening angle of the ring edge (θ_{edge}) is defined as the minimum angle (θ) which satisfy the following two conditions:

$$\frac{d^2\mathrm{PE}}{d\theta^2} = 0, \tag{6.4}$$

$$\theta_{edge} > \theta_{peak}, \tag{6.5}$$

where PE(θ_{peak})>PE(θ) for all θ. At this stage, the direction of the particle is also a free parameter and fitted by maximizing the function (Q) defined as

$$Q(\theta_{edge}) = \frac{\int_0^{\theta_{edge}} \mathrm{PE}(\theta)d\theta}{\sin\theta_{edge}} \times \exp\left(-\frac{(\theta_{edge}-\theta_C)^2}{2\sigma^2}\right), \tag{6.6}$$

where θ_C is the Cherenkov opening angle and σ is its resolution.

TDC-fitter

At this stage, we can use the edge information of the Cherenkov ring and fit the vertex more precisely. We use two goodness parameters for the "TDC-fitter", G_I and G_O. G_I is the goodness for the PMTs located in the Cherenkov ring, which is obtained by the ring edge search program, and the PMTs of which timing (T_i) is earlier than the mean of T_i ($\langle t\rangle$). G_O is the goodness for the remaining PMTs, which are considered to detect the scattered photons. They are defined is as follows:

$$G_I = \sum_i \frac{1}{\sigma_i^2}\exp\left(-\frac{(t_i-\langle t\rangle)^2}{2(1.5\langle\sigma\rangle)^2}\right), \tag{6.7}$$

$$G_O = \sum_i \frac{1}{\sigma_i^2} \times \max\left[\exp\left(-\frac{(t_i-\langle t\rangle)^2}{2(1.5\langle\sigma\rangle)^2}\right),\ 0.8\times\exp\left(-\frac{(t_i-\langle t\rangle)}{20(nsec)}\right)\right], \tag{6.8}$$

where σ_i is the timing resolution of the i-th PMT as a function of charge, $\langle\sigma\rangle$ is the mean value of σ_i. The factor 1.5 is the parameter for the effective cut-off of timing distribution at $\sim 3\sigma$. The overall goodness(G_T) is defined as

$$G_T = (G_I + G_O)/\sum_i \frac{1}{\sigma_i^2}. \tag{6.9}$$

In this fitting, the finite track-length of the particle is also taken into account. The track-length is estimated from the total number of p.e. within the cone of 70° half opening angle and we correct for the timing information of each individual PMT (T_i') in calculating the G_T. The fitted vertex position is the point where the G_T is maximum obtained by iterating the scheme described above.

6.2 Ring counting

The number of rings of an event corresponds to the number of charged particles or γ-rays and is very important information for the proton decay analysis. The ring counting program identifies rings and counts the number of them. In searching for rings, it makes a special "charge map" and searches for possible candidates of rings. After that, the ring information is passed to the ring determination routine and identified as rings. The method of each part is described in this section.

Search for secondary ring candidates

Candidates for secondary rings are searched for by using a "charge map". This "charge map" is a 2-dimensional map which consists of 72 bins for azimuthal angle and 36 bins for zenith angle. Each bin corresponds to the direction from the vertex and the number of p.e. within 42 degrees from the direction is filled to each bin. After summing up the number of p.e. for each bin, the expected number of p.e. from the rings which are already identified is subtracted. The direction of a ring candidate is identified as a bin which has the largest number of p.e. When one of the angles between the direction of the newly identified ring and that of the previously identified ones is smaller than 15 degree, this candidate is treated as the same ring and discarded.

Ring determination

The ring determination is done by using the maximum likelihood method. Firstly, we assume the existence of a new ring candidate and calculate the likelihood from the expected number of p.e. Next, we calculate the likelihood from the expected number of p.e. with the rings which are already identified. This likelihood function is calculated with weights from the opening angle and overlapping regions between the rings. Finally, the ring determination is done by comparing these two likelihoods. If the existence of the new ring is more probable, it is identified as a new Cherenkov ring.

Performance

The performance of the ring counting is checked by using Monte Carlo charged current quasi-elastic scattering events in the Sub-GeV region, which means the visible energy is less than 1.33 GeV. The efficiency is defined as follows:

$$\epsilon = \frac{\text{number of events identified as single-ring}}{\text{number of quasi-elastic events}}. \tag{6.10}$$

Figure 6.2 shows the efficiency as a function of momentum.

According to this figure, 95% of the quasi-elastic events are identified as single-ring above 400MeV/c. Relatively low energy electrons of which momenta are less than 400MeV/c are scattered and the efficiency is slightly lower; the efficiency for the e-like events of which energy is less than 400MeV/c is estimated to be 90%. Figure 6.3 shows the efficiency as a function of the distance from the wall. From this figure, no dependence on the vertex positions can be seen.

6.3 Ring separation

For multi-ring events, the Cherenkov rings will be overlapped. Thus, we have to separate each individual ring to identify the kind of the incident particles and their momenta. We estimate the number of p.e. from each ring for each PMT which is located within 70 degree from the particle direction by maximizing the χ^2 defined as follows:

$$\chi^2 = \sum_i \left(\frac{Q_{obs}(i) - Q_{sum,exp}(i)}{(Q_{obs}(i))} \right)^2, \tag{6.11}$$

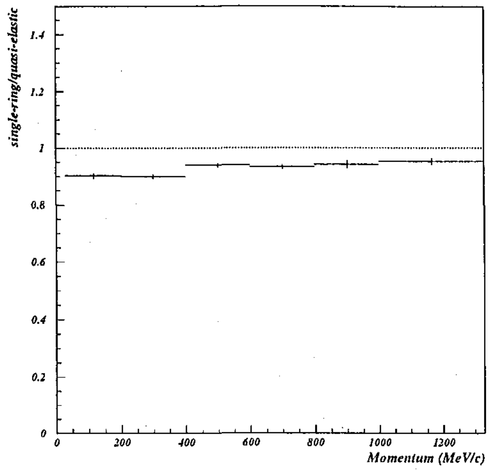

(a)

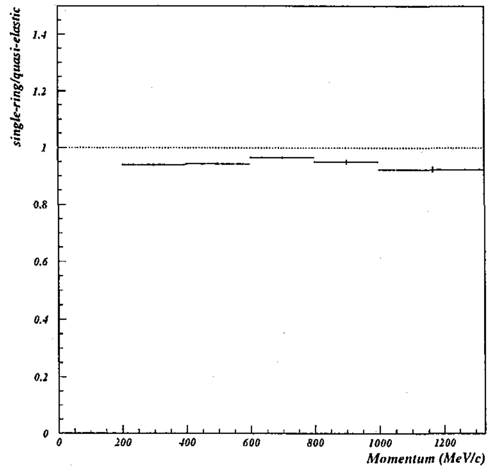

(b)

Figure 6.2: Efficiency of ring counting as a function of momentum for charged current quasi-elastic scattering events. (a): electron neutrino induced and (b):muon neutrino induced events.

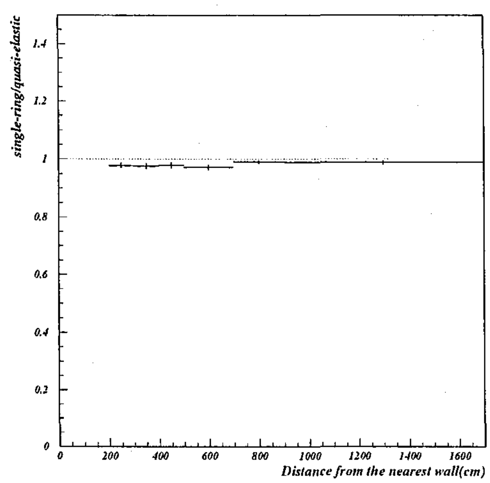

Figure 6.3: Efficiency of ring counting as a function of vertex distance from the wall for muon neutrino charged current quasi-elastic scattering events (momentum of muon is more than 200MeV/c and less than 400MeV/c).

where $Q_{obs}(i)$ is the observed number of p.e. for the i-th PMT, $Q_{sum,exp}(i)$ is the sum of the expected number of p.e. for the i-th PMT. When there are n rings identified, $Q_{sum,exp}(i)$ is defined as:

$$Q_{sum,exp}(i) = \sum_{j=1}^{n} Q_{exp}(i,j). \tag{6.12}$$

At the first stage, we assume that all the particles are electrons and calculate the expected number of photons($Q_{exp}(i,j)$). To maximize the χ^2, we change the momentum of each particle and calculate $Q_{sum,exp}$. Next, the charge distribution of the j-th ring($Q'_{exp}(\theta,j)$) is calculated from the fitted result as a function of angle to the direction of the particle. This time, $Q_{exp}(i,j)$ is obtained by using the maximum likelihood method. The relation between $Q_{exp}(i,j)$ and $Q'_{exp}(\theta,j)$ is defined as $Q_{exp}(i,j) = \alpha_j \cdot Q'_{exp}(\theta_{op}(i,j),j)$, where $\theta_{op}(i,j)$ is the angle between the particle direction which correspond to the j-th ring and the direction to the i-th PMT from the fitted vertex. In the estimation of $Q_{exp}(i,j)$, we use the following likelihood function and maximize its value by changing the parameter α_j:

$$\begin{aligned} L_{sep}(j) &= \sum_i \log(Prob(Q_{obs}(i), Q'_{sum,exp}(i))) \\ &\quad \times\sqrt{Q'_{exp}(\theta_{op}(i,j),j)} \times W_s, \end{aligned} \tag{6.13}$$

$$Q'_{sum,exp}(i) = \sum_{j=1}^{n} \alpha_n Q'_{exp}(\theta_{op}(i,j),j), \tag{6.14}$$

where n is the total number of the rings, $Q'_{exp}(\theta_{op}(i,j),j)$ is the expected number of p.e. from the j-th ring which is calculated from $Q_{exp}(i,j)$ and $Prob(Q_{obs}, Q_{exp})$ is the probability to take Q_{obs} when the incident number of p.e. is Q_{exp}. $Prob(Q_{obs}, Q_{exp})$ is obtained from the measured value of one p.e. distribution for small Q_{exp} which is less than 20 p.e. [Fig.6.4]. For the larger Q_{exp}, $Prob(Q_{obs}, Q_{exp})$ is defined as follows:

$$Prob(Q_{obs}, Q_{exp}) = \frac{1}{\sqrt{(2\pi)}\sigma} \exp\left(-\frac{(Q_{obs}-Q_{exp})^2}{2\sigma^2}\right), \tag{6.15}$$

where $\sigma^2 = Q_{exp} \times 1.2^2 + (0.1 \times Q_{exp})^2$. The factor 1.2 comes from the difference of the PMT resolution between the ideal one and the real one and factor 0.1 comes from the uncertainty in the relative gain calibration of PMT. W_s is the weight parameter to include the effect of the scattered photons defined as follows:

$$W_s = \begin{cases} 1.0 & (\theta_{op}(i,j) \le (\theta_c)) \\ \sqrt{\frac{\theta_c}{\theta_{op}(i,j)}} & (\theta_{op}(i,j) > \theta_c) \end{cases}, \tag{6.16}$$

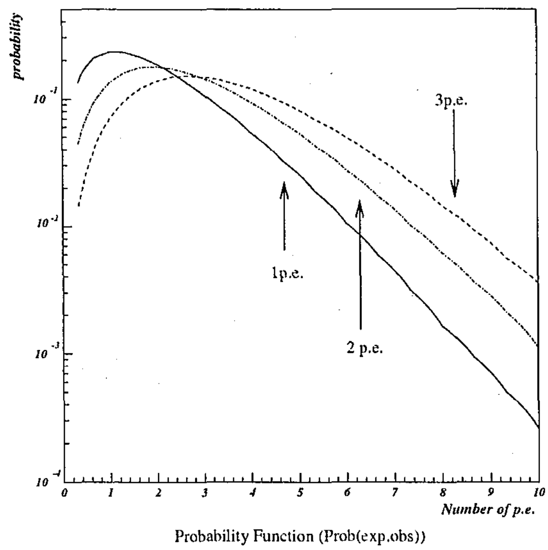

Figure 6.4: Charge probability function $Prob(Q_{obs}, Q_{exp})$.

where θ_c is the Cherenkov angle. After the particle identification, which is described in the following section, we can use the kind of the particle and estimate more precise charge distribution. The likelihood function which is used for the ring separation is the same as above except for the W_s which is always set to 1.

6.4 Particle identification

In the Super-Kamiokande detector, particle identification can be done by using the shape of the Cherenkov ring. Electrons or γ-rays generate electromagnetic showers and their products also emit the Cherenkov light. As a result, observed Cherenkov rings for electrons (γ-rays) are diffused compared to the rings generated by muons. Also the opening angle of the ring can be used to identify the type of low momentum particles.

Expectation from each particle

In identifying particles, we have to estimate the expected number of p.e. for each particle and momentum. For the direct Cherenkov photons from electrons, we made Monte Carlo events of various momenta with ideal quality of water, which means that no light scattering

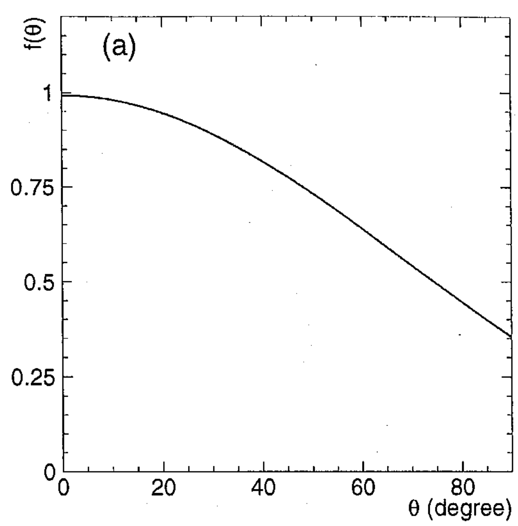

Figure 6.5: Fraction of effective photo-sensitive area of the PMT.

and attenuation are considered. Then, we make the tables of the expected number of p.e. observed at 16.9m from the initial vertex ($N_{MC}(p_e, \theta)$) as a function of momentum (p_e) and opening angle from the particle direction (θ). By using this table, the expected number of p.e. for the i-th PMT is calculated as follows:

$$N_{e,direct,exp}(i) = \alpha_e \times N_{MC}(p_e, \theta_i) \times \left(\frac{16.9(m)}{l_i}\right)^{1.5} \times \exp\left(\frac{l_i}{L}\right) \times f(\Theta), \tag{6.17}$$

where α_e is the normalization factor, p_e is the momentum of an electron which can be calculated from the total number of p.e., l_i is the distance of the i-th PMT from the vertex, parameter 1.5 comes from the characteristic of the scattering of the Cherenkov photons, L is the light attenuation length of water and $f(\Theta)$ is the fraction of effective photo-sensitive area of the PMT [Figure 6.5].

The expected number of p.e. for the i-th PMT from a muon can be expressed as:

$$N_{\mu,direct,exp}(i) = \left(\alpha_\mu \times \left(l_i \left(\sin\theta_i + l_i \left(\frac{d\theta}{dx}\right)\right)\right)^{-1} \times \sin^2\theta_i + N_{\mu,knock,exp}(i)\right) \times \exp\left(-\frac{l_i}{L}\right) \times f(\Theta), \tag{6.18}$$

where α_μ is a normalization factor. The second term includes the ionization energy loss of the particle as shown in Figure 6.6. $N_{\mu,knock,exp}(i)$ is the expected number of photons emitted by the knock-on electrons detected by the i-th PMT as a function of angle between

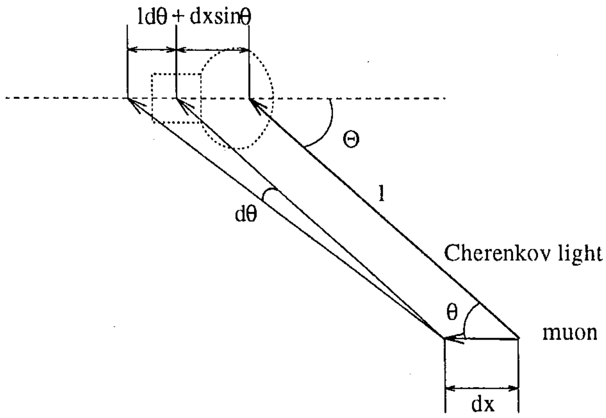

Figure 6.6: Relation between the muon energy loss and the change of the direction of Cherenkov photon.

the particle direction and the i-th PMT. This number is estimated from the Monte Carlo simulation.

The scattered photons are also taken into account. We only use PMTs located inside the cone of which half opening angle is less than $1.5\times\theta_c$, where θ_c is the Cherenkov angle. The direct photons and the scattered photons are identified by using the TOF subtracted relative timing. After selecting the PMTs, we make the histogram of charge as a function of TOF subtracted timing. By using this histogram, the direct photons are defined as follows:

$$-30\text{nsec} < T_i - t_{peak} \leq \sigma(N_i) + 7\text{nsec}, \tag{6.19}$$

where t_{peak} is the TOF subtracted timing when the charge histogram has the highest peak and $\sigma(N_i)$ is the timing resolution of the i-th PMT. From this equation, the number of scattered photons ($N_{scattered}(i)$) is calculated.

Probability functions

To identify particle types, we use two probability functions: one for electron and one for muon, and compare the probabilities. These probability functions consist of two parts: one is the shape of the Cherenkov ring ($Prob_{charge}$) which uses the charge distribution of the ring, and the other is the opening angle of the ring ($Prob_{angle}$) as

$$Prob(e \text{ or } \mu) = P_{charge}(e \text{ or } \mu) \times P_{angle}(e \text{ or } \mu). \tag{6.20}$$

The probability functions for charge are defined as follows:

$$\begin{aligned} Prob_{charge}(e \text{ or } \mu) &= \exp\left(-\frac{1}{2}\left(\frac{\chi^2(e \text{ or } \mu) - min[\chi^2(e), \chi^2(\mu)]}{\sigma_{\chi^2}}\right)^2\right); \quad (6.21) \\ \chi^2(e \text{ or } \mu) &= (\log_{10} e)^{-1} \times (-\log_{10} L(e \text{ or } \mu)) - const., \\ \sigma_{\chi^2} &= \sqrt{2N_D}, \end{aligned}$$

where $L(e \text{ or } \mu)$ is the likelihood function:

$$L(e \text{ or } \mu) = \prod_{\theta_i < 1.5\theta_c} Prob_i(e \text{ or } \mu). \tag{6.22}$$

The probability function for the i-th PMT $Prob_i(e \text{ or } \mu)$ is defined as follows:

for the direct photons,

$$Prob_i(e \text{ or } \mu) = Prob(N_{direct,exp}(i), N_{data}(i)), \tag{6.23}$$

for the scattered photons,

$$Prob_i(e \text{ or } \mu) = Prob(N_{direct,exp}(i), 0) \times Prob(N_{scattered,exp}(i), N_{data}(i)), \tag{6.24}$$

where N_{exp} is the expected number of p.e. and N_{data} is the observed number of p.e.. The probability function $Prob(N_{exp}, N_{data})$ is derived from the measured single-photoelectron distribution for small N_{data}, which is smaller than 20 p.e.. For the larger number of observed number of p.e.(N_{data}) we use the following function:

$$\begin{aligned} Prob(N_{exp}, N_{data}) &= \frac{1}{\sqrt{2\pi}\sigma} \exp\left(-\frac{(N_{exp} - N_{data})^2}{2\sigma^2}\right), \quad (6.25) \\ \sigma^2 &= 1.2^2 \times N_{exp} + (0.1 \times N_{exp})^2. \end{aligned}$$

The factor 1.2 in σ^2 comes from the result of comparison between the actual PMT resolution and the ideal one and the factor 0.1 comes from the uncertainty of the relative calibration of the PMT in this region. The probability to take certain opening angle (θ_{data}) is calculated

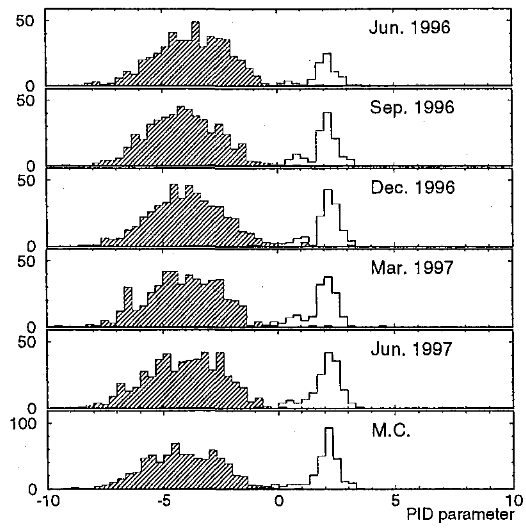

Figure 6.7: Distribution of PID parameter. The hatched region shows the cosmic-ray muons and clear region shows the decay electron.

by using the expected opening angle derived from the reconstructed momentum (θ_{exp}). Thus, the probability function for the opening angle ($P_{angle}(e \text{ or } \mu)$) is defined as

$$P_{angle}(e \text{ or } \mu) = C \times \exp\left(\frac{1}{2}\left(\frac{\theta_{exp}(e \text{ or } \mu) - \theta_{data}}{\Delta\theta}\right)^2\right). \tag{6.26}$$

where C is the normalization constant and $\Delta\theta$ is the ambiguity of the opening angle derived from the reconstructed momentum.

Performance of particle identification

The performance of the particle identification has been studied by using cosmic-ray muon, decay electron and atmospheric neutrino events. In Figure 6.7 shows the result of particle identification for cosmic-ray muons and decay electrons from cosmic-ray muons. X-axis shows the parameter of particle identification(P_{PID}):

$$P_{PID} = C \times (\sqrt{P(e)} - \sqrt{P(\mu)}), \tag{6.27}$$

where C is the normalization constant. If P_{PID} is greater (less) than 0, then that particle is identified as electron-like (muon-like).

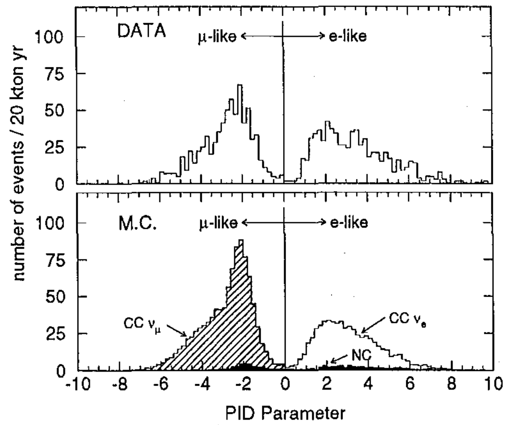

Figure 6.8: Distribution of the PID parameter for single ring atmospheric neutrino data sample and Monte Carlo.

The distribution of Monte Carlo events agrees well with the data and no time dependence is observed. The miss-identification (MISS-ID) probabilities estimated from the data for muon and electron are $0.4 \pm 0.1\%$ and $1.8 \pm 0.5\%$, respectively. From the Monte Carlo events, MISS-ID probabilities are estimated to be $4.4 \pm 1.0\%$ and $0.1 \pm^{0.3}_{0.1}$ % for electron-like and muon-like events, respectively.

To the atmospheric neutrino single-ring events, we also applied the particle identification. The results are shown in Figure 6.8. From this figure, ν_μ events and ν_e events are clearly separated and the shape of the histogram for Monte Carlo events agrees well with the data. From these results, the miss-identification probability is estimated to be $0.8 \pm 0.1\%$.

6.5 MS fit

For single-ring events, the vertex resolution of TDC fit is not so good for longitudinal direction compared to the transverse direction. This is the general characteristic of the fitting which mainly relies on the timing information. To improve the resolution of longitudinal direction, we use charge information in MS fit. To make assumption of charge distribution, we use the results obtained so far: the initial vertex from TDC fit and the information of particle identification.

Fitting method

As described above, the MS fit uses the timing information to fit the vertex perpendicular to the particle direction and the charge distribution to fit the vertex parallel to the direction. Firstly, the vertex position perpendicular to the particle direction is fitted by using the same goodness used for TDC fit. Next, by shifting the vertex parallel to the particle direction, the best position is found where the likelihood function of particle identification (L(e or μ)) returns the best value. The MS-fit iterates these two steps until the following conditions are satisfied:

$$\Delta_{vertex} < 5\text{cm},$$
$$\Delta_{\theta} < 0.5^{\circ},$$

where Δ_{vertex} and Δ_{θ} represent the changes of the vertex and the angle.

Performance

The performance of the MS fit is checked by using the atmospheric neutrino Monte Carlo single-ring events. The distributions of the distance between the real and fitted vertex parallel to the particle direction are shown in Figure 6.9. From this figure, apparently the MS fit has better resolution and smaller systematic effect to the particle direction.

The distribution of the distance between the real vertex and the fitted vertex is shown in Figure 6.10. We define the vertex resolution at the distance where 68% of the events are covered and the results are 34cm for e-like events and 25cm for μ-like events.

The distribution of the angle between the real direction and the fitted direction is shown in Figure 6.11. Again the angular resolution is defined in the same way as for the vertex and the result is 3.2° for e-like events and 1.9° for μ-like events.

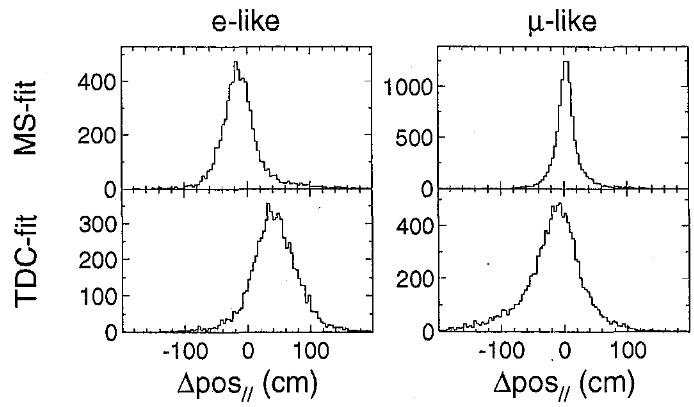

Figure 6.9: Distributions of the distance between the real and fitted vertex parallel to the particle direction of single ring events.

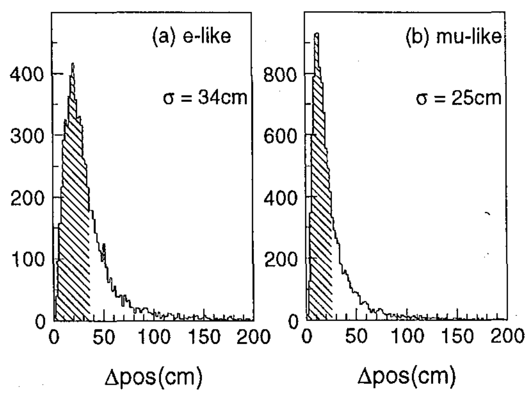

Figure 6.10: Distributions of the distance between the real vertex and the fitted vertex for single ring atmospheric neutrino Monte Carlo events. The hatched region corresponds to the 68% of the events.

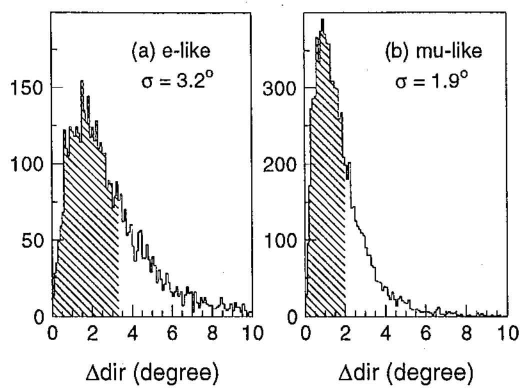

Figure 6.11: Distributions of the angle between the real particle direction and the fitted direction for single ring atmospheric neutrino Monte Carlo events. The hatched region corresponds to the 68% of the events.

6.6 Momentum determination

For the momentum determination, we use the corrected total number of p.e. (R_{tot}). To calculate the R_{tot}, we want to eliminate the effect from the scattered lights. Thus the following selection criteria are set to select the direct photons:

- use PMTs of which opening angle from the particle direction is less than 70°,
- $-50(\mathrm{ns}) < (T'(i) - T'_{mean}) < 250(\mathrm{ns})$,

where $T'(i)$ is the TOF subtracted timing information of the i-th PMT and T'_{mean} is the mean of $T'(i)$. The number of p.e. is also corrected for the flight length of photon (distance from the vertex to the PMT) and for the incoming direction of photons to the PMT. Figure 6.12 shows the relation between the R_{tot} and the momentum for each particle, which were generated from the Monte Carlo simulation.

The absolute scale ambiguity of the momentum reconstruction is discussed in Chapter 7 and it is estimated to be less than ±2.5%. The momentum resolution of each particle is estimated from Figure 6.13 and the results are

$$\text{for electrons} \quad : \quad \sigma_p = 0.6 + \frac{2.6}{\sqrt{p}}\%, \tag{6.28}$$

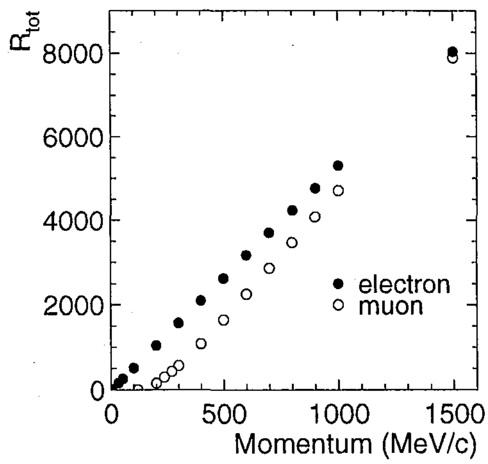

Figure 6.12: Relation between the momentum of the particle and R_{tot}.

$$\text{for } \mu \quad : \quad \sigma_p = 1.7 + \frac{0.7}{\sqrt{p}}\%, \tag{6.29}$$

where p is the momentum of each particle in GeV/c.

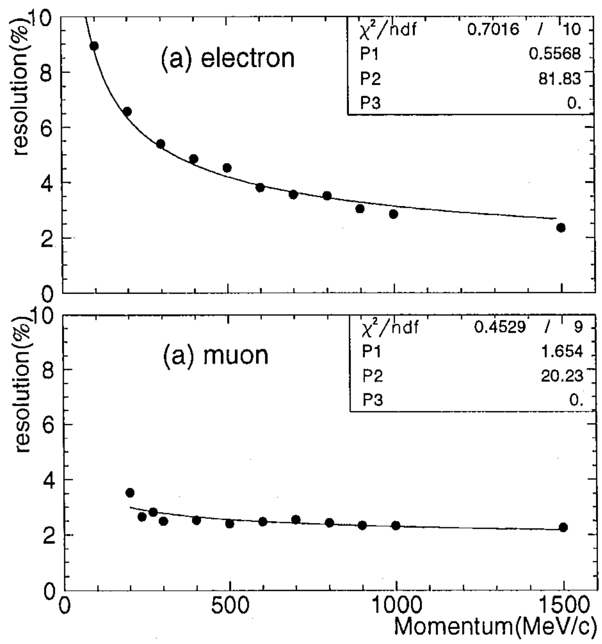

Figure 6.13: Resolution of the reconstructed momentum.

Chapter 7

Energy calibration

The accuracy of the reconstructed momentum and the vertex position is sensitively dependent on the calibration of charge and timing. In this chapter, the methods of calibration and their results are described.

7.1 Relative gain calibration

It is very important to adjust the gain of each PMT, because the momentum is reconstructed out of the charge information. The uniformity of the gain is also important to insure a good detection efficiency for low energy events.

To calibrate the relative gain of the PMTs, a scintillator ball with a Xe lamp as the light source is used. A schematic view of this system is shown in Figure 7.1.

The Xe lamp generates ultra violet light pulses. This light is converted in the scintillator ball to scintillation light, whose wavelength peaks at 440nm by BBOT, a wave length shifter, and is diffused by MgO mixed in the ball. The observed pulse width is a few 10ns. This scintillator ball is lowered into the tank from the calibration hole located near the center of the top surface of the tank. To reduce the systematic effect of the incoming direction of the photon, we took data by placing the scintillator ball at various heights. The relative gain of the i-th PMT(G_i) is expressed by the following equation:

$$G_i = \frac{1}{f(\theta)} \cdot \frac{Q_i}{Q_0} \cdot r^2 \exp\left(\frac{r}{L}\right), \tag{7.1}$$

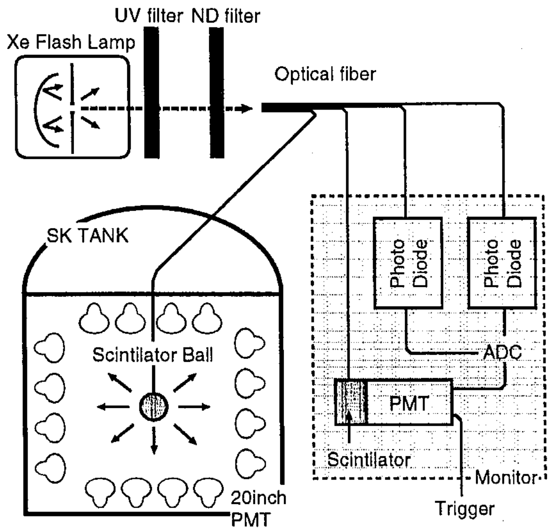

Figure 7.1: A Schematic view of Xe calibration system.

where Q_i is the charge detected by the i-th PMT, r is the distance between the PMT and the scintillator ball, L is the light attenuation length in the water and Q_0 is the normalization factor. We adjusted the gain by changing the high voltage value of each PMT. As a result, the spread of the relative gain is kept within 7% [Figure 7.2].

7.2 Absolute gain calibration

The absolute gain is calibrated by using a low energy γ-ray source. Because each PMT will catch a single photon in such a low energy event, the distribution of the signal pulse height can be treated as that of a single photo electron(p.e.).

We use γ-rays from a neutron capture of Ni. A schematic view of this calibration source is shown in Figure 7.3. A ^{252}Cf source is used as a neutron source and the average energy of emitted neutrons is about 2MeV. The emitted neutrons are thermalized by water and captured by Ni. We use natural Ni whose abundance and energy of emitted γ-rays are listed in table 7.1. The single p.e. distribution for a typical PMT is shown in Figure 7.4. From this figure, the mean value of the charge distribution is obtained as 2.055pC and thus we define 1 p.e. as 2.055pC. Also the relative gain of each PMT is corrected by comparing the mean value obtained from this measurement.

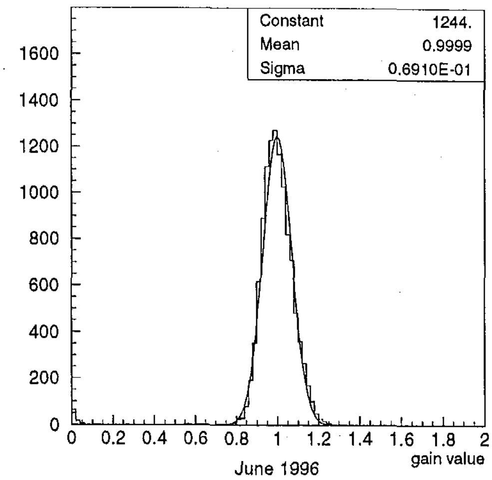

Figure 7.2: Spread of the relative gain of PMT

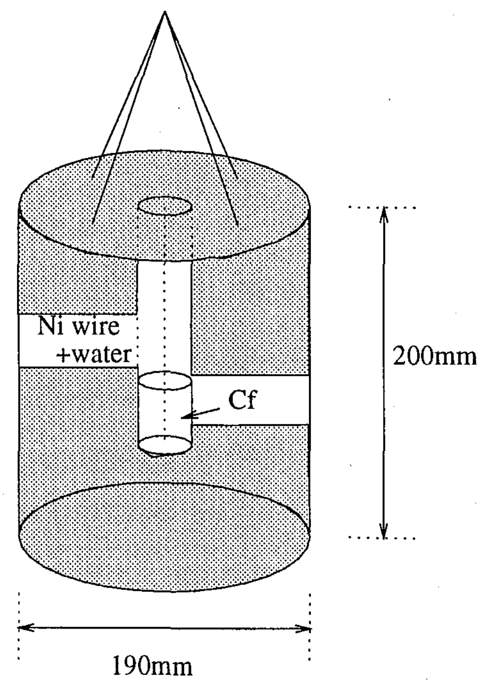

Figure 7.3: A schematic of calibration Ni source

Isotope	abundance (%)	Neutron capture cross section (barn)	Energy of γ (MeV)
^{58}Ni	68.27	5.5	9.0
^{60}Ni	26.10	2.6	7.8
^{61}Ni	1.13	2.0	10.6
^{62}Ni	3.59	15.	6.8
^{64}Ni	0.91	1.5	6.1

Table 7.1: Property of Ni as a gamma-ray source

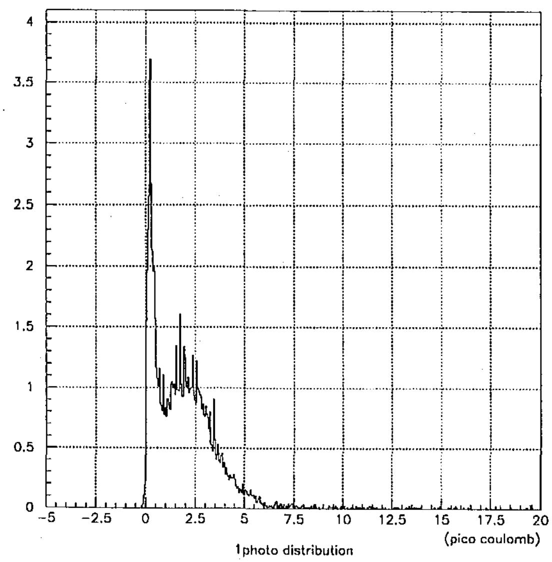

Figure 7.4: Typical distribution of single photo electron.

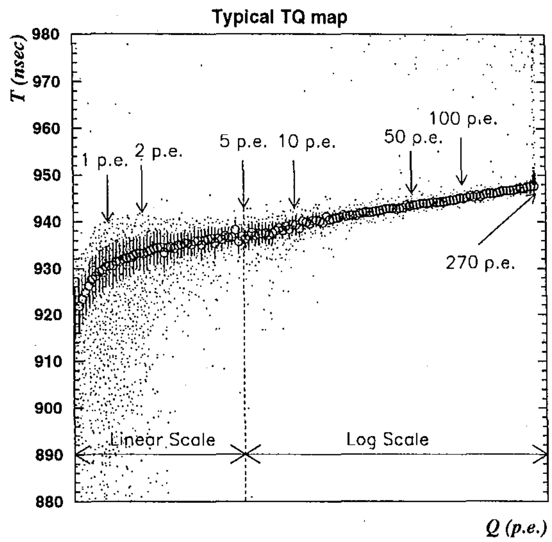

Figure 7.5: Typical timing response of a PMT as a function of the detected charge.

7.3 Calibration of timing

The timing information is essential to the vertex reconstruction and thus the calibration of the relative timing of each PMT is important. As the response of timing is different from PMT to PMT, we have to correct the data for these effects. These differences are mainly from two causes, one is the transit time difference of the PMT and the other is the pulse height dependence of the discriminator response of the input signal (slewnig effect). The difference of the transit time is caused by the different high voltage supplied to each PMT. To correct for these effects, we make a table called TQ-map and adjust timing for different pulse heights, length of cables and response of PMTs. In making TQ-map the pulse width of the light source should be narrow. Therefore, we choose N_2 laser of which pulse width is less than 4ns. The wavelength of N_2 laser itself is 337nm and it is short compared to the wavelength of Cherenkov light. Thus the wavelength is converted to 384nm by a dye. The intensity of the light is controlled by optical filter. The laser light goes through the optical fiber and reaches at a diffusing ball placed at the center of the detector. This diffusing ball emits the light isotropically. Figure 7.5 shows a typical timing response of a PMT as a function of the detected charge. We generate TQ-map for all the channels by fitting this histogram.

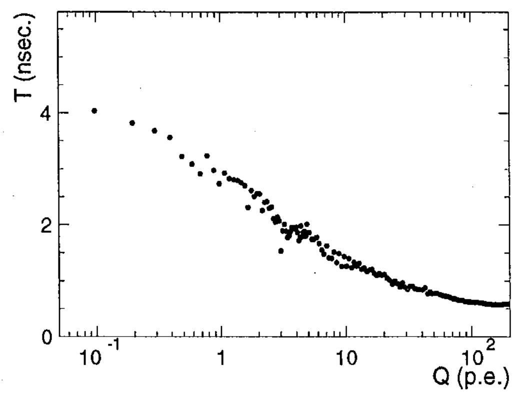

Figure 7.6: Timing resolution as a function of charge.

The timing resolution as a function of charge is also obtained from this figure and the result is shown in Figure 7.6.

7.4 Ambiguity in the energy determination

It is important to know the accuracy of the momentum reconstruction in the data analysis. In this chapter, we estimate the ambiguity in our energy determination by using several sources.

LINAC electrons

We employ an electron LINAC (LINear ACcelerator) installed near the detector. This LINAC can provide electrons with energies between 5MeV and 16MeV with the energy spread of less than 0.3% at the end of the beam pipe. We use the dataset of 16MeV electrons which were injected downward from 6m below the top of the inner PMT surface. The criteria for LINAC electron events are as follows:

- the number of hit PMTs of the inner detector is between 100 and 210,
- $goodness_{low}$ is more than 0.5,
- the distance between the real vertex and the reconstructed vertex is less than 200cm.

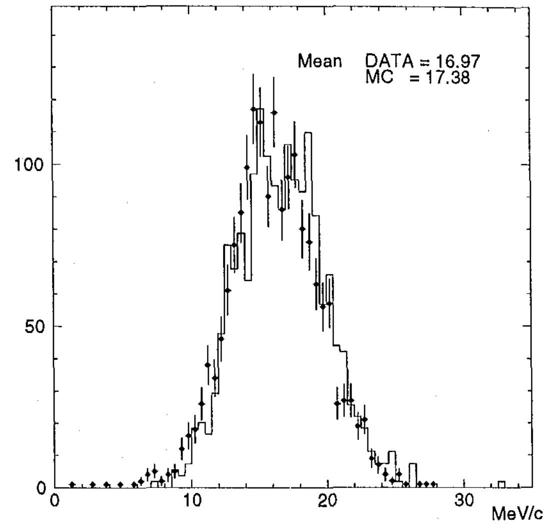

Figure 7.7: Reconstructed momentum distribution of 16MeV electrons from LINAC. Histogram shows that of Monte Carlo.

Figure 7.7 shows the reconstructed momentum distribution of 16MeV electrons from LINAC. The difference of the mean value between the real data and Monte Carlo is 2.4% and thus the agreement is good.

decay electrons

The energy spectrum of decay electrons from muons follows the Michel spectrum. We select decay electron events and compare the spectrum with that of Monte Carlo events. The criteria for decay electron events are as follows:

- the timing gap between the parent muon and the decay electron is more than 1.5μsec and less than 8μsec,
- the number of hit PMTs of the inner detector is less than 1000,
- $goodness_{low}$ is more than 0.5,
- the reconstructed vertex of the decay electron is in the fiducial volume.

For the Monte Carlo events, the vertices distribute uniformly in the fiducial volume and their directions are isotropic. Figure 7.8 shows the reconstructed momentum distribution

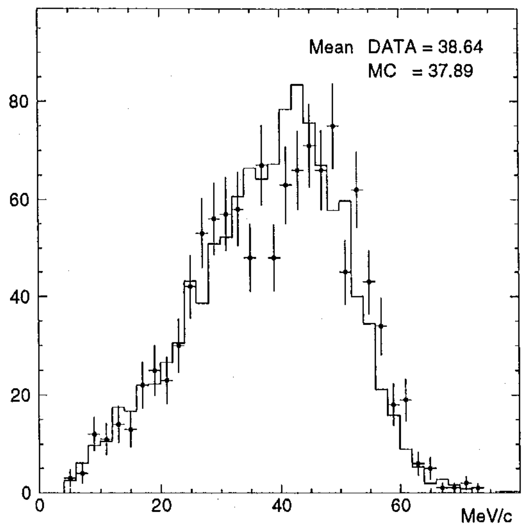

Figure 7.8: Reconstructed momentum of decay electron from cosmic-ray muon. Histogram shows the Monte-Carlo.

of electrons. The spectrum of the data agrees well with that of the Monte Carlo. The difference of the mean values between the real data and Monte Carlo is 2.0%.

reconstructed mass of π^0

π^0s decay into two γ-rays as soon as they are created (or escape from ^{16}O). For the neutral current single π^0 production, no other particles generate Cherenkov rings and the two e-like rings are clearly observed. By using these events, we can reconstruct the mass of π^0 and check the accuracy of the energy reconstruction. The selection criteria for π^0 candidate events are as follows:

- reconstructed vertex is in the fiducial volume,
- two ring events,
- both rings are identified as e-like,
- reconstructed momentum of π^0 (p_{π^0}) is less than 400MeV.

Figure 7.9 shows the distribution of reconstructed mass of π^0. The mean value is the result from Gaussian fit between 110MeV/c^2 and 160MeV/c^2. The discrepancy between the real

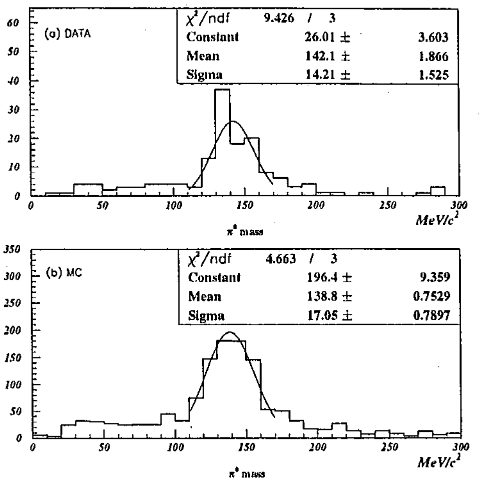

Figure 7.9: Reconstructed mass distribution of π^0. (a):Atmospheric neutrino data sample. (b):Atmospheric neutrino Monte Carlo sample. The solid line shows the result from Gaussian fitting between 110MeV/c^2 and 160MeV/c^2.

data and Monte Carlo is 2.4%.

Low energy stopping muons

For low energy muon events, the opening angle of the Cherenkov cone can also be used to reconstruct momentum. This information is independent of the charge and we can check the ambiguity of the momentum reconstruction by comparing these two methods: one is from charge and the other is from the opening angle of the Cherenkov cone. Figures 7.10-(a) and (b) show the relation between the reconstructed momentum and the opening angle for the Monte Carlo and for the data, respectively.

Figure 7.11 shows the ratio of the reconstructed momentum by using charge information of real data and that of Monte Carlo events which have the same opening angle. From this figure, reconstructed momentum difference between the real data and the Monte Carlo is found to be less than 2.5% at most.

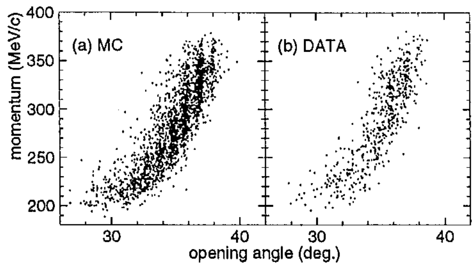

Figure 7.10: Reconstructed opening angle distribution of low energy muons. (a):Atmospheric neutrino Monte Carlo sample. (b):Atmospheric neutrino data sample.

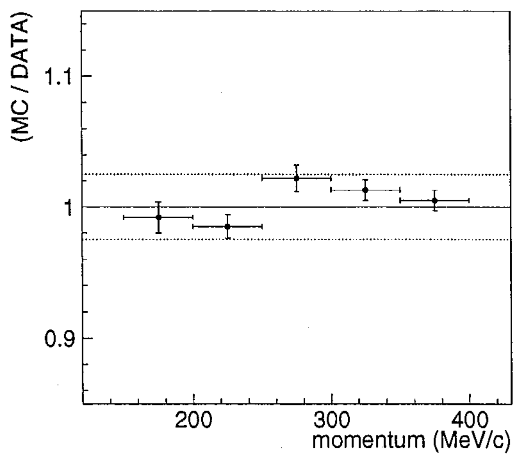

Figure 7.11: Reconstructed momentum ratio of real data and Monte Carlo. X-axis shows the momentum reconstructed from opening angle and Y-axis shows the ratio of reconstructed momentum through charge information between data and Monte Carlo of which momentum reconstructed from opening angle is the same.

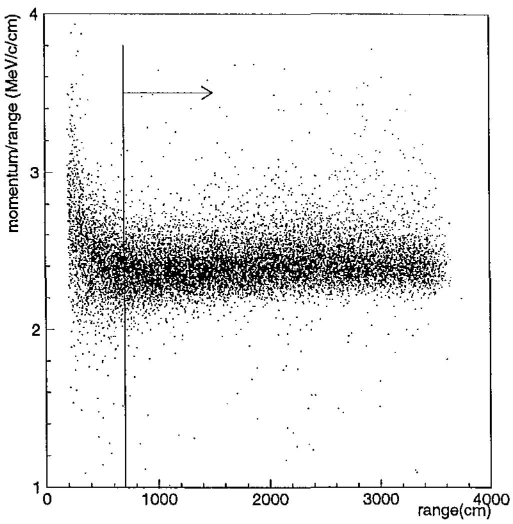

Figure 7.12: Relation between the (range of muon)/(momentum of muon) and the momentum of muon.

High energy stopping muons

For a cosmic-ray muon event of higher energy, we can estimate the momentum by using its track length in the detector, because the track length is proportional to the momentum of the muon. The track length of a muon is estimated by fitting the entrance of the muon as the starting point and the vertex of the decay electron from the muon as the stopping point. Figure 7.12 shows the relation between the momentum and the range of muons.

The mean energy loss is about 2.5MeV/cm. To reduce the ambiguity arising from the estimation of the track length, we use the muons of which track length is more than 7m. The ratio of reconstructed momentum/track length between the Monte Carlo and the real data is shown in Figure 7.13. According to this figure, the difference between the Monte Carlo and the real data is at most 2.1% for momentum of muon less than 1.33GeV/c.

Summary of the momentum calibration

We checked the uncertainty in the absolute scale of the momentum reconstruction by using several sources: LINAC electrons, decay electrons, reconstructed mass of π^0s, low energy stopping muons and high energy stopping muons. Figure 7.14 is the summary of

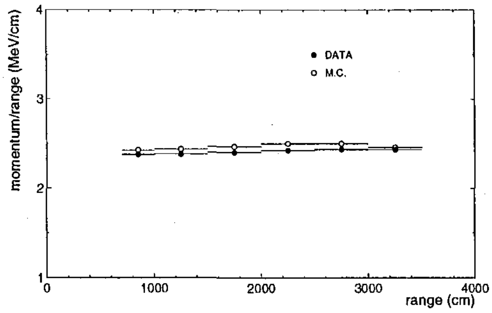

Figure 7.13: Estimated range of muons.

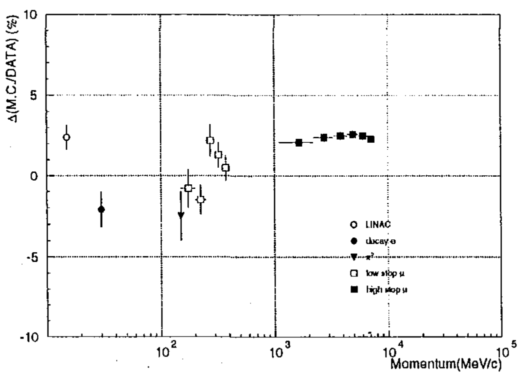

Figure 7.14: The estimated uncertainty in the momentum reconstruction.

uncertainty in our momentum reconstruction. As a result, we estimate the uncertainty in the reconstructed momentum scale to be less than $\pm 2.5\%$ for all momentum regions.

Chapter 8

Characteristics of the event sample

After the visual scanning, there remains 6386 events. Most of the events are generated by atmospheric neutrino events. To these events, the vertex fitting, ring number counting and particle identification programs are applied. (See chapter 6 for the detailed description of each program.) In this chapter, comparisons between the Monte Carlo simulation of neutrino events and the data are shown. For the absolute normalization of the atmospheric neutrino fluxes, we use the calculation done by Honda. In some figures, the fluxes calculated by Gaisser are used for comparison.

Events of neutrino interactions and of proton decay will occur uniformly in the detector. Figure 8.1-(a) and (b) show the vertex distributions of the real data. According to these figures, the vertices are distributed uniformly over the fiducial volume as expected. The excess near the wall is caused by the remaining cable-hole muon events.

Figure 8.2 shows the number of rings for the real data and for the Monte Carlo events. The shapes of these two distributions are quite similar.

Figure 8.3 shows the results of the particle identification for one ring events. Muons and electrons are clearly separated as expected but the number of muons is fewer than the expected from the model. The anomaly of ν_μ/ν_e ratio has been found in Kamiokande and IMB. Data from days of data in Super-Kamiokande confirms this anomaly with higher statistics.

Figure 8.4 (a)-(d) show the vertex distributions of the one ring μ-like and e-like events of data. There is no position dependence observed in all these figures.

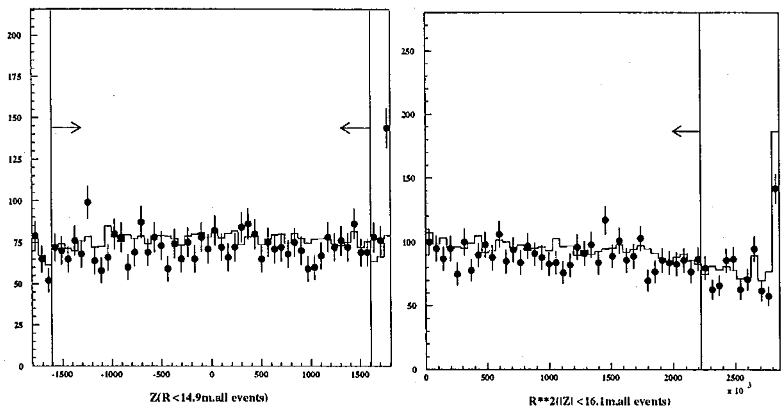

(a) (b)

Figure 8.1: Vertex distribution of the real data. The histogram shows the prediction of atmospheric neutrino Monte Carlo.

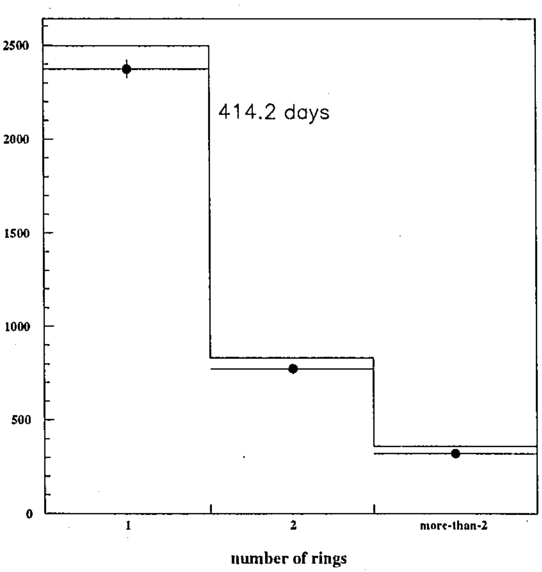

Figure 8.2: Number of rings. Histogram line shows the Monte Carlo prediction.

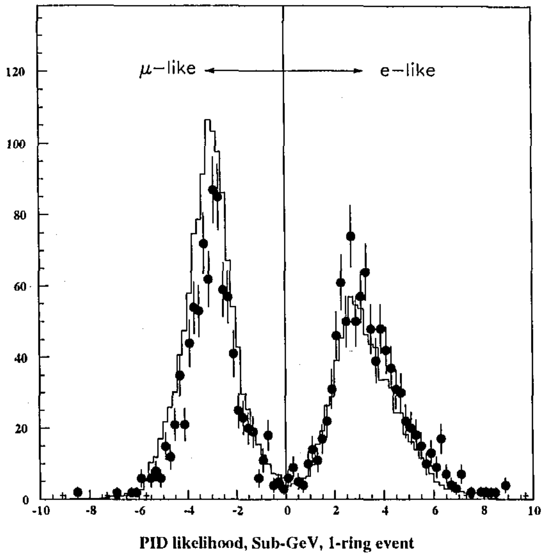

Figure 8.3: Likelihood distribution of particle identification. Histogram line shows the Monte Carlo prediction.

Figure 8.5-(a) and (b) show the reconstructed momentum of electrons and muons for one ring events, respectively. The shape of each distribution shows a good agreement with the Monte Carlo simulation except for the normalization. Based on the study of Monte Carlo simulation, more than 95% of the μ-like events are coming from ν_μ and 90% of the e-like events are from ν_e.

In summary, Monte Carlo simulation reproduces the data well except for the absolute normalization for μ-like events.

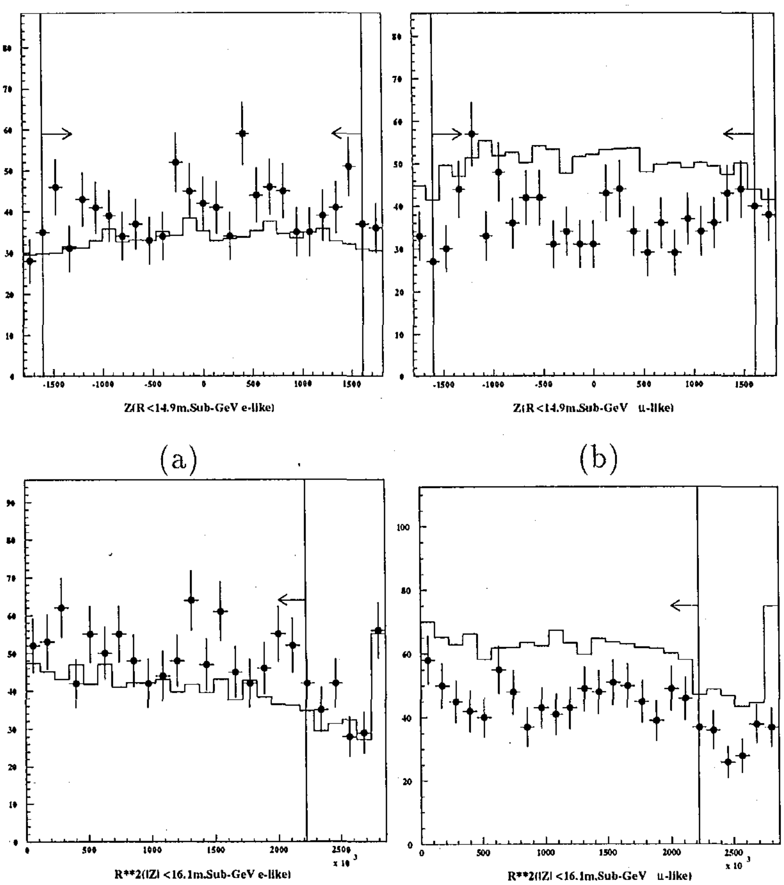

(a) (b)

(c) (d)

Figure 8.4: Vertex distribution of e-like and μ-like events. The histogram shows the prediction of atmospheric neutrino Monte Carlo simulation.

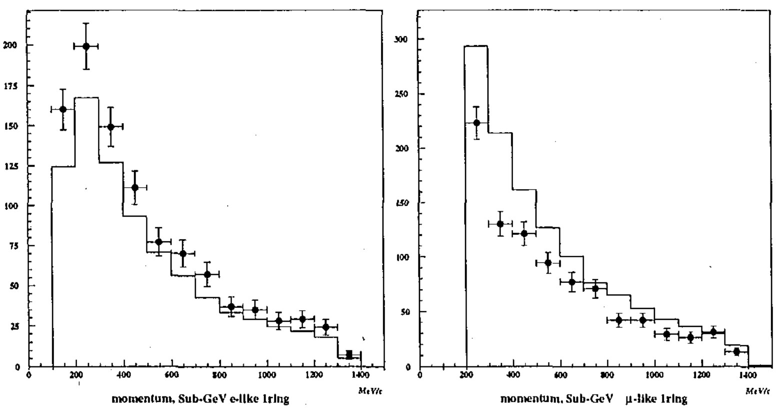

(a) (b)

Figure 8.5: Reconstructed momentum distribution of e-like and μ-like one ring events. The histogram shows the prediction of atmospheric neutrino Monte Carlo simulation.

Chapter 9

Proton decay analysis

The K^+ from $p \rightarrow \bar{\nu}K^+$ carries only 340MeV/c and it is below the threshold momentum for the Cherenkov light emission. Thus the candidate events of this decay mode are identified through the decay products of K^+. The major decay modes of K^+ are

$$\begin{aligned} K^+ &\rightarrow \mu^+\nu_\mu, \\ K^+ &\rightarrow \pi^+\pi^0, \end{aligned}$$

and the branching ratios are 63.5% and 21.2%, respectively. The cross section of the low momentum K^+ is known to be small and more than 90% of them will stop before decay. In the analysis, we can assume that the decay of K^+ to be at rest and therefore that the momentum of each decay particle to be unique. Proton decay into $\bar{\nu}K^+$ can be searched for through these two decay modes using these characteristics. In addition, a prompt γ-ray signal can be used when a proton of ^{16}O in the $p_{3/2}$ state decays. The resulting ^{15}N will emit a prompt γ-ray of 6.3MeV. The signal from the decay particles of K^+ will be delayed due to its relatively long lifetime ($\tau = 12ns$), so there could be more than 15ns time gap between the emitted γ-ray and decay particles of K^+. In Super-Kamiokande, these two signals can be clearly separated within an event. The emission-probability of 6.3MeV γ-ray from Oxygen is estimated to be 40%[63] and the identification of this γ-ray would allow eliminating almost all the background. This prompt γ-ray search is applied to the $K^+ \rightarrow \mu^+\nu_\mu$ candidates. All these modes have been studied in this thesis. They are described in the following sections.

9.1 Search for 236MeV/c μ^+

Since the momentum of μ^+ from the decay of stopped K^+ is 236MeV/c, the selection criteria for candidate events are:

1) one ring μ-like event,

2) with one decay electron.

To determine the signal region and to estimate the detection efficiency, total of 3681 Monte Carlo events have been generated and analyzed just in the same way as the real data. The reconstructed momentum distribution of the proton-decay Monte Carlo events, which satisfy the above criteria, is shown in Figure 9.1-(a). Based on this simulation, signal region of the reconstructed momentum of μ^+ is defined to be between 215MeV/c and 260MeV/c. The detection efficiency of this mode is estimated to be 68.9% through this Monte Carlo study [Table 9.4]. The momentum distributions of the real data and the atmospheric neutrino Monte Carlo events, which satisfy the above criteria, are shown in Figures 9.1-(b) and Figure 9.1-(c), respectively.

To estimate the excess of proton-decay signal from these three histograms, we count the number of events in three momentum regions: from 200MeV/c to 215MeV/c, from 215MeV/c to 260MeV/c and from 265MeV/c to 300MeV/c, and apply χ^2 method to fit parameters. The χ^2 function is defined as follows:

$$\chi^2(a,b) = \sum_{i=1}^{3} \frac{(N_{real}(i) - (a \cdot N_{atm\nu}(i) + b \cdot N_{pdcy}(i)))^2}{N_{real}(i)}, \tag{9.1}$$

where a and b are the fit parameters, $N_{real}(i), N_{pdcy}(i), N_{atm\nu}(i)$ are the numbers of events of real data, of proton decay Monte Carlo and of atmospheric neutrino Monte Carlo, in each momentum region(i), respectively [Table 9.1]. From this fitting result, the excess from the proton decay is estimated with the 90% confidence level(C.L.) [Table 9.2]. The best fit parameter is in the unphysical region ($b < 0$). Thus, the unphysical region have to be omitted while estimating the parameter for the excess of the signal with 90% C.L. (b_{90}). To obtain the parameter b_{90}, it is necessary to calculate $\Delta_{\chi^2}(= \chi^2(90\%\mathrm{C.L.}) - \chi^2(\mathrm{minimum}))$. Assuming the distribution of χ^2 as Gaussian, the Δ_{χ^2} is defined as:

$$\frac{f(\Delta_{\chi^2})}{f(\infty)} = 0.9, \tag{9.2}$$

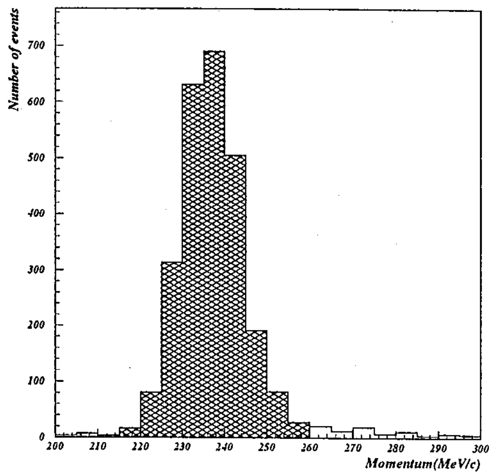

(a)

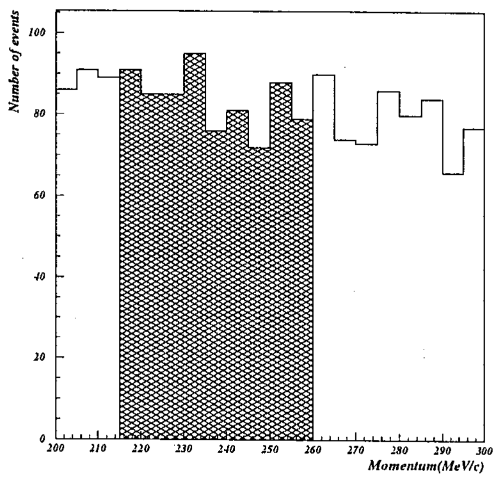

(b)

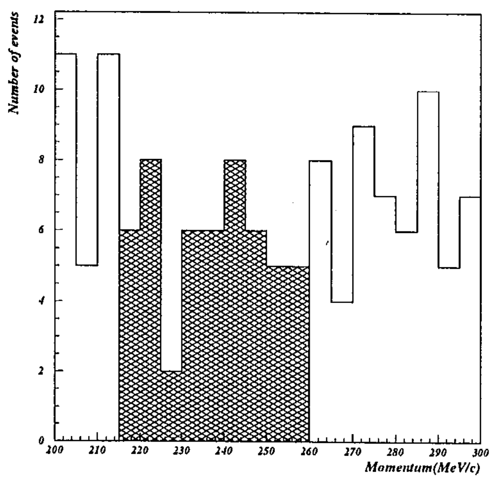

(c)

Figure 9.1: Reconstructed momentum distribution of (a) 236MeV/c μ^+ from K^+ decay, (b) Monte Carlo 1 ring μ-like events of 225kt·yr equivalent atmospheric neutrinos and (c) 1 ring μ-like events in the 25.5kt·yr of Super-Kaminokande data. Defined signal region is hatched.

	$p \to \bar{\nu} K^+$ $K^+ \to \mu^+ \nu_\mu$ N_{pdcy}	Atmospheric ν M.C. (225kt·yr) $N_{atm\nu}$	Super-Kamiokande data (25.5kt·yr) N_{real}
200 $\sim$ 215 MeV/c	14	266	27
215 $\sim$ 260 MeV/c	2537	752	52
260 $\sim$ 300 MeV/c	86	630	56

Table 9.1: Number of events in each momentum region.

	a (# of estimated B.G. events)	b (# of estimated excess)	χ^2
Best fit	9.36×10^{-2} (70.4)	-7.28×10^{-3} (-18.5)	0.29
90% C.L.	7.88×10^{-2} 59.2	4.15×10^{-3} 10.9	6.95

Table 9.2: Fitted parameters of 236MeV/c μ search.

$$f(x) = \int_0^x \exp(-\frac{1}{2}(x - x_0)^2), \quad (9.3)$$

where x_0 is the minimum value of the χ^2. Then, the parameter b_{90} is calculated to take the maximum value by changing the value a for the fixed Δ_{χ^2}.

The number of events of excess signal is estimated to be 11 and the momentum distribution of fitted parameters with the 90% C.L. is shown in Figure 9.2. The partial lifetime (τ_β yr) can be calculated as follows:

$$\tau_\beta = (7.525 \times 10^{33} \times T \times \epsilon B_m)/N_{cand}, \quad (9.4)$$

where T is the exposure time in year, ϵB_m is the detection efficiency multiplied by the meson branching ratio and N_{cand} is the number of candidate events. Therefore, the lower limit of the partial lifetime of 3.4×10^{32} years with 90% C.L. But the systematic error reduces this number as described in section 9.4.

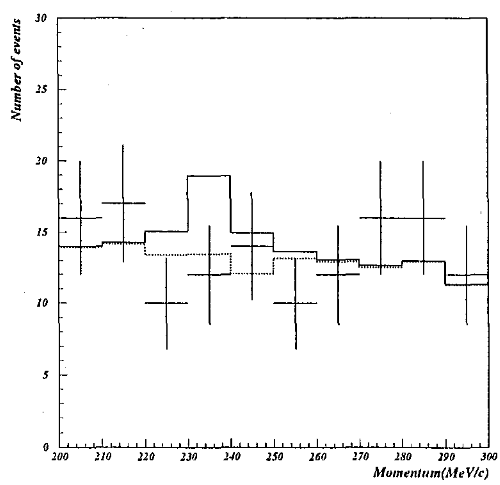

Figure 9.2: Reconstructed momentum distribution. Solid line shows the estimated 90% C.L. number of events which contains the background atmospheric neutrino and the proton decay signal, dotted line shows the estimated 90% C.L. number of events which contains only the background atmospheric neutrino and the data-points with error-bars are the data with statistical errors.

9.2 $K^+ \to \pi^+\pi^0$ mode search

Each π from stopped K^+-decay carries only 205MeV/c and the Cherenkov ring generated by π^+ is almost invisible in Super-Kamiokande. Therefore, event selection of this mode is done by searching both for π^0 of which momentum is 205MeV/c and for the decay electron from π^+,

$$\pi^+ \rightarrow \mu^+\nu_\mu, \quad (9.5)$$

$$\mu^+ \rightarrow e^+\bar{\nu}_\mu\nu_e. \quad (9.6)$$

π^0 can be identified as two γ-rays of which reconstructed mass is around 135MeV/c^2. The selection criteria for the mass and the momentum of π^0 were determined based on the Monte Carlo study on this decay mode ($p \to \bar{\nu}K^+, K^+ \to \pi^+\pi^0$). At first, events which have two electron-like (e-like) rings and one decay electron were selected. The reconstructed mass distribution of the events satisfying the above criteria is shown in Figure 9.3-(a). Based on this, the signal region of the reconstructed mass is determined to be between 85MeV/c^2 and 185MeV/c^2. Figure 9.3-(b) shows the reconstructed momentum distribution of π^0. From this result, we set the signal region of momentum to be from 175MeV/c to 250MeV/c. The detection efficiency for this mode is estimated to be 37%. Figures 9.4-(a) and (b) show the background distributions of the reconstructed mass and the momentum of π^0s generated by atmospheric neutrino Monte Carlo events, respectively. Among the remaining atmospheric neutrino Monte Carlo events, 9 out of 43 are induced by ν_μ or $\bar{\nu}_\mu$. From the observation of atmospheric neutrino in Super-Kamiokande[64], measured fluxes of ν_μ and $\bar{\nu}_\mu$ are known to be smaller than the theoretical expectation while ν_e and $\bar{\nu}_e$ are slightly larger than expected. The actual values are obtained as:

$$\mathrm{flux}_{measured}(\nu_\mu + \bar{\nu}_\mu) \simeq 0.74 \times \mathrm{flux}_{expected}(\nu_\mu + \bar{\nu}_\mu), \quad (9.7)$$

$$\mathrm{flux}_{measured}(\nu_e + \bar{\nu}_e) \simeq 1.2 \times \mathrm{flux}_{expected}(\nu_e + \bar{\nu}_e). \quad (9.8)$$

By using these values, the number of background is estimated to be 3.6 events/yr in Super-Kamiokande. Figure 9.5 shows the same distribution for the real data. There remains no candidate event. The numbers of events remaining after each reduction step are summarized in Table 9.3. 90% C.L. upper limit for the number of proton decay candidates(x_{limit})

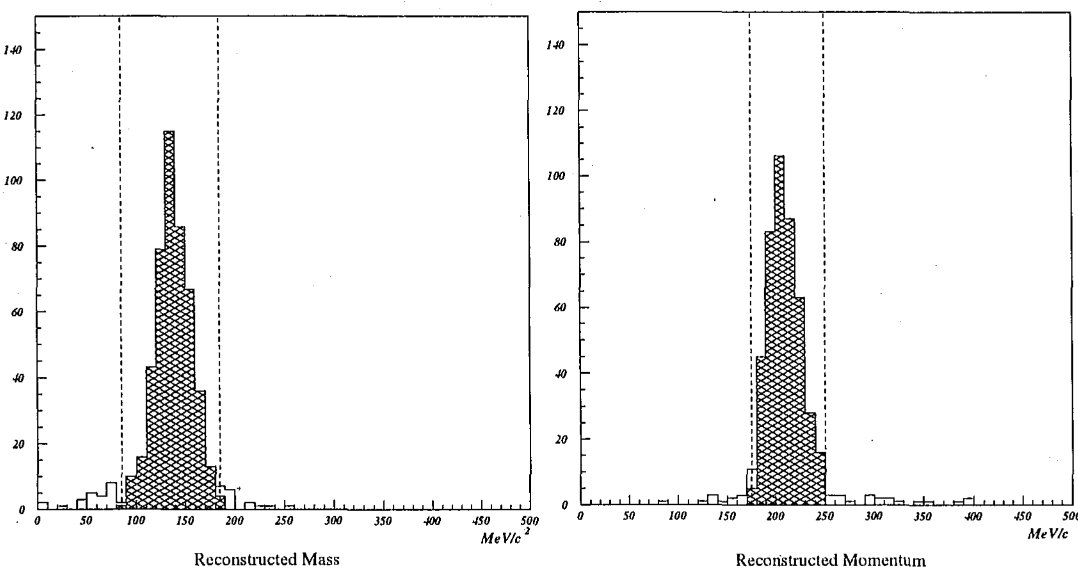

(a) (b)

Figure 9.3: (a) Distribution of the reconstructed mass of π^0 from $K^+ \to \pi^+\pi^0$ Monte Carlo events. (b) Distribution of the reconstructed momentum of π^0 from $K^+ \to \pi^+\pi^0$. In each figure, hatched area corresponds to the defined signal region.

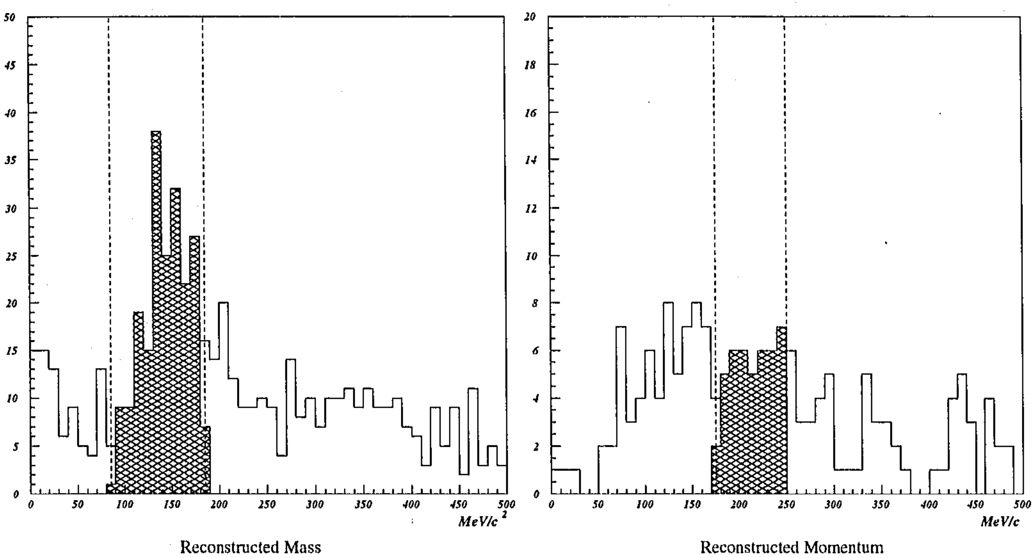

(a) (b)

Figure 9.4: (a) Distribution of the reconstructed mass of two showering particles of 225kt·yr equivalent atmospheric neutrino Monte Carlo events. (b) Reconstructed momentum distribution of π^0 candidates. In each figure, hatched area corresponds to the defined signal region.

	$p \to \bar{\nu} K^+$ $K^+ \to \pi^+ \pi^0$ Monte Carlo	Atmospheric neutrino M.C. (Normalized)	Super-Kamiokande data (25.5kt·yr)
Generated	1171	—	—
Fid.Vol. and 2 Rings	790	755	780
Both e-like	749	450	462
With 1 decay-e	508	93.5	81
Mass of π^0 ($85\mathrm{MeV/c}^2 \sim 185\mathrm{MeV/C}^2$)	470	20.1	19
Momentum of π^0 ($175\mathrm{MeV/c} \sim 250\mathrm{MeV/c}$)	433	4.08	4

Table 9.3: Remaining number of events at each reduction step. The number of events for atmospheric neutrino Monte Carlo are normalized to both measured flux and exposure.

is calculated as follows:

$$
\begin{aligned}
\frac{\int_0^{x_{limit}} P(N_{obs}, N_{bgd}(x))dx}{\int_0^{\infty} P(N_{obs}, N_{bgd}(x))dx} &= 0.90,, & (9.9)\\
N_{bgd}(i,x) &= X_{BG} + x, & (9.10)
\end{aligned}
$$

where $P(N,x)$ is the probability function of the Poisson statistics, N_{obs} is the number of observed candidates, X_{BG} is the number of estimated background events, $\epsilon B_m(i)$ is the detection efficiency multiplied by the meson branching ratio. Using x_{limit} and eqn.9.4, 90% C.L. lower limit of the partial lifetime for this decay mode is obtained to be 1.4×10^{32} years. But the systematic error reduces this number as described in section 9.4.

9.3 236MeV/c μ^+ with prompt 6.3MeV γ-ray search

By requiring the prompt γ-ray from the oxygen in addition to a monochromatic 236MeV/c μ^+ signal, almost all the background events coming from atmospheric neutrino interactions can be eliminated. The timing gap between the prompt γ-ray and the μ^+ is less than a few tens of ns, these two signals are contained in one event. Thus, the candidate events for this analysis are selected by the same criteria for the monochromatic 236MeV/c μ^+-search as described before. After that, we apply the prompt γ-ray search program. This prompt γ-ray search is done by the following sequence:

- making the timing distributions of hit PMTs for one event [Figure 9.6],
- search for the primary peak produced by μ^+ in the timing histogram,
- search for the prompt peak produced by γ-ray in the timing histogram.

Before applying the prompt peak-search, we reject proton induced events. These protons are produced through neutral current interactions. There are one ring events where a ring is induced by proton with large momentum enough to emit Cherenkov photons. γ-rays can be emitted from the excited nucleus, whose effect is also included in the Monte Carlo. Therefore, if the fitted vertex has been shifted from the real vertex, a fake prompt peak will be observed due to the wrong TOF value calculated for each PMT. And there are not so many proton induced events. Thus, in the MS-Fit, which is described in Chapter 6, the particle can be identified as μ and the fitted vertex will be shifted from the real one because proton is much heavier than muon. For the proton rejection, we use the timing information of each PMT and the fitted vertex. The proton induced events are rejected by requiring *goodness* of TDC-fit (G_T, defined in eqn.6.9) to be greater than 0.6 at the vertex fitted by the MS-fit.

The peak-search is done by counting the number of hit PMTs within 12ns window. The timing gap between the prompt γ-ray peak and the μ peak is required to be more than 12ns. Figures 9.7-(a) and (b) show the number of hit PMTs in the timing region of the prompt peak candidates obtained by applying the prompt peak-search program to the Monte Carlo events of $K^+ \rightarrow \nu_\mu \mu^+$ with and without γ-ray, respectively. In Figure 9.7-(b), there are some events with prompt peak without 6.3MeV γ-ray. The prompt peak is caused by γ-rays emitted from the excited nuclei which collided with K^+. Based on these results, the selection criterion of the prompt γ-ray peak is to require more than 7 hit PMTs in the prompt peak. The detection efficiency for the prompt γ-ray search is estimated to be 4.0% including the branching ratio of $K^+ \rightarrow \mu^+ \nu_\mu$ and the emission probability of 6.3MeV γ-ray. Figure 9.8-(a) shows the corresponding figures to Figure 9.7 for the atmospheric neutrino Monte Carlo events after the proton-rejection. From this figure, the background contamination is estimated to be 0.25 events/yr.

Finally we apply the same cuts to the real data, and observe no events surviving as shown in Figure 9.8-(b). The numbers of events in each reduction step are also summarized in table 9.4.

The obtained lower limit of the partial lifetime for this mode is 1.5×10^{32} yr at 90% C.L.(eqn.9.4)

9.4 Systematic errors

Main sources of systematic errors are:

- uncertainty in the momentum reconstruction,
- uncertainty in the detection efficiency of the decay electron from the stopped muon,

	$p \to \bar{\nu} K^+$ $K^+ \to \mu^+ \nu_\mu$ with 6.3MeV γ	$p \to \bar{\nu} K^+$ $K^+ \to \mu^+ \nu_\mu$ without 6.3MeV γ	Atmospheric ν M.C. (Normalized)	Super-Kamiokande data (25.5kt·yr)
Generated	1173	2508	—	—
Fid.Vol. and 1 Ring	1061	2312	2387	2594
μ-like	1034	2240	1134	1152
With 1 decay-e	871	1856	691	680
Momentum of μ (215$\sim$260MeV/c)	804	1733	63	52
Proton rejection	782	1727	62	52
prompt γ search	233	13	2.5×10^{-1}	0

Table 9.4: Remaining number of events at each reduction step. The number of events for atmospheric neutrino Monte Carlo are normalized to both measured flux and exposure.

- uncertainty in the neutrino fluxes and interaction cross sections used in the Monte Carlo simulation.

As discussed in Chapter 7, the uncertainty of the momentum reconstruction is estimated by using various sources. For the search of monochromatic 236MeV/c μ^+ peak, the systematic error of the momentum reconstruction is less than 2.5%. This value is estimated by comparing two independent methods in reconstructing the momentum. When the reconstructed momentum is shifted by $\pm 2.5\%$, the maximum expected number of excess events (90% C.L.) becomes 13 instead of 11 and the detection efficiency changes only by 1.0%. In searching for monochromatic 236MeV/c μ^+ peak, we have also calculated the expected number of excess events by using the other size of binning to estimate the effect of binning. We used 5MeV/c for each bin and fitted both with the χ^2 method and with the maximum likelihood method with Poisson distribution function. At the same time, the reconstructed momentum is also shifted by $\pm 2.5\%$. Combining all these effects, the estimated number of signal events is obtained to be less than 13 at 90% C.L.

For the search of $K^+ \to \pi^0\pi^+$ mode, the number of events in the signal region is unchanged even if the allowed region of both mass and momentum are widened by 2.5% and the detection efficiency of pion changes only by 2.3% based on the proton decay Monte Carlo simulation. Thus, the effect of systematic error of the momentum reconstruction is negligible in this mode.

The systematic error for the detection efficiency of the decay electron from a muon is estimated to be less than 2%[65]. This value was estimated by comparing the fraction of cosmic-ray muon events associated with decay electron between the Monte Carlo simulation and the real data. This uncertainty will directly reflect into the detection efficiency although the value is small and thus the lower limit of the partial lifetime for each mode is unchanged.

The ambiguity of the number of background events comes from the uncertainty of the neutrino flux and the interaction cross sections. This ambiguity can be estimated by comparing the number of events of the atmospheric neutrino background and the real data at each reduction step. The maximum difference between the number of events of the Monte Carlo and the real data in the reduction step is less than 10%. For the $K^+ \to \pi^0\pi^+$ search, we take this effect into account by reducing the number of estimated background events by 10%. And the lower limit of partial lifetime for this mode becomes 1.3×10^{32} years with 90% C.L. However, for search of the 236MeV/c μ^+ with prompt γ-ray, the lower limit of the partial lifetime does not change because there is no candidate event remaining. In searching for the excess of 236MeV/c μ^+, we only use the shape of the momentum distribution and the absolute normalization is left as free parameter in the fitting. Thus the ambiguities of neutrino flux and the interaction cross-sections will not affect the lower limit of the partial lifetime.

The cross section of the neutrino K production was measured in the accelerator experiment and the number of events expected through this interaction was studied[66]. The expected number of events is 0.1 event/kt·yr. From this number, we can calculate the number of events remaining after the rejection by using the detection efficiency estimated from the proton decay Monte Carlo. The expected background from neutrino K production for each mode are as follows:

1.15		event/25.5kt·yr	for $K^+ \rightarrow \mu^+\nu_\mu$,
1.28	$\times10^{-1}$	event/25.5kt·yr	for $K^+ \rightarrow \pi^0\pi^+$,
1.15	$\times10^{-1}$	event/25.5kt·yr	for $K^+ \rightarrow \mu^+\nu_\mu$ with prompt γ-ray tag.

But the inclusion of this interaction only increases the lower limit and thus, to be conservative, it is not included in the lifetime estimation.

9.5 The result

The lower limits of the partial lifetime for $p \rightarrow \bar{\nu}K^+$ are summarized in Table 9.5.

The combined 90% C.L. upper limit for the number of proton decay candidates (x_{limit}) is calculated by integrating the likelihood function to the 90% probability level as follows:

$$\frac{\int_0^{x_{limit}}[\prod_{i=1}^n P(N_{obs}(i), N_{bgd}(i,x))]dx}{\int_0^{\infty}[\prod_{i=1}^n P(N_{obs}(i), N_{bgd}(i,x))]dx} = 0.90, \tag{9.11}$$

$$N_{bgd}(i,x) = X_{BG}(i) + \frac{\epsilon B_m(i)\cdot T}{\sum_{j=1}^n[\epsilon B_m(i)\cdot T]}x, \tag{9.12}$$

where n is the number of independent observations, $P(N,x)$ is the probability function of the Poisson statistics, $N_{obs}(i)$ is the number of observed candidates, $X_{BG}(i)$ is the number of estimated background events , $\epsilon B_m(i)$ is the detection efficiency multiplied by the meson branching ratio and each suffix i stands for the i-th observed mode. In this thesis two decay modes of K^+ are analyzed: $K^+ \rightarrow \mu^+\nu_\mu$ mode and $K^+ \rightarrow \pi^0\pi^+$ mode. At this moment, the lifetime limit obtained by prompt γ-ray tagging method is shorter than that by the 236MeV/c μ^+ excess-search method. Thus the limit obtained by the prompt γ-ray tagging method is not used in calculating the combined result. But the 236MeV/c μ^+ excess-search method is background limited and the prompt γ-ray tagging method will be important when the detector exposure is increased.

Finally, the lower limit of the partial lifetime for $p \rightarrow \bar{\nu}K^+$ mode is obtained to be

$$\tau/B(p \rightarrow K^+\bar{\nu}) \geq 3.3 \times 10^{32} \text{ yr (90\% C.L.).} \tag{9.13}$$

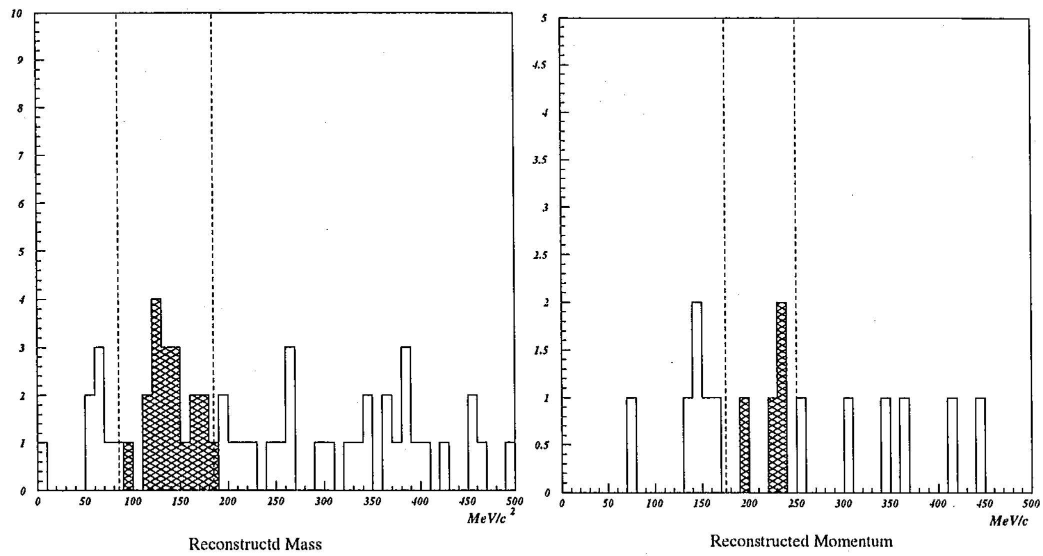

(a) (b)

Figure 9.5: (a) Reconstructed mass distribution of 25.5kt·yr of Super-Kamiokande data. (b) Reconstructed momentum distribution. In each figure, hatched area corresponds to the defined signal region.

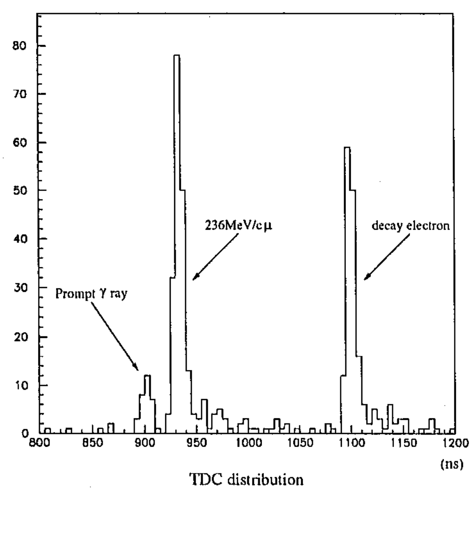

Figure 9.6: Typical TDC distribution (TOF subtracted) for Monte Carlo events of $p \rightarrow \bar{\nu} + K^+$ with 6.3MeV γ-ray. The prompt peak around 900ns corresponds to the 6.3MeV γ-ray and the last peak around 1100ns corresponds to the decay electron from μ.

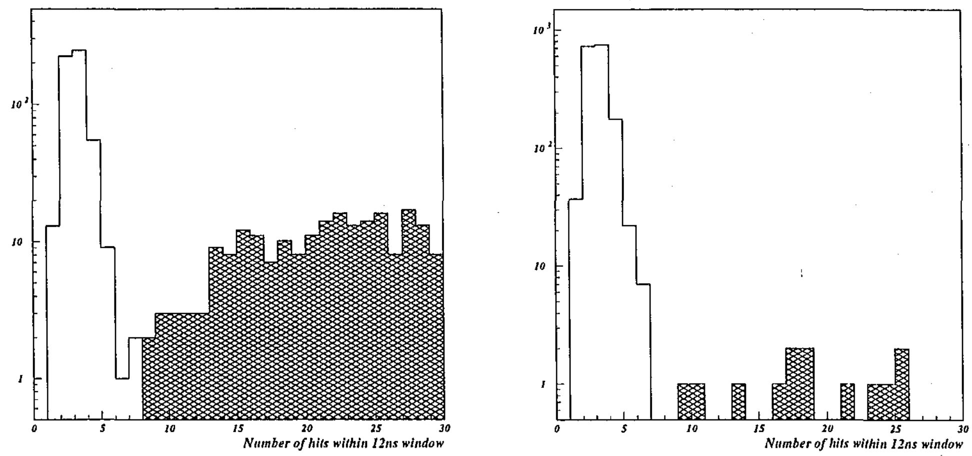

(a) (b)

Figure 9.7: Number of hit PMTs within 12ns for the prompt peak candidate for $p \to \bar{\nu}K^+, K^+ \to \mu^+\nu_\mu$ Monte Carlo (a) with 6.3MeV γ-ray and (b) without 6.3MeV γ-ray. (Both datasets include γ-rays generated by the interactions of K^+ in H_2O.)

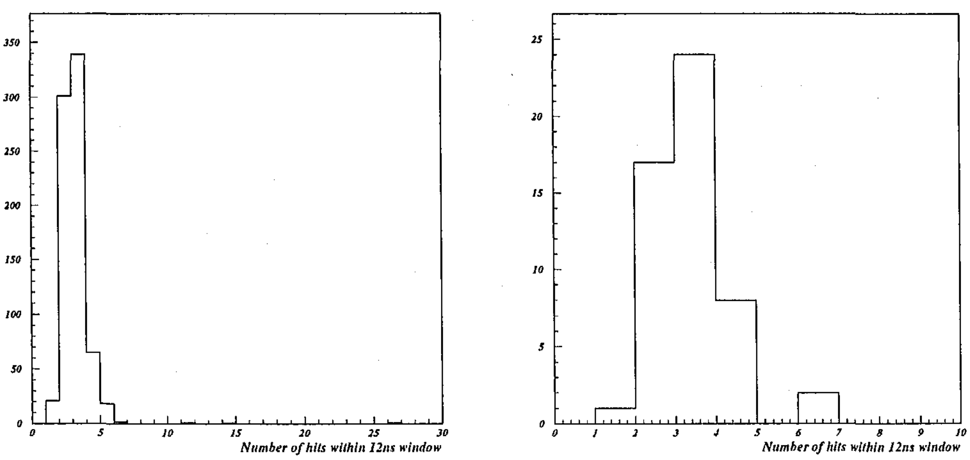

(a) (b)

Figure 9.8: Number of hit PMTs within 12ns window for the prompt peak candidate for (a) 225kt·yr equivalent atmospheric neutrino Monte Carlo events and (b) 25.5kt·yr data of Super-Kamiokande

decay mode of K^+	number of signal (or estimated excess)	number of background	lower limit of partial lifetime
$K^+ \to \mu^+\nu_\mu$	13	55.9 ± 2.5	2.8×10^{32} yr
$K^+ \to \pi^+\pi^0$	4	4.2 ± 0.55	1.3×10^{32} yr
$K^+ \to \mu^+\nu_\mu$ (with prompt γ-ray tag)	0	$(3.7 \pm 1.4) \times 10^{-1}$	1.5×10^{32} yr

Table 9.5: Obtained lower limit of the partial lifetime for $p \to K^+\bar{\nu}$

Chapter 10

Summary and conclusion

10.1 Summary and conclusion

We have studied $p \to \bar{\nu} K^+$ with the Super-Kamiokande detector. This decay mode is the major mode of minimal SUSY-SU(5) GUT prediction. The data were taken from May 1996 to October 1997 and the total detector exposure is 25.5 kt·yr. A total of 3468 fully contained events which consists of 2374 of single ring events and 1094 of multi ring events are observed.

We have analyzed the proton decay mode of $p \to \bar{\nu} K^+$ by using the decay products of K^+. The major decay modes of K^+ are

$$
\begin{aligned}
K^+ &\to \mu^+ \nu_\mu (63.5\%), \\
K^+ &\to \pi^+ \pi^0 (21.2\%),
\end{aligned}
$$

and both modes are analyzed in this thesis.

The momentum distribution of single ring μ-like events is consistent with the atmospheric neutrino background and has no excess around 236MeV/c. Thus, there are no statistically significant evidence for $p \to \bar{\nu} K^+, K^+ \to \nu_\mu \mu^+$ mode. The momentum distribution of π^0 events with one decay electron from μ^+ shows that there are no candidate remaining for $p \to \bar{\nu} K^+, K^+ \to \pi^0 \pi^+$ mode. To reduce the background, we also applied the prompt 6.3MeV γ-ray tagging method for $K^+ \to \mu^+ \nu_\mu$ mode analysis. In the earlier experiments, the detection efficiency of such low energy γ-rays is not sufficient and this is the first time to do the prompt γ-ray tagging analysis. But again, there are no candidate events observed.

As a result, no statistically significant evidence for the nucleon decay has been found and 90% C.L. lower limits of partial lifetime for $p \to \bar{\nu}K^+$ mode have been obtained as:

$$2.8 \times 10^{32} \quad \text{yr for} \quad K^+ \to \nu_\mu \mu^+, \tag{10.1}$$

$$1.3 \times 10^{32} \quad \text{yr for} \quad K^+ \to \pi^0 \pi^+, \tag{10.2}$$

$$1.5 \times 10^{32} \quad \text{yr for} \quad K^+ \to \nu_\mu \mu^+ \text{with prompt } \gamma\text{-ray-tag.} \tag{10.3}$$

The combined 90% C.L. lower limit of partial lifetime for $p \to \bar{\nu}K^+$ is obtained to be

$$\tau/B(p \to \bar{\nu}K^+) \geq 3.3 \times 10^{32}\text{yr (90\% C.L.).} \tag{10.4}$$

The predicted lifetime of $p \to \bar{\nu}K^+$ by the minimal SUSY-SU(5) GUT is 10^{29-33} yr. The obtained lower limit of partial lifetime for $p \to \bar{\nu}K^+$ does not completely rule out but gives a strong constraint to the minimal SUSY-SU(5) GUT in combination with the recent result from LEP.

Comparison with the other experiments

The lower limit of the partial lifetime for this decay mode has been measured by other experiments and those results are summarized in table 10.1.

The limit obtained by Super-Kamiokande is 3 times longer than the previous result from Kamiokande[8], which now appears in the particle data book[67], and much longer than that by the other experiments[13][68]. But the lower limit obtained by IMB3 experiment[5] is 4.6×10^{32}yr, which is longer than the limit obtained in this thesis. This result was obtained through a different method. The detection efficiency for this mode in IMB3 is 41% which is almost the same as in Super-Kamiokande (44%). The exposure is 7.6kt·yr and this is 3.4 times smaller. The observed numbers of events are 15 in IMB and 52 in Super-Kamiokande, respectively. The numbers of events estimated from atmospheric neutrino background are 29 in IMB3 and 55 in Super-Kamiokande, respectively as summarized in table 10.2. Of course, we cannot compare these numbers of events directly but if we compare the normalized event rate of signal and background, normalized event-rate of signal is almost comparable but the background is apparently larger. This is the reason why the limit obtained by IMB3 is higher. If we apply our calculation method to their result through the equation 9.11, the number is 2.5×10^{32}yr for IMB3 and becomes slightly shorter than the result from Super-Kamiokande.

10.2 Future prospect

The Super-Kamiokande is currently running very well. The total exposure of the detector will be up to 100kt·yr within 5 yr and we can search for $p \to \bar{\nu} K^+$ to the lifetime limit of is order of 10^{33} yr. We will also analyze data to search for neutron decays such as $n \to \bar{\nu} K^0$ and $n \to l^{\pm} K^{\mp}$, where $l^{\pm}$ is charged lepton. By combining all these results with the results from LEP, we can give a strong restriction to or rule out the minimal SUSY-SU(5) GUT and other models.

Experiment	exposure (kt·yr)	lower limit of partial lifetime (yr)
Super-Kamiokande	25.5	3.3×10^{32}
Kamiokande	3.76	1.0×10^{32}
IMB (1+2)	3.3	1.5×10^{31}
(3)	7.6	$(4.6 \times 10^{32})^{(*)}$
Soudan 2	0.5	4.5×10^{30}
Frejus	1.3	1.5×10^{31}

Table 10.1: Comparison of the lower limit of partial lifetime for $p \to K^+\bar{\nu}$ mode with the other experiments. $^{(*)}$ See text for a detailed description.

Experiment (decay mode)	exposure (kt· yr)	detection efficiency (%)	number of observed events	number of estimated background	Normalized event-rate of signal (events/kt·yr)	Normalized event-rate of background (events/kt·yr)
Super-Kamiokande ($K^+ \to \mu^+\nu_\mu$)	25.5	44	52	55.9	4.6	5.0
IMB3	7.6	41	15	29	4.8	9.3

Table 10.2: Comparison of results from Super-Kamiokande and IMB3. The Normalized event rates are calculated by dividing the number of events by the exposure and the detection efficiency.

Bibliography

[1] S.Glashow, Nucl. Phys. 22(1961), 59.
S.Weinberg, Phys. Rev. Lett. 19(1967), 1264.
A.Salam, Elementary Particle Physics ed. by N.Svartholm, Stockholm, Almquist and Wiksell(1968).

[2] H.Fritzsch and M.Gell-Mann, XVI Int. Conf. on High Energy Physics, Vol.2(1972), 135.
H.Fritzsch et al., Phys. Lett. 47B(1973).
S.Weinberg, Phys. Rev. Lett. 31(1973), 494.
S.Weinberg, Phys. Rev. D8(1973), 4482.

[3] F.Abe et al., Phys. Rev. Lett. 74(1995), 2676 .
S.Abachi et al., Phys. Rev. Lett. 74(1995), 2632.

[4] H.Geworgi and S.L.Glashow, Phys. Rev. Lett. 32(1974), 438.
For a review, see Phys. Rep. 72(1981), 185.

[5] C.McGrew, Thesis, University of California Irvine (1994).

[6] J.Wess and B.Zumino, Phys. Lett. 49B(1974), 52.
J.Iliopoulos and B.Zumino, Nucl. Phys. B76(1974), 310.
S.Ferrara and O.Piguet, Nucl. Phys. B93(1975), 261.
A.A.Slavnov, Nucl. Phys. B97(1975), 155.

[7] N.Sakai and T.Yanagida, Nucl. Phys. B197(1982), 533.
S.Weinberg, Phys. Rev. D26(1982), 287.

J.Ellis et al., Nucl. Phys. B202(1982), 43.
P.Nath et al., Phys. Rev. D32(1985), 2348.
P.Nath et al., Phys. Rev. D38(1988), 1479.
J.Hisano et al., Nucl. Phys. B402(1993), 46.

[8] K.S.Hirata et al., Phys. Lett. B220 (1989), 308.

[9] P.Langacker et al., Phys. Rev. D44(1991), 817.

[10] Particle Data Group, Phys. Rev. D54(1996), 85.

[11] K.R.Dienes and C.Kolda, Perspectives on Supersymmetry ed. by G.Kane, World Scientific, hep-ph/9712322.

[12] C.Berger et al., Z. Phys. C50(1991), 385.

[13] D.Ayres et al., Proceedings of the 25th International Conference on High Energy Physics, Singapore(1990).

[14] R.Becker-Szendy et al., Nucl. Instrum. Meth. A326(1994), 1.

[15] K.Inoue, Thesis, Univ. of Tokyo, 1993.
K.Kaneyuki, Thesis, Osaka Univ., 1994.

[16] H.Kume et al. Nucl. Instrum. Meth. 205(1983), 443.
A.Suzuki et al., Nucl. Instrum. Meth. A329(1993), 299.

[17] H.Ikeda et al., Nucl. Instrum. Meth. A320(1992), 310.

[18] S.Hiramatsu et al., Proc. Int. Conf. on Nuclear Structure Studies Using Electron Scattering and Photoreaction, Sendai, 1972, p.429.

[19] M.Honda et al., Phys. Rev. D52(1995), 4985.
Private Communication with M.Honda.

[20] V.Agrawal et al., Phys. Rev. D53(1995), 1314.
Private Communication with T.K.Gaisser.

[21] C.H.Llewellyn Smith, Phys. Rep. 3C(1972), 261.

[22] H.J.Grabosch et al., Z. Phys. C41(1989), 527.

[23] S.J.Barish et al. Phys. Rev. D16(1977), 3103.

[24] S.Bonetti et al., Nuovo Cimento A38(1977), 260.

[25] S.V.Belikov et al., Z. Phys. A320(1985), 625.

[26] N.Armenise et al. Nucl. Phys. B152(1979), 365.

[27] K.Abe et al., Phys. Rev. Lett. 56(1986), 1107.
C.H.Albright et al., Phys. Rev. D14(1976), 1780.

[28] D.Rein and L.M.Sehgal, Ann. of Phys. 133(1981), 79.
D.Rein, Z. Phys. C35(1987), 43.

[29] G.M.Radecky et al., Phys. Rev. D25(1982), 1161.

[30] Proc.of the 1979 international symp. on lepton and photon(1979)

[31] T.Kitagaki et al., Phys. Rev. D34(1986), 2554.

[32] E.Oltman et al., Z. Phys. C53(1992), 51.

[33] T.Eichten et. al., Phys. Lett. 64B(1973), 274.

[34] S.Ciampolillo et al., Phys. Let. 84B(1979), 281.

[35] J.G.Morfin et al., Phys. Lett. 104B(1981), 235.

[36] D.S.Baranov et al., Phys. Lett. 81B(1979), 255.

[37] D.C.Colley et al., Z.Phys. C2(1979), 187.

[38] A.S.Vovenko et al., Yad. Fiz. 30(1979), 1014.

[39] S.J.Barish et al., Phys. Rev. D19(1979), 2521.

[40] C.Bltay et al., Phys. Rev. Lett. 44(1980), 916.

[41] N.I.Bker et al., Phys.Rev. D25(1982), 617.

[42] V.N.Anikeev et al., Z. Phys. C70(1996), 39.

[43] O.Erriquez et al., Phys. Lett. 80B(1979), 309.

[44] S.J.Barish et al., Phys. Rev. D17(1978), 1.

[45] H.Sarikko, Neutrino 1979(1979), 507.

[46] S.Barlag et al. Z.Phys. C11(1982), 283.

[47] Paul Musset and Jean-Pierre Vialle, Phys. Rep. C39(1978), 1.

[48] J.E.Kim et al., Rev. Mod. Phys. 53(1981), 211.

[49] D.Rein and L.M.Sehgal, Nucl. Phys. B223(1983), 29.
P.Marage et al., Z. Phys. C31(1986), 191.

[50] L.L.Salcedo et al., Nucl. Phys. A484(1988), 557.
Private communication with H.Toki.

[51] G.Rowe et al., Phys. Rev. C18(1978), 584.

[52] T.Fujii et al., Nucl. Phys. B120(1977), 395.

[53] D.Ashery et al., Phys. Rev. C23(1981), 2173.

[54] C.H.Q.Ingram et al., Phys. Rev. C27(1983), 1578.

[55] K.Baba et al., Nucl. Phys. A306(1978), 292.

[56] R.G.Glasser et al., Phys. Rev. D15(1977), 1200.

[57] T.Kajita et al., J. Phys. Soc. Jpn. 55(1986), 711.
T.Kajita, Thesis Univ. of Tokyo(1985).

[58] T.A.Gabriel et al., SSC Calorimetry Workshop(1989),193-196.
Proceedings of Detector research and development for the Superconducting Super Collider(1990), 608-611.

[59] E.Bracci et al., CERN/HERA 72-1(1972).

[60] A.S.Carrol et al., Phys. Rev. C14(1976), 635.

[61] E.Eichler, JADE-Note 65(1980).

[62] T.Yamsguvhi, Thesis, Osaka Univ..

[63] H.Ejiri, Phys. Rev. C48 (1993), 1442.

[64] Super-Kamiokande collaboration, to be published.

[65] T.Hayakawa, Thesis, Univ. of Tokyo.

[66] W.A.Mann et al., Phys. Rev. D34 (1986), 2545.

[67] Particle Data Group, Phys. Rev. D54 (1996).

[68] Ch.Berger et al., Nucl. Phys. B313 (1989), 509.